UNIVERSITY OF NAPLES “FEDERICO II”

Department of Chemical, Materials and Industrial Process Engineering

Philosophy Doctor in

Industrial Product and Process Engineering

Innovative Processes for Submicron Particle Removal

Tutor

Prof. Amedeo Lancia

Ing. Francesco Di Natale

Coordinatore

Prof. Giuseppe Mensitieri

Candidate

Francesco La Motta

XXIX Cycle-2017

Summary

List of Figures

List of Tables

List of symbols

Latin

ASD	Aerosol size distribution	-
b	FHH isotherm parameter	
BC	Bubble column	-
C_c	Cunningham factor	-
CDF	Cumulative distribution function	-
CMD	Count mean diameter	nm
C_{tot}	Total particle concentration	#/cm^3
C_i	Particle concentration for j_{th} diameter	#/cm^3
C_{BET}	Bet isotherm paramter	
C_e	concentration in the liquid bulk	Mol/m^3
C_s	Concentration in the bulk liquid at the equilibrium with a monolayer	Mol/m^3
d^{5th}	5th percentile diameter	nm
d^{95th}	95th percentile diameter	nm
d_{32}	Sauter diameter	nm
d_D	Droplet diameter	µm
dG_{het}	Variation of Gibbs free energy	J/mol
D_P	Particle diffusion coefficient	m^2/s
d_p	Particle diameter	nm
D_g	Stable liquid embryo diameter	nm
D_w	Water diffusivity in air	m^2/s
E	Collisional efficiency	-
f(m,x)	Correction factor	-
g	Gravity acceleration	m/s^2
GT	Grow tube	-
h	Height of bubble column	cm
I_c	Mass flux	Kg/sm^2
K	Kinetic constant	1/sm^2
k_p	Particle thermal conductivity	W/mK
k_g	Gas thermal conductivity	W/mK

k_n	Knudsen number	-
k_C	Coulomb constant	Nm^2/C
k_B	Boltzmann constant	J/K
J	Nucleation rate	1/s
L	Length of grow tube	cm
M	Molecular weight	g/mol
m	Contact angle	°
N	Total number of particles/droplets	#
N_{B0}	Total number of particles at inlet of bubble column	#
N_B	Total number of particles at outlet of bubble column	#
$n(d_P,0)$	Initial particle concentration	#/cm^3
$n(d_P,t_P)$	Final particle concentration	#/cm^3
n_l	Number of molecule per unit volume in the liquid phase	Molecules/m^3
$P^\circ(T_s)$	Equilibrium vapour pressure	Pa
Pr	Prandtl number	-
Pe	Peclet number	-
P_v	Partial vapor pressure	Pa
P^{eq}	Partial pressure at equilibrium with the adsorbed phase	Pa
PDF	Probability density function	-
$PM_{0.1}$	Particulate Matter with $d_p<0.1$ μm	-
PM_1	Particulate Matter with $d_p<1$ μm	-
$PM_{2.5}$	Particulate Matter with $d_p<2.5$ μm	-
PM_{10}	Particulate Matter with $d_p<10$ μm	-
q_e	Adsorption uptake	Mg/g
q_e	Adsorption uptake for a monolayer	Mg/g
Q_L	Liquid flow rate	mL/min
Q_D	Droplet charge	C
r_B	Bubble radius	mm
r	Radius of growth tube	cm
r_e	Critical embryo radius	nm
R_v	Universal gas constant	J/mol·K
Re	Reynolds number	-
RH	Relative humidity	Pa/Pa
S	Oversaturation	-

S_{lg}	Liquid-vapor Contact surface	m^2
S_{ls}	Liquid-solid Contact surface	m^2
S_{gs}	Solid-vapor Contact surface	m^2
Sc	Schmidt number	-
St	Stokes number	-
St*	Critical Stokes number	-
T	Absolute temperature	K
T_s	Surface temperature	K
T_D	Droplet temperature	K
T_G	Gas temperature	K
T_w	Water film temperature	K
t_P	Particle residence time	s
U_{D-P}	Relative velocity liquid-gas	m/s
V	Charging potential	kV
V_e	Volume of the adsorbed phase	$M^{3/}g$
V_s	Volume of a monolayer adsorbed	$M^{3/}g$
v_B	Bubble rise velocity	m/s
x	Particle radius	nm
WES	Wet electrostatic scrubber	-
Greeks		
α	FHH isotherm parameter	-
α_S	Coefficient of sedimentation	1/m
α_I	Coefficient of inertial deposition	1/m
α_D	Coefficient of diffusive deposition	1/m
δ_x	Error of particle number for size channel	%
ε_0	Vacuum electric permittivity	F/m
ε_P	Particle dielectric permittivity	F/m
ΔG^*	Free energy of formation	J/mol
$\eta(d_P)$	Collection efficiency	-
μ_w	Dynamic water viscosity	Pa·s
μ_g	Dynamic gas viscosity	Pa·s
μ_l	Chemical potential of the liquid phase	J/mol
μ_v	Chemical potential of the vapor phase	J/mol
μ_v^0	Chemical potential at the standard condition	J/mol

λ_a	Air mean free path	m
$\Lambda(d_D)$	Scavenging coefficient	-
ρ_w	Water density	Kg/m^3
ρ_P	Particle density	Kg/m^3
σ	Standard deviation	-
σ_L	Liquid surface tension	N/m
σ_x	Standard deviation of particle size	-
τ	Particle relaxation time	s
$\varphi(d_D)$	Droplets size distribution	-
η^{tot}	Total removal efficiency	-
η^j	Removal efficiency per jth channel	-
η_{GT}^D	Removal efficiency of GT from test D (-)	-
$\eta_{GT\text{-}BC}^E$	Removal efficiency of GT-BC system from test E (-)	-
$\eta_{GT\text{-}BC,W}^F$	Removal efficiency of GT-BC_{empty} from test F (-)	-
η_{BC}^G	Removal efficiency of BC unit from test G (-)	-
$\eta_{BC,W}^H$	Removal efficiency of distributor and wall of BC_{empty} from test H (-)	-
$\eta_{BC,L}^E$	Removal efficiency of liquid of BC from test E (-)	-
η_{BC}^E	Removal efficiency of BC unit from test E (-)	-
$\eta_{BC,L}^G$	Removal efficiency of liquid of BC from test G (-)	-
$\eta_{BC,W}^F$	Removal efficiency of distributor and wall of BC_{empty} from test F (-)	-

Abstract

The removal of fine (FP dp < 2000 nm) and ultrafine particles (UFP dp <100 nm) from anthropogenic flue gases is becoming a priority of environmental chemical engineering because of their toxicity for humans and their contribution in climate change. In fact, once inhaled, particles finer than 300-500 nm penetrate the deepest regions of the lungs and even cross the cellular membranes, reaching the circulatory system and causing a wide range of health problems. In addition, fine and ultrafine particles affect atmosphere and climate characteristics in complex and sometimes still undetermined ways, according to their physical nature. In general, the presence of high particles contamination in the atmosphere is associated to reduction of visibility in cities and scenic areas, cloud formation, secondary reactions of atmospheric pollutants and radiative forcing phenomena.

Fine and ultrafine particles are primarily emitted by combustion processes some of which are located close to high population density area (vehicular traffic, harbours, industrial areas, residential heating) increasing significantly the exposure risk: while the overall particle exposure appears as a limited concern, regional effects are often significant and affect a wide fraction of the world population.

Following the pertinent regulation on air quality and pollution control, the design of conventional fine particle abatement devices was optimised to achieve a very high reduction (even higher than 99.5%) of the emitted particles in mass. Therefore, they are very effective in removing the largest particles (whose weight highly influences the mass removal efficiency) but are far less efficient toward the particles ranging from 100 to 2000 nm, range called Greenfield Gap.

To this end, new technologies able to effectively handle both coarse, fine and ultrafine particles are under development. Among them, it is worth mentioning wet electrostatic precipitators, agglomerates, wet electrostatic scrubbers, pool scrubbing and condensational growth assisted treatment units.

The rationales for using condensational growth as a pre-treatment are that the liquid-solid aerosols can be more easily captured because, their size is larger than the critical regions and the presence of a water shell may favour their sticking with the water-gas interface. Condensational growth can be adopted to increase the removal efficiency of different wet particle removal technologies.

The purpose of this work was to study an innovative system to remove fine and ultrafine particles. The concept design was to couple the gas treatment devices with the condensational growth aimed to enhance the particles collection. Among the removal techniques, the work focused on the bubble columns and the wet electrostatic scrubbers. The concept design consisted to pre-treat particles laden

gas in a growth unit in order to generate a solid-liquid aerosol with larger size that, fed to the removal units, was more easily captured. The growth unit consisted in a growth tube (GT), made up by a glass cylinder high 40 cm and with an internal diameter of 1.5 cm. The concept of the growth unit was to make in contact the aerosol with a warmer liquid film. The supersaturation levels depended on the temperature gradient and the gas velocity. The bubble column (BC) consisted in a glass bottle filled with distilled water (ID= 10 cm, H= 20 cm) having a porous ceramic distributor (D=8 mm) placed 1 cm above the bottom from which the gas enters the bottle and a gas outflow at the bottle cap. The wet electrostatic scrubber (WES) consisted in a cylinder in plexiglass 40 cm high and with an internal diameter of 4.5 cm. It is equipped with an electrospray unit that houses on the top of the chamber. The lateral surface of the reactor presents two 10 mm holes for gas inlet and outlet.

Two different set of experiments were carried out. A first set of experiments was carried out to measure the aerosol growth obtained in the GT and to verify the conditions at which the heterogeneous condensation took place. The second one was meant to measure the particles abatement in the GT, BC, WES and the entire GT-BC and GT-WES systems.

The experiments were performed at a gas flow rate of 48 L/h with the GT operated at liquid temperature between 30 and 70°C. Five different materials were tested: sodium chloride, titanium dioxide, carbon black and calibrated nanoparticles of polystyrene with a mean volume diameter of 100 and 200 nm. The aerosol was generated by an aerosol generator (TOPAS ATM 221) and monitored by two different diagnostic system: the TSI 3340, based on a light scattering measure, and a TSI 3910, based on the electrical mobility measure.

The experimental results on the particle growth showed that at the exit of the GT the initial wide distribution changed towards more narrow shape and moved towards larger particles. This behaviour was observed for all the materials and the mode of their distributions at the highest temperature was roughly 350 nm. Moreover, the supersaturation levels established in the GT for each film temperature were evaluated and it was observed that the particles started to grow at supersaturation level much lower than that one predicted by the classical theory. A deep investigation of the physic of the condensational growth was accomplished in order to explain these experimental evidences.

The experimental results on the particle abatement showed that the GT contributed to the particle removal and had a “cut-off” for particles larger than 500 nm. The tests run with the whole systems showed that indeed the efficiencies of both the BC and the WES improved significantly when the particle growth was observed. The BC had the maximum increment of roughly 100% at 70°C for all the tested aerosols, while the WES had the maximum improvement at 50°C for most of the tested particles, suggesting the presence of an optimum between the particles growth process and its capture mechanisms.

INTRODUCTION

I. Particulate sources and characteristics

There are many kinds of macroscopic and microscopic particles floating in the air: re-suspended soil particles, smoke from power generation, photochemically formed particles, salt particles formed from ocean spray, and atmospheric clouds of water droplets or ice particles. They could affect not only visibility and climate, but also our health and quality of life [1].

All these particles are referred as aerosols (or particulate matter, PM) and due to their wide multi- component chemical composition and large particle size from nanometers to micrometers, they are relatively complex to characterize. [2]

A first convenient and common classification of the aerosols is based on their aerodynamic properties because: (a) they govern the transport and removal of particles from the air; (b) they also govern the deposition within the respiratory system and (c) they are associated with the chemical composition and sources of particles. These properties are conveniently summarized by the aerodynamic diameter that is the size of a unit-density sphere with the same aerodynamic characteristics.

The aerodynamic size based classification of particle consists of three main classes:

- *Ultrafine particles or Nuclei Mode*: 0.005-0.1µm diameter:
  Nuclei mode particles are formed by condensation of vapours during combustion processes and from nucleation of species. They exit the nuclei mode via coagulation with lager particles or each other. This class of particles represents the $PM_{0.1.}$
- *Fine particles or Accumulation Mode*: 0.1-2.5 µm diameter:
  Accumulation mode particles have their sources from coagulation of nuclei mode particles and condensation of vapour on already existing particles. The accumulation mode accounts for the largest mass and number of particles,indeed they are suspended in the atmosphere since does not exist any real efficient removal mechanisms in the atmosphere because of their dimensions. The *fine particulate* is also known as $PM_{2.5}$
- *Coarse Particles*: larger than 2.5 µm diameter:
  The sources of coarse particles are mechanical processes either of natural or anthropogenic origin (windblown desert dust, mechanical industrial processes and combustion processes).
  They experience a rather short lifetime due to their large size. The main removal mechanisms from atmosphere are sedimentation and settling. These particles are also identified with PM_{10}, such as particles with diameter lesser than 10 µm.

For each size category, the particles can be emitted from both natural and anthropogenic sources. Figure I illustrate the main natural sources that affect the concentration of $PM_{2.5}$ (a) and PM_{10} (b) and the anthropogenic ones that affect the concentration of $PM_{0.1}$ (c) and PM_{10} (d) in Europe, where all the shares are reported in mass percentage.

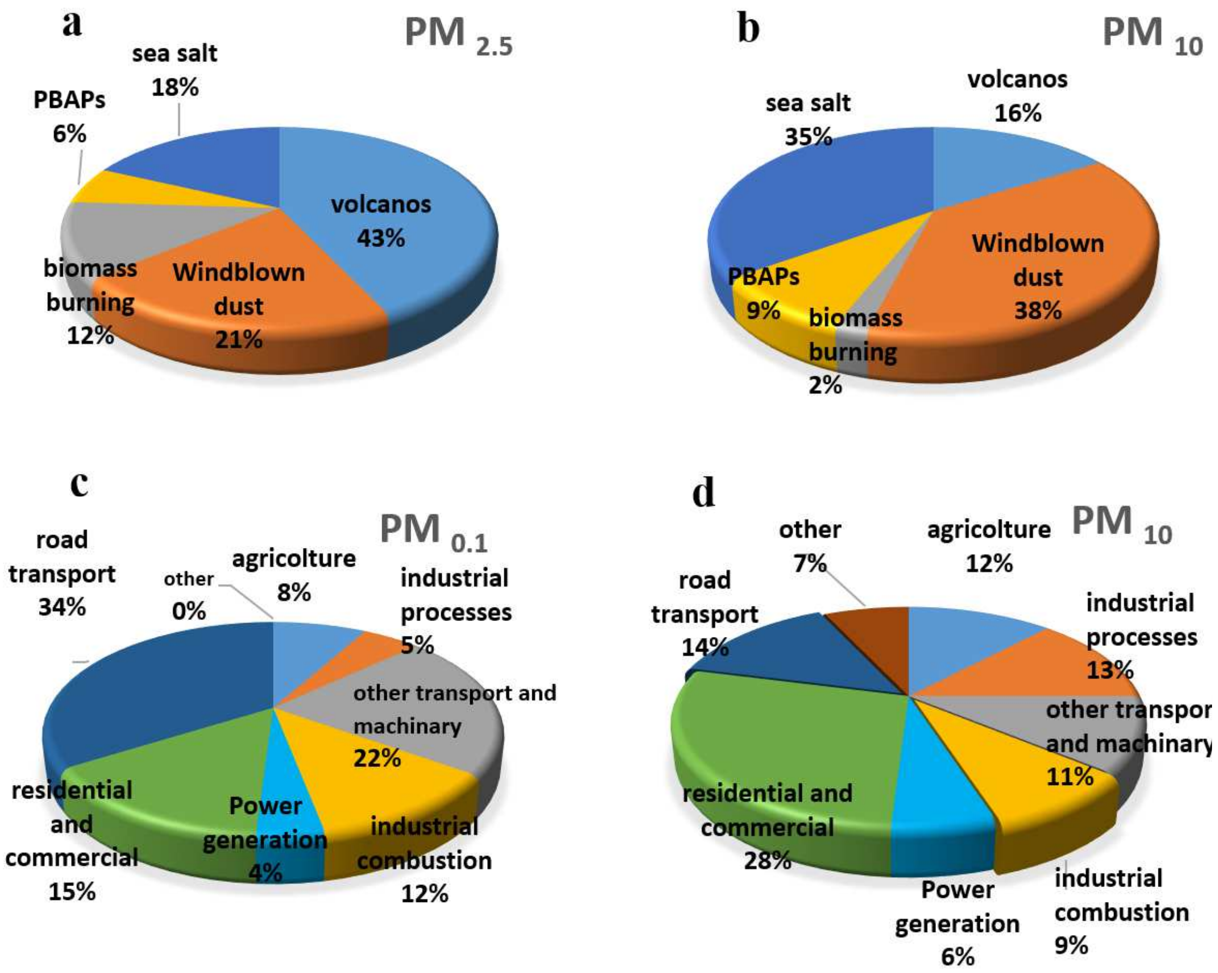

Figure I- Pie chart of anthropogenic and natural emissions. Figures a) and b) show $PM_{2,5}$ and PM_{10} emission from natural sources, while Figures c) and d) show $PM_{0.1}$ and PM_{10} emission from anthropogenic sources [3]**.**

As seen in Figure I, the main natural source of $PM_{2.5}$ and PM_{10} are particles emitted by the volcanos activity, sea salt and windblown dust. The concentration of the primary biological aerosol particles (PBAPs) in $PM_{2.5}$ and PM_{10} is not significant, but these natural particles may play an important role in aerosol– climate interactions, in particular by affecting ice formation in mixed phase clouds. However, the role of PBAPs is poorly understood because the sources and distribution of PBAPs in the atmosphere are not well quantified. [4]

Chemical mixtures represent the majority of atmospheric anthropogenic aerosol particles. A significant fraction of sulphates, nitrates, organics is produced in the atmosphere by combination of several physic-chemical processes, like combustion and manufacturing industry process, and losses of fertilizers from soils [5]. In addition to these processes there are also particles made by domestic activities, like diesel vehicles, fireplaces and meat-cooking operations.

Among all the particles emitted by the anthropogenic source, the 63% of PM_{10} is due to residential and commercial emissions. Despite of the introduction of diesel particles filtration and oxidation catalyst, the great part of the $PM_{0.1}$ percentage is caused by road transport. Therefore, the education of the population about the risks linked to domestic emission is essential

Figure II also reports and summarises the characteristic particle size of the main atmospheric aerosols components.

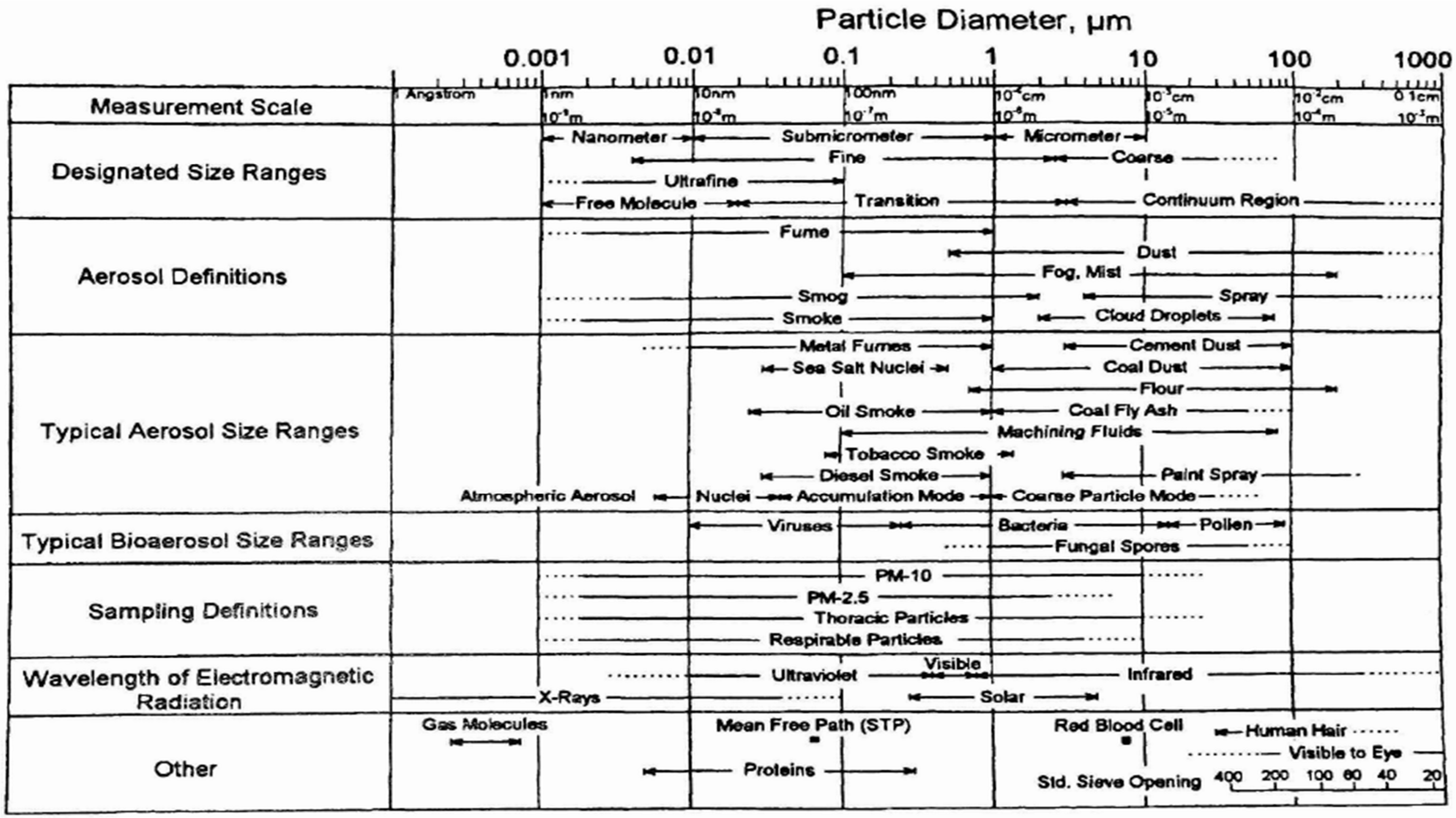

Figure II- Size range of airborne particles showing the ultrafine, fine and coarse fraction together with the characterization of measurement scale adapted from “Aerosol Technologty” [1]

II. Human health effects

Substantial epidemiological evidences suggest that fine and ultrafine particulate matter have adverse human health effects. Although many studies have focused on respiratory health endpoints, there is growing evidence that particulate matter is a risk factor for cardiovascular disease and pulmonary toxicity [6]–[8].

According to the structure of the respiratory system, the particulate could be classified into three categories [9]:

- *Inhalable fraction*: includes all the particles which go into and persist the nostrils and the mouth (PM_{10});
- *Thoracic fraction*: includes the particles which are able to go through the larynx and into the lungs during the inhalation, reaching the tracheobronchial region ($PM_{2.5}$);
- *Respirable fraction*: includes the particles that are small enough to reach and go through the region of the pulmonary alveoli, entering into the blood by overpassing the cellular membranes. ($PM_{0.1}$ and PM_1).

The Figure III shows the ranges of particulate that enter the respiratory system:

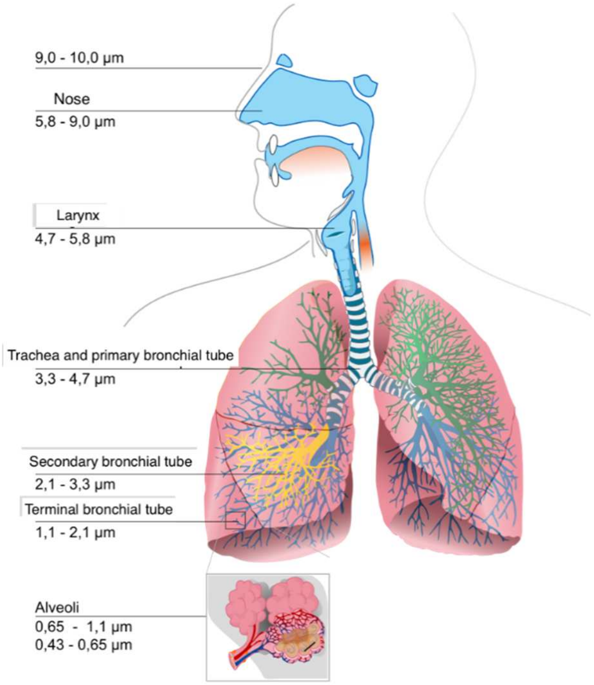

Figure III- The respiratory apparatus and the size ranges of particulate matter which are inhaled

It is important to highlight that particle size plays an important role in defining toxicity as well as their chemical compositions that give rise to high surface reactivity and ability to cross cell membranes, which increase their negative health impact. A correlation between particle size and toxicity relies on the role of particles surface area, a key toxicological parameter determining the amount of available functional groups and of toxic gaseous species that can be adsorbed on particulate matter surface: at the same concentration, the finer the particle, the higher the surface area and the toxicity.

However, as stated from “WHO Air Quality”, at the moment there are no evidences to identify differences in the effects of particles with different chemical composition and sources, with the exception of the black carbon fraction of combustion-related $PM_{2.5.}$ Indeed, the evidences on black carbon toxicity and its contribution on health and climate are more consistent. It was observed that organic compounds as PAHs, metals and inorganic salts adsorbed on Black Carbon and caused cancers and poisoning of human cells. [10]

The effects of PM on health occur at levels of exposure currently being experienced by many people both in urban and rural areas and in developed and developing countries – although exposures in many fast-developing cities today are often far higher than in developed cities of comparable size.

"WHO Air Quality Guidelines (WHO AQG)" estimate that reducing annual average particulate matter (PM_{10}) concentrations from levels of 70 $\mu g/m^3$, common in many developing cities, to the WHO guideline level of 20 $\mu g/m^3$, could reduce air pollution-related deaths by around 15%. However, even in the European Union, where $PM_{2.5\text{-}10}$ concentrations in many cities do comply with Guideline levels, it is estimated that average life expectancy is 8.6 months lower than it would be otherwise due to PM exposures from anthropogenic sources.

III. European legislation

The particulate sources are different and many so it is clear the impossibility to propose a unique regulation on the emission control. Generally, the World Health Organization (WHO) [10] and the European Environment Agency (EEA) drawn the guidelines [11], showed in Table I, for particulate matter.

Table I-- Air quality limit and target values, and other environmental objectives, for PM10 and PM2.5 as given in the EU Ambient Air Quality Directive and WHO AQGs

Size Fraction	Averaging period	EU Air Quality Directive		WHO AQG (µg/m^3)
		Objective and legal nature and concentration	Comments	
PM_{10}	1 day	Limit value: 50 µg/m^3	Not to be exceeded on more than 35 days per year	50
PM_{10}	Calendar Year	Limit value: 40 µg/m3		20
$PM_{2.5}$	1 day			25
PM2.5	Calendar year	Target value: 25 µg/m3		10
$PM_{2.5}$	Calendar year	Limit value: 25 µg/m^3	To be met by 1 January 2015 (until then, margin of tolerance)	
PM2.5		Exposure concentration obligation (b), 20 µg/m3	To be met by 2015	
$PM_{2.5}$		Exposure reduction target (b), 0–20 % reduction in exposure (depending on the average exposure indicator in the reference year) to be met by 2020		

The Ambient Air Quality Directive (EU, 2008) sets limit values for both short-term (24-hour) and long-term (annual) PM_{10} concentrations, whereas values for long-term $PM_{2.5}$ concentrations only have been set (Table I). The short-term limit value for PM_{10} (i.e. not more than 35 days per year with a daily average concentration exceeding 50 µg/m^3) is the limit value that is most often exceeded in Europe. It corresponds to the 90.4 percentile of daily PM_{10} concentrations in one year. The annual PM_{10} limit value is set at 40 µg/m^3. The deadline for Member States to meet the PM_{10} limit values was 1 January 2005. The deadline for meeting the target value for PM2.5 (25 µg/m^3) was 1 January 2010, and the deadline for meeting the limit value (25 µg/m^3) and the exposure concentration obligation for PM2.5 (20 µg/m^3) was 2015.

Beyond these generic guidelines, the European Union proposed specific regulations in the automotive sector. From 1993 to 2014, firstly the European Union emission issued some directives, summarized in the Table II on the particulate emission and other pollutants generated by commercial vehicle.

Table II-Standard emissions for high duty vehicles

Stage	Date	CO	HC	HC+NO_x	NO_x	PM	PM
		g/km					*#/km*
Euro 1	1992.07	2.72 (3.16)	-	0.97 (1.13)	-	0.14 (0.18)	-
Euro 2, IDI	1996.01	1.0	-	0.7	-	0.08	-
Euro 2, DI	1996.01[a]	1.0	-	0.9	-	0.10	-
Euro 3	2000.01	0.64	-	0.56	0.50	0.05	-
Euro 4	2005.01	0.50	-	0.30	0.25	0.025	-
Euro 5a	2009.09[b]	0.50	-	0.23	0.18	0.005[f]	-
Euro 5b	2011.09[c]	0.50	-	0.23	0.18	0.005[f]	6.0×10^{11}
Euro 6	2014.09	0.50	-	0.17	0.08	0.005[f]	6.0×10^{11}

It is possible to note that until 2009 the PM were regulated in terms of mass, i.e. the vehicles had to emit less than 5 mg/km. This regulation is not useful nowadays, since it was understood that the most toxic fraction of particulates is the submicronic one that means in terms of mass the 10%, which corresponds to about 10% of the mass fraction and 90% of its number fraction. Therefore, the Euro 6, dated 2014, regarded the number emission too, in particular the vehicles had to emit less than $6.0\text{x}10^{11}$ particles/km.

Concerning the ship emissions, after recognizing the relevance of shipping on the worldwide and regional atmospheric pollution, specific guidelines were introduced in the Regulations 13 and 14 of the Annex VI of the International Convention for the Prevention of Pollution from Ships (MARPOL) of the International Maritime Organization (IMO) that entered in force on the 19th of May 2005. According to the MARPOL VI Article 14, SO_2 and sulphates particles emissions should be reduced either by using proper scrubbers as after-treatment system or by lowering the sulphur content in the fuels. In specific Environmental Control Areas (ECA), the admitted sulphur weight content in the fuel had to be lower than 1% from the 1st of January 2010 to the 31st of December 2014. Nowadays the maximum admitted sulphur content is 0.1% that will be extended to all ships in the world by 2020. The former limit allowed the use of low sulphur fuels as Marine Diesel (Gas) Oil, known by the acronyms MDO or MGO. Unfortunately, the unit costs of these fuels is far higher than the conventional one and cost benefit analyses are now driving part of the Maritime Sector towards the adoption of after-treatment systems to comply with regulations.[12]

The European Environmental Agency reported that in the 2014 the PM_{10} and $PM_{2.5}$ concentration, measured by specific monitoring stations located in all Europe, were above the EU limit value in most of the European States. In Italy, where the D.lgs. 155/2010 imposes a maximum number of 35 days/year during which it is allowed to have a PM_{10} concentration higher than 50 µg/m^3, “LegaAmbiente” revealed that the most of cities exceeded the WHO limit for more than 50 days in the 2016 and the beginning of 2017 showed a similar trend [13]. These indications push the scientific community and the companies to invest in technological research.

IV. Advanced Removal techniques

Nowadays, the methods for particles analysis show that the particulate matter emitted has a size distribution ranging from few nanometres to microns. For this reason, the regulation has become more restricted and the cut-off particle size has been reduced from 10 µm (PM_{10}) to 2.5 µm ($PM_{2.5}$) and in the future, they will probably tend to 1 µm (PM_1). Many existing devices for particles capture are employed in treatment plants since years, such as cyclones, fabric filters, electrostatic precipitators and wet scrubbers. All these technologies are able to remove the coarsest particulate. Their capture efficiencies reach values almost equal to 100% and the electrostatic precipitator turns out to be better among the others. Yet, the efficiencies become too low for the particles, which mean size is included in the range 0.1-1 µm, denoted as *Greenfield gap* and as showed in the Figure IV. Indeed, these particles are too fine to be subjected to substantial inertial forces, too large to be captured by Brownian forces and prone to be easier re-suspended by the gas. Therefore, they neither benefit from the mechanisms of capture of coarse particles nor from those of nanometric particles, so they are the more difficult particles to be captured.

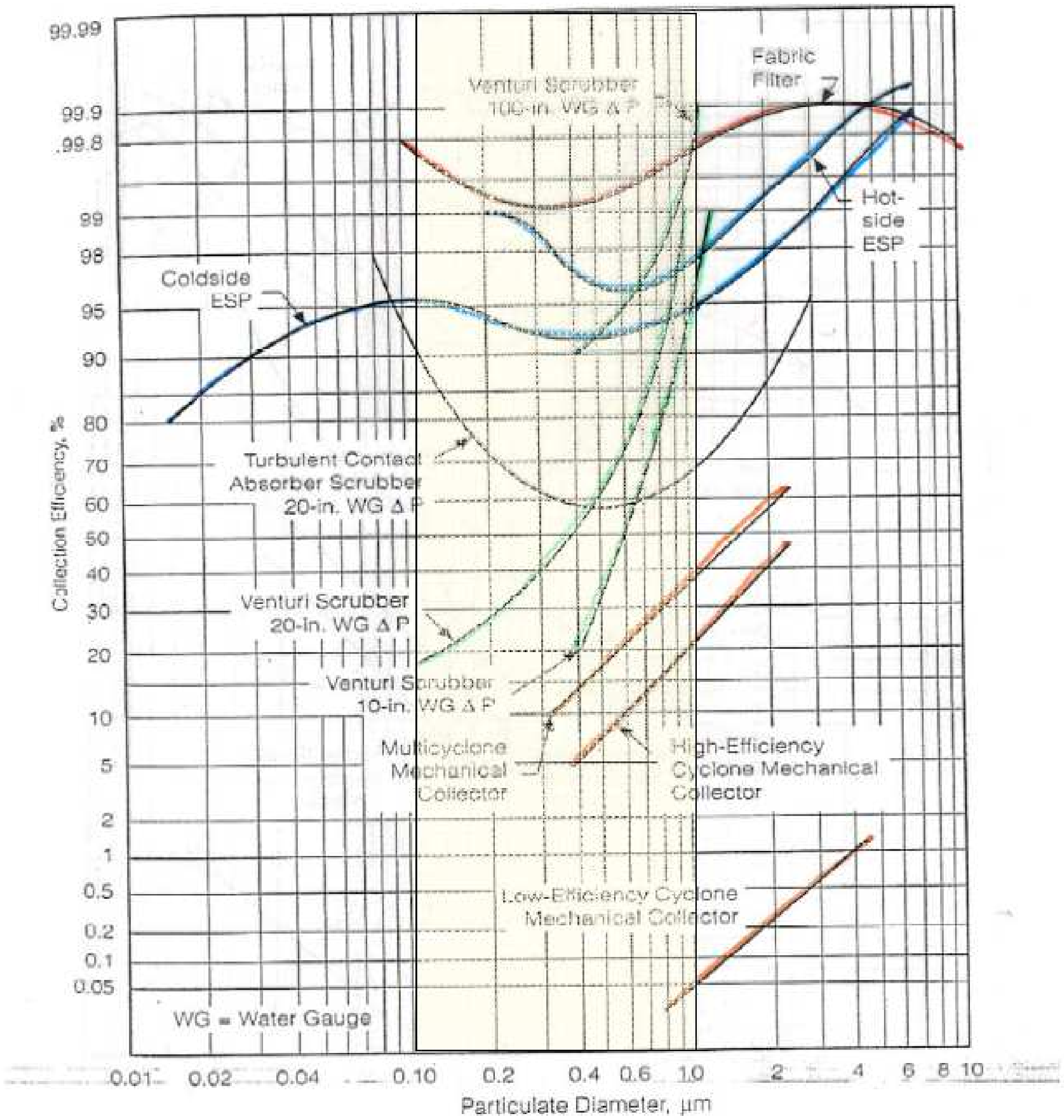

Figure IV- Removal efficiency of conventional particle abatement devices[14]

High removal efficiencies for Greenfield Gap particles are observed only for ESP and FF for industrial application. For small scale, like indoor or cars engines, the effective removal of ultrafine particles can be easily achieved by properly design Ultrafine Particles (ULPA) filters or by Diesel Particulate Filter/Diesel Oxidation catalyst (DPF/DOC). However, these units suffer for severe and rapid clogging when coarse particles or sticky liquid aerosols are present in the treated gas and they can hardly manage inflammable powders, such as flour, carbon etc.[15]–[17]

To this end, for industrial application, new technologies able to effectively handle both coarse, fine and ultrafine particles are under development. Among them, wet electrostatic scrubbers [18], electrostatic precipitators [19], pool scrubbing [20] are under scrutiny as reliable techniques for Greenfield gap particles removal from waste gases. A smart insight would be to apply a preconditioning technique to improve the particles removal efficiency in either conventional or innovative treatment systems. To this end the heterogeneous condensation may play a relevant role. Indeed, this technique consists in the condensation of vapour on the ultrafine particles to create a coarser liquid-solid aerosol whose size is larger than the upper limit of the Greenfield Gap (about 2 µm). Since this phenomenon occurs when the vapour, usually of a low volatile gas, overtakes the supersaturation level, the wet gas treatment devices to couple with are recommended. They consist in liquid-gas systems and can be classified according to nature of feed streams. In Wet Scrubbers and Venturi Scrubber, the gas is the continuum phase and the liquid as droplets represents the discrete one. In bubble column or pool scrubbing, the behaviour of gas and liquid streams is the contrary.

V. Aim of the work

The purpose of this thesis is to provide experimental evidences on the enhancement of the removal efficiency of a bubble column and a WES when the aerosol is previously enlarged. The condensation growth of the particles was achieved in a purpose-made laboratory system. In order to optimize the process of the heterogeneous condensation as preconditioning technique, a deep knowledge on the oversaturation level to trigger the particle growth is required. Therefore, by varying the water film temperature of the growth tube, the ranges of oversaturation levels at which a particle growth was observed, were identified and compared with that one predicted by the classic theory.

The adopted treatment units were a bubble column and a WES because they are emerging in the environmental chemical engineering as promising gas treatment systems due to their main features. Indeed, the first device is characterized by a simple construction, easy temperature control and constant pressure drops with gas flow rate and it is a promising technique for gas cleaning system. The second technology is gaining the attention of the scientific world due to its capability to capture fine and ultrafine particles and simultaneously soluble gases. The purpose of employ two treatments units is to evaluate the performances of a conventional technology, already industrially operating, with a technology that is pending of investigations and suggests the implementation of electrical forces to improve once again the collection efficiency.

At this end, five different materials were tested, whose size ranged between to emulate the ultrafine aerosols in atmosphere. The materials differentiate for their chemical nature and behaviour in presence of a water film. They allowed firstly to better investigate the condensational growth process and identify the operative conditions at which the heterogeneous condensation revealed to be an effective improvement in ultrafine particles capture, and then the performances of bubble column and wet electrostating scrubber in presence of different particle size distributions.

The thesis is structured in four chapters. In the first chapter, the state of the art and the pertinent literature on the removal of sub- micrometric particulate from gas by means of heterogeneous condensation, bubble column and wet electrostatic scrubber applications are reported.

In the second chapter, the experimental rig with a detailed description of the apparatus and the adopted methodologies for both condensational growth and abatement tests are examined in depth.

In the third chapter, the results are expounded with an incisive analysis on the growth mechanism of each materials and on the removal efficiency of the system. In last, the discussion of experimental results is undertaken and the main conclusions are then described.

1 STATE OF ART

1.1 Condensational growth

1.1.1 Theoretical framework

The heterogeneous condensation is a natural phenomenon on which the cloud formation is based. It consists in the creation of a liquid layer surrounding the particles so to transform the solid aerosol in a liquid solid aerosol of larger size. Studies on these topics started at the end of the XIX century and a detailed analysis of the historical background and the State-of-Art on the heterogeneous condensation phenomenon were reported in several papers dating back to the last 10–20 years [21], [22]. Over the years, different theories and models on the mechanisms of the process have been developed and the debate is still open. Indeed, the physics of the process is still unclear and in this work a summary of the main theories is reported. Before entering the details of the models, a brief physically description of the phenomenon is presented.

Heterogeneous condensation on a solid submicron particle is an energetically unfavourable process because the liquid free surface increase causes a free energy rising. In order to overcome the energetic barrier, the vapour must be supersaturated, i.e. the saturation ratio:

$$S = \frac{P_v}{P(T_S)} \tag{1.1}$$

Where S, defined as the ratio between partial vapour pressure P_v and equilibrium vapour pressure, $P°(T_s)$, at the particle surface temperature, T_S, must exceed unity and in a such case we talk about a oversaturation level.

Lord Kelvin [23] firstly indicated that the smaller the particle the higher the required oversaturation to activate condensational growth. In fact, the equilibrium vapour pressure over a droplet is higher than that one over a flat surface due to the droplet surface tension. This effect is described by the Kelvin's relation [23] that estimated the diameter of a stable liquid embryo D_g:

$$D_g = \frac{4\sigma M}{\rho R_v T ln(S)} \tag{1.2}$$

Which associates the vapor saturation S, with the diameter of an existing droplet with diameter D_g composed of condensed vapor, with molecular weight M, density ρ and surface tension σ. In equation (1.2) R_v is the universal gas constant and T is the absolute temperature of the vapour. Therefore, under the effect of a specific oversaturation levels, all the droplets having size larger than D_g are thermodynamically stable.

The classic theory of the heterogeneous condensation as proposed by several authors envisages two consequential stages: nucleation and growth. The nucleation consists in the formation of a liquid embryo on the particle surface; the growth is the condensation of the vapour around the embryo and the consequent enlargement of the particle.

It is worth noticing that, although this equation was developed to describe homogeneous droplets, the same relations hold to describe the liquid embryo formed on a surface, as proven by Fletcher[24] and Smorodin [25]. Each step of the heterogeneous condensation, namely the nucleation and the growth, is characterised by a specific rate. The nucleation rate represents the number of embryo, of a given size d_g, formed per second and per particle and is generally defined as:

$$J = \pi K d_p^2 \exp(-\frac{\Delta G^*}{k_B T}) \tag{1.3}$$

where K is a kinetic constant, k_B the Boltzmann constant, d_p the particle diameter and ΔG^* is the free energy of formation of a liquid embryo (in equilibrium with its vapour phase) on the particle. Several models were presented in the literature to calculate ΔG^* following either the assumptions that a uniform liquid shell immediately surrounds each particle [26] or that initially, the liquid forms one or more embryos on given points of the particle [24], [25], [27], [28]. By substituting the ΔG^* as defined by Fletcher:

$$\Delta G^* = \frac{8\pi M^2 \sigma^3}{3\rho R_v T ln(S\,)} f(m,x) \tag{1.4}$$

Where $f(m,x)$ is a correction factor for the spherical surface that depends on the contact angle $m=cos\theta$ and the particle radius $x=d_p/2$. Commonly, a critical supersaturation S_{cr}^{het} is conventionally defined in the pertinent literature as the level of S required to allow formation of one liquid embryo per second. Application of the Fletcher model for an insoluble and spherical particle for J=1 (1/s) gives:

$$S_{cr}^{het} = \exp\left(\frac{1}{\rho R_v T}\sqrt{\frac{8\pi M^2 \sigma^3}{3 k_B T ln(\pi K {d_p}^2)} f(m,x)}\right) \tag{1.5}$$

S_{cr}^{het} decreases by increasing particle size and gas temperature. Although in line of principle higher values of supersaturation are desired to activate the smaller particles, there is a practical limit for an effective heterogeneous condensation. This is represented by the occurrence of homogeneous nucleation that takes place when nuclei of molecules of condensable components form spontaneously, without the support of any foreign solid surface. This is an undesired phenomenon that causes a depletion of vapour and, thus, an undesired reduction of actual supersaturation level of the gas phase. Homogeneous nucleation rate can be calculated with the Kashchiev [29] model. By analogy with the heterogeneous condensation, a critical value of supersaturation level for homogeneous condensation, S_{cr}^{hom} , can be considered. Typical values of S_{cr}^{hom} are 2–5 [21], [22], [30], [31]. Figure 1.1 reports a comparison of S_{cr}^{hom} and S_{cr}^{het} together with the value of S_{cr}^{K}, that is the supersaturation level required to allow stable formation of a water nucleus of diameter d_k (Eq. (2)) on a particle with diameter d_p (Eq. (7)). Figure 1.1 shows the existence of a region of supersaturation levels where heterogeneous condensation can be achieved without undesired vapour depletions caused by homogeneous condensation.

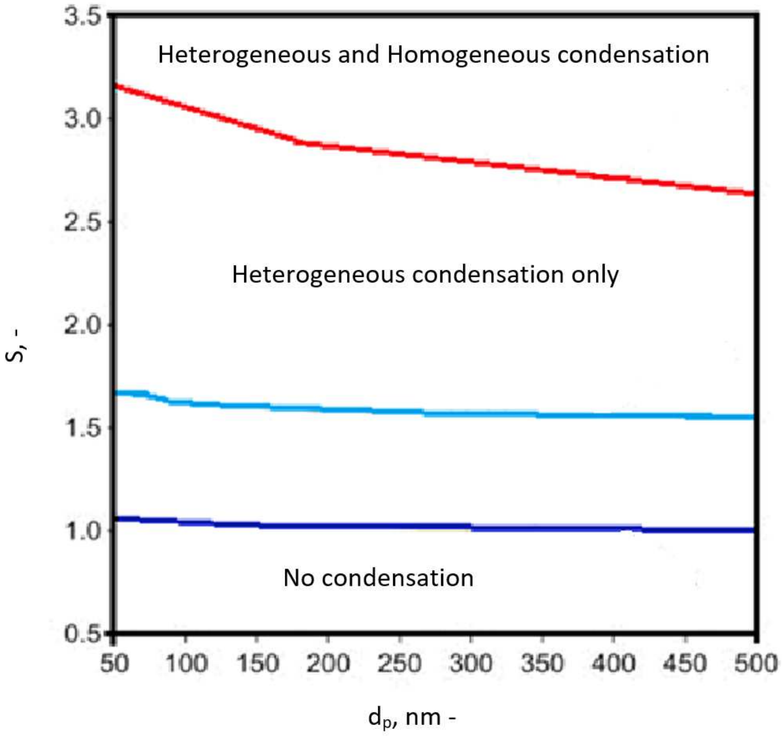

Figure 1-1-Critical saturation levels for homogeneous condensation (red line), heterogeneous condensation (light blue line) and equilibrium condensation given by Kelvin's equation as a function of particle diameter (blue line). P=1 atm, T=300 K; liquid: water;

In the Figure 1.1, it could be observed that the critical saturation levels decrease with particle diameter. The homogeneous condensation occurs at a saturation level above 2.5, while the heterogeneous one between 1.5 and 2.5.

In the years, the condensation of vapour on nuclei has been studying and investigating and the first works are far dated [32]. In fact, this process appears in several macro phenomena, as the cloud formation or the phase transition from gas to liquid. Moreover, several experimental techniques were based on this process as the condensation particles counter (CPC).

1.1.2 Nucleation

The studies in literature deal with the kinetic description of both stages. In general, the goal of a nucleation theory is a quantitative model that links thermodynamic parameters as temperature, vapour pressure, and physical properties, as particle diameter and contact angle, to the production rate of a liquid embryo. The goal of the growth theory is to describe the consequently enlargement rate of the liquid embryos by the agglomeration and the collection of these last.

A briefly resume of the nucleation and growth model present in literature is reported.

The classic nucleation theory refers to the description of the formation of the liquid embryo on a smooth spherical surface. It is possible to differentiate the several nucleation theories based on the particle solubility. In the Figure1.2 the main nucleation theories of soluble (left) and insoluble (right) particles are reported.

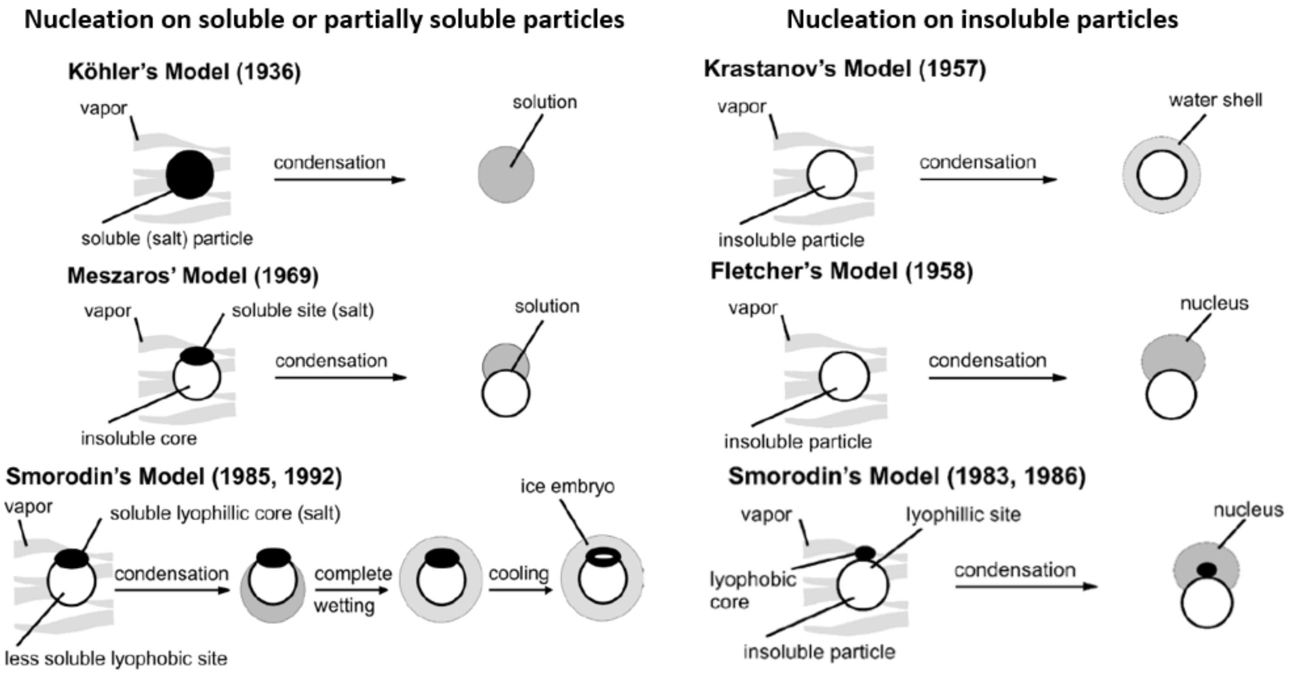

Figure 1-2 Schematic diagram of models for heterogeneous condensation on soluble (left) and insoluble particles (right) [25]

All the theories showed in the Figure 1.2 describe the nucleation step of a vapour condensation on a homogeneous smooth spherical particle. In the 1936, Kohler firstly studied the nucleation of the heterogeneous condensation of vapour on soluble particles[33] . In 1969, Meszaros proposed a nucleation theory of the vapour condensation on an insoluble particle with a soluble site. Smorodin, in 1985, extended this theory identifying further intermediate steps leading to a water surrounding particle. Vapour condensation on insoluble nuclei was analysed by Krastanov [34] and he proposed that the vapour generates a liquid shell, surrounding completely the nuclei. In 1958, starting from the Volmer's theory of the heterogeneous condensation on a flat surface, Fletcher extended it to an insoluble spherical particle starting from the formation of an embryo liquid lens. Moreover, Fletcher investigated heterogeneous nucleation on homophile aerosol particles when the formation of an embryo with size smaller than the particle, forms a finite contact angle ($\theta > 0°$). The contact angle, indicated as θ, is defined as the angle between liquid and solid phase and is described by Young's equation [35]. The Smorodin's model [25] assumes that on the surface of the insoluble particle there are zones, "active sites", with different chemical and physics characteristics, as the coefficient of wetting. The theory suggests that the energy and the rate of heterogeneous condensation on heterophilic particles at a constant supersaturation level depends on the particles size: larger particles enhances the condensation thank to higher concentration of active sites on the surface compared with a smaller particle size.

The major limit of the classic theory is that to apply the macroscopic thermodynamics to the small clusters, neglecting the dependence of the physical properties on the dimension. Several authors [36]–[39] pointed out a discrepancy between the experimental data on the heterogeneous condensation on submicronic particles and the theoretical predictions based on the classical model. Chen et al.[37] studied the heterogenous condensation of water vapor on different materials and they always found significant differences between the theoretical and experimental data in terms of critical supersaturation level. They suggested that a thin liquid layer was generated on the particle surface that reduced the energetic barrier and so promoted the heterogeneous condensation. Koutsky et al. [40] highlighted that the critical degree of the supersaturation was generally smaller than the theoretical one. This discrepancy was ascribable to the energy surface that seemed to be overestimated by the theory. According these experimental findings, it is possible to assume that applying the macroscopic theories on a microscopic level induces to an overestimation of the energetical barrier that depends mainly on the contact angle and the specific surface energy of the liquid droplet.

Therefore, other theories were developed by approaching the process differently.

Ruckenstein and Narsimhan [41] formulated a new theory for the heterogeneous condensation based on the density functional theory. The model is based on the balance between the evaporation and condensation rates of the vapor on the nucleus. Van der Hage [36] recognized firstly a possible role of the adsorption in the heterogeneous condensation phenomenon. He suggested the formation of a thin liquid layer due to the water molecules adsorption on the particles surface and then the growth of this layer could lead to the drop generation. This approach leads to consider the heterogenous condensation process starting from the formation of layer and so the interactions between the liquid and vapor phase is completely different than the vapor-solid one. Consequently, the phase transition needs lower supersaturation levels, confirming the doubts of the classic theory. Furthermore, Laaksonen [42] proposed a new model of vapour adsorption on solid surface based on the formation of molecular clusters, modelled as liquid caps. The fundamentals of this approach are built on the consideration that the classical heterogeneous condensation theories are based on the formation of liquid cluster but it is described with a single parameter, the contact angle, which would be poor to describe such a complex phenomenon. Instead, the adsorption isotherms, based on the formation of cluster on active sites present on the sorbent surface, allow to better describe the process. Laaksonen extended the Frenkel-Halsey-Hill (FHH) adsorption isotherm [43] in order to be applicable both at sub-monolayer surface coverages and at supersaturated conditions. The new model was applied on the experimental results obtained by the condensation of different vapours on different solid surfaces. The work pointed out a good agreement between the experimental data and the new model, laying the groundwork for a new heterogeneous condensation theory.

A different approach was adopted by McCoy [44]. McCoy presented a theory based on the cluster distribution kinetics for single-monomer addition and dissociation as a framework for homogeneous and heterogeneous vapour condensation. The author described the condensation process as the reversible polymerization-depolymerization by monomer addition-dissociation. A population balance and moment equations based on the polymerization theory were applied to describe the experimental data and a good agreement was observed. A similar approach was adopted by Luo et al. [27]. They proposed a kinetic model of condensation vapour on an insoluble spherical particle, considering that the cluster growth is due to the direct addition of water molecules from the vapour and to the surface diffusion of adsorbed water molecules on the particles.

1.1.3 Experimental devices for condensational growth

Once the embryo is formed, it undergoes to an enlargement thanks to the condensation of vapour. Several authors proposed a growth model for the embryo enlargement that strictly depends on the adopted experimental system. In fact, the rate of the embryo growth is ruled by the classical laws of the heat and mass transfer around a single droplet. A supersaturation environment can be achieved in different ways for example by mixing saturated gases of different temperature, by cooling, by chemical reactions and by evaporation a liquid surface. In all these cases, supersaturation is caused either by a reduction of the temperature or by an increase in the vapour pressure in the system. The evaporation of a liquid surface is an economically feasible process to achieve supersaturation economically, also on a technical scale. Many studies on the particle growth deal with the development of the condensation particle counter (CPC). This technique consists in detecting and counting aerosol particles by first enlarging them through heterogeneous condensation. In this way, even the particles with diameter less than 50 nm, that generally are undetectable with conventional optical techniques, are measured.

Concerning the CPCs development, too many literature works deal with this topic and a complete review lies outside from this work. Several CPC were developed from the first one, proposed by Aitken [45] in the 1875, to the more recent tool present in most of the TSI particle detection instruments. A deep study on the CPCs history is presented by McMurry [46]. McMurry classified the CPC in two main categories: expansion chamber or steady flow chambers. The former consists in an adiabatic expansion of a gas stream so to reach a oversaturation level; the latter consists in a tube in which a saturated gas enters and encounters a liquid film with different temperature, generating a oversaturation level. From these two concepts, many authors presented their own systems.

Beyond the development of CPCs, several authors focused on the study of the heterogeneous condensation on particles and the consequent development of experimental set-up to this aim.

A briefly resume of the set up and the growth rate aimed to the heterogeneous condensation study is summarized.

Barret and Fissan [47] proposed a correlation between the rate of growth of the embryo and the supersaturation ratio and they showed as the condensation on small particles needed high supersaturation levels, as suggested by the Fletcher theory.

Li et al [48] proposed a vertical growth tube modifying the original system developed by Nicoloan et al. The tool consists in a vertical glass cylinder with a water distributor on the top that assures the formation of a uniform water film along the internal wall. The gas enters the tube from the bottom and exit from the top. The film water was kept at a desired temperature by means a liquid jacket around the tube. The gradient temperature between the gas and the water film guarantees the oversaturation levels. According to Li et al., the relative humidity, *RH*, depends on the dimensionless parameter ξ:

$$\xi = \mathrm{L/rPe} \tag{1.6}$$

where L and r are the length and the radius of the growth tube, respectively, while Pe is the Peclet number. Their studies indicated that for $Pe>100$, the *RH* level reached 99.5% for $\xi \geq 0.7$.

Chen et al. [37] proposed a new tool to study the heterogeneous condensation on fine particles. The device consisted in a flow cloud chamber (FCC) in which the aerosol growth thanks to the water vapor generated by the gradient of temperature. The authors measured the particle number concentration at the inlet and outlet of the chamber and from these the removal efficiency of the chamber. After solving the mass and heat balance of the chamber and considering the nucleation rate of Fletcher, they compared the experimental efficiency with the theoretical one and estimate the critical supersaturation level at which the process occurred. The results showed a significant disagreement between the experimental and theoretical efficiency and the estimated supersaturation level was 30% less than the theoretical one. According to Chen et al [37], this discrepancy is due to the formation of a thin liquid layer on the particles that promote the heterogeneous condensation decreasing the energy barrier.

Park and Lee [49] derived an analytical solution when the size distribution changes by condensational growth of polydispersed aerosol, using the growing rate derived by Kulmala [50]. The results showed how the size distribution shifted to larger diameter and to a narrower shape.

Fisenko and Brin [51] have presented a new mathematical model of laminar flow diffusion chamber, with a cylindrical geometry, which included mutual influence of homogeneous nucleation and droplets growth on heat and mass transfer processes. In this study, the wall temperature was lower than the gas-vapour mixture, which was introduced in the chamber. The numerical results applied to experimental results, carried out with helium and argon, showed that the model could be applied only for relatively low nucleation rates. The droplet growth, based on this model, was a function of the radial position, and was maximum along the axial position of the chamber.

Fisenko et al. [52] proposed a study about the vapour condensation on nanoparticles in a supersaturated gaseous mixture. The supersaturation was created by mixing two flows with different temperatures in a cylindrical mixer at atmospheric pressure. The conditions for mixing were chosen so that the homogeneous nucleation of vapour did not mask the growth of heterogeneous droplets with nanoparticles inside. A mathematical model of the growth of heterogeneous droplets was developed using a one-dimensional description of the mixer. Five parameters that affect the performance of the particles size magnification were identified: temperature of the saturator and of gas stream, the number density and initial radius of the nanoparticles, and the gas and vapour flow rate ratio. The authors have seen that high number concentration of particles determined low efficiency due to depletion of vapour and that with high supersaturation the final radius of droplet reaches several microns, but led the homogeneous condensation. Besides, the Kelvin effect became important with radii about 10 nm. The results of the simulation were compared with experimental data showing a good agreement.

Brin and Fisenko [52] studied the growth of heterogeneous water droplets containing nanoparticles in two laminar flow diffusion chambers of different designs. The efficiency of heterogeneous condensation was, to a substantial extent, governed by the processes of heat and mass transfer inside a chamber condenser. The integral parameter, C(R), representing the probability that a nanoparticle with radius R was covered with a condensate film in a laminar flow chamber, was calculated. It was established that, in air–water vapour mixtures, the radius of heterogeneous water droplets may amount to several micrometers and efficient condensation began on spherical nanoparticles when their radii exceed 5 nm.

Porstendorfer et al.[39] studied the heterogeneous nucleation of vapor on nanoparticles of NaCl and Ag. They used a process-controlled expansion chamber: the aerosol, opportunely saturated in an humidifier at 28°C, was fed to a cylindrical expansion chamber where a controlled oversaturation level was achieved. The results showed that the critical supersaturaion level to trigger the vapor condensation was lower than the theoretical one evaluated by Kelvin’s equation for the NaCl particles, while was higher for the Ag particles. Moreover, satisfactory agreement with Fletcher's theory for the insoluble particles was observed. For the soluble particles, however, deviations from the corresponding theoretical model were encountered. This can probably be explained by the fact that the above mentioned macroscopic theory of heterogeneous nucleation was applied to particle diameters down to 6 nm.

De Joannon et al. [53] proposed a study on the particulate abatement in a condensational scrubber. Their system consists in a laminar flow chamber where a gas stream was fed and mixed with a vapor stream. They studied the particle removal efficiency of the chamber by varying the vapor concentration and temperatures. The results showed that the dispersed particles were captured in the nucleated water droplets with high efficiency. The highest particle size was reached with the maximum amount of vapor and the lowest temperature. Moreover, they suggested to separate the condensation process in two units, a first aimed to trigger the nucleation that need high supersaturation level and a second aimed to promote the growth.

Xu et al. [54] studied the heterogeneous condensation of water vapor on fine and coarse particles of SiO_2, $CaSO_4$, Fe_2O_3 by means a similar growth tube developed by Tammaro et al.[55] They found that the mean diameter of the aerosols increased with the supersaturation and that the growth ration of the fine particles was higher than that one of the coarse particles. Finally, they showed that the wettability of particle may lead to different processes of heterogenous condensation and it has a strong impact on particle enlargement performance.

1.1.4 Heterogeneous condensation application in gas treatment

The concept of the particle enlargement used in CPC could be also applied identically in gas cleaning technologies: basically, larger particles are more easily captured and the presence of a water shell, and this may simplify their capture in water based technologies (wet scrubber, Venturi scrubber, bubble columns, etc.).

In literature there are many experimental data on aerosol enlargement, the works of Tammaro et al.[55], Xu et al. [54], Fan et al. [27], Chen et al.[37,56] All these works had the goal to provide experimental evidences on vapour condensation under different operative conditions on different kind of particles. Less studies have been accomplished on experimental evidences of a gas treatment system improvement coupled with the heterogeneous condensation.

Lancaster and Strauss [57] were the first to investigate the performance of a scrubber when a vapor injection was implemented. That showed that the observed increment of the particle removal efficiency was due to the occurring of the vapor condensation on the particles, higher vapor led to higher particles capture.

Yoshida et al. [58] proposed a device to improve a supersaturated atmosphere by mixing two kinds of saturated air, one of which was humidified by direct contact with hot water and the other with non-heated water. The degree of supersaturation or the quantity of condensable water vapour was controlled by changing their mixing ratio and the combination of their temperatures. Aerosols were continuously introduced into the supersaturated atmosphere at a constant rate.

The droplet growth can be realized also in trickle bed columns with water as showing investigations of Calvert and Englund [59] and Johannessen et al.[60] that have shown that fine particles can be separated from saturated warm gas streams in packed trickle beds with cold water. The separation of the fine particles was caused by an enlargement of the particles due to heterogeneous condensation.

Yan et al. [61] performed a scrubber with an aerosol growth unit as preconditioning technique and observed an enhancement of the total mass removal particles efficiency from 15% to 85% with particles with d_p 50÷1000 nm. Similarly, Huang et al. [62] coupled a heterogeneous condensation process with a Venturi scrubber increasing the numerical removal efficiency of particles with d_p 50÷500 nm from 35% up to 97%.

Chen et al.[56] equipped an electrostatic precipitator with a fine water mist generator in order to cool down the gas and to improve the particle capture of the system, triggering a heterogeneous condensation process. The removal efficiency increased from 70-90 % to 99% when the water mist was fed for particles ranged from 40 to 10000 nm. Moreover, the authors observed that the capture of particles of 40 nm passed from 62 % to 99%.

Yan et al. [63] studied the particle removal of a system made up by a growth unit, and a wet scrubber, as particle capture unit. The authors studied the efficiency as function of the kind of particles, from oil or coal combustion, and of the steam amount. They observed that the total efficiency increased from 15 % to 95 % when the growth unit was switched on by feeding steam.

In conclusion, the heterogeneous condensation is, indeed, a promising technique which a gas treatment system could be equipped with.

1.2 Bubble column

1.2.1 Principle of functioning

Bubble column reactors belong to the general class of multiphase reactors which consist of three main categories namely, the trickle bed reactor (fixed or packed bed), fluidized bed reactor, and the bubble column reactor. A bubble column reactor is basically a cylindrical vessel with a gas distributor at the bottom. The gas is lead in the form of bubbles into either a liquid phase or a liquid–solid suspension. These reactors are generally mentioned as slurry bubble column reactors when a solid phase exists[64]. Bubble columns offer many advantages such as little maintenance requirement due to simple construction, easy temperature control, limited pressure drops with gas flow rate, significant mass and heat transfer and low initial costs of installation which led to a widely use of this system in the chemical industries[20].

Thanks to their characteristics, bubble columns are suitable to transfer material from one phase to another. For instance, Reay and Ratcliff [65] studied the particle transfer from the liquid phase to the gas phase by means a flotation cell, while other authors studied the bubble column as an alternative gas treatment device where the particles transfer from the gas phase to the liquid.[20], [66], [67]

An industrial application of the bubble column are the pool scrubbers. They are seldom applied in the chemical industry, as gas cleaning system, and most frequently in the nuclear industry, when they act as a security measure: if fission by-product aerosols are accidentally released, they pass through stagnant pools of water, where they are removed before being emitted in the environment [68]-[69].

Advantages of this process are that it operates at high but constant pressure drop and they require low maintenance, which limits the risk of malfunctioning during emergency conditions. There is an extensive literature and a series of textbooks concerning bubble columns hydrodynamic and bubble-liquid interfacial phenomena [70]–[73], but far less studies focused on their application as particle removal process.

A theoretical model on the particles capture mechanisms of the bubble column and a brief literature studies description are reported thereinafter.

1.2.2 Pich's Model

Pich and Schutz [74] described the particle capture in a bubble column as an absorption mechanism and developed a capture model based on three main deposition mechanisms: sedimentation, inertial impact and Brownian diffusion. The model is based on the assumption of spherical bubbles, with an internal circulation represented by a Hill's vortex.

Pich and Schutz starting from the Fuchs model, described the deposition of aerosols in a rising gas bubble by the differential equation:

$$\frac{dN}{dh} = -(\alpha_D + \alpha_I + \alpha_S)N = \alpha \cdot N \tag{1.7}$$

where N accounts for the total number of particle in a bubble, and α_D, α_I, α_S are the coefficient of diffusive deposition, inertial deposition and deposition by sedimentation, respectively.

The solution of the differential equation leads to:

$$\eta_b = \frac{N_{B,0} - N_B}{N_{B,0}} = 1 - e^{-\alpha\, h} \tag{1.8}$$

where N_{B0} and N_B are the total number of particles at inlet and outlet of bubble column, respectively, α (i.e. the sum α_s, α_s and α_s) is called absorption coefficient.

The coefficients are given by equations 1.9-1.11:

$$\alpha_I = \frac{9 v_B \tau}{2 r_B^2} \tag{1.9}$$

$$\alpha_D = 1.8 \sqrt{\frac{D_p}{v_B\, r_B^3}} \tag{1.10}$$

$$\alpha_S = \frac{3 g \tau}{4\, v_B\, r_B} \tag{1.11}$$

where v_B denotes the bubble rise velocity, r_B the bubble radius, τ is the particle relaxation time, D_p the particle diffusion coefficient, g is the acceleration of gravity.

The diffusion coefficient is given by the Stokes-Einstein equation (1.12) and the particle relaxation time by the Eq. (1.13):

$$D_p = \frac{k_B T}{3\pi\eta_g d_p} \tag{1.12}$$

$$\tau = \frac{2\rho_p {d_p}^2}{18\,\eta_g} \tag{1.13}$$

where k_B is the Boltzmann constant, T the absolute temperature, η_g the dynamic gas viscosity, d_p the particle size, ρ_p is the particle density.

Pich and Schuts predicted that the absorption coefficient depends on the particle diameter and presents a minimum for particles with size ranging from 100 to 700 nm, as reported in the Figure 1.2.

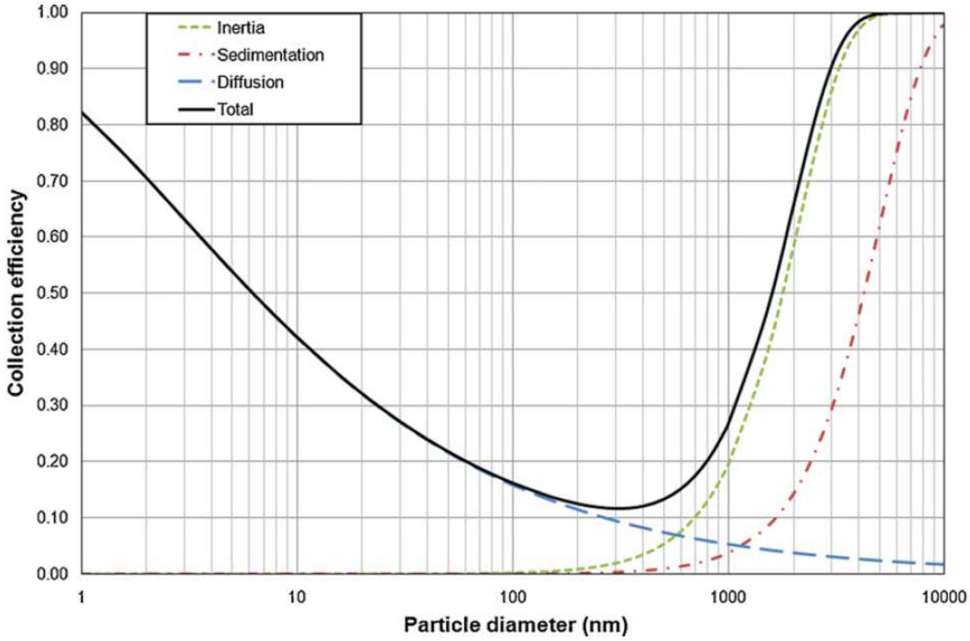

Figure 1-3- Coefficient efficiency calculated with the Pich's model wit h=20cm and d_g=4 mm.

1.2.3 Literature review

Many experimental studies confirm that bubble column scrubbers present high performances for the collection of nanoparticles, as particulate removal device implementing the gas treatment line in the industries [20].

Many different studies were developed in order to characterise the removal efficiency and the influence of diverse parameters on the bubble collection mechanism, such as bubble size and velocity, height of liquid, particles concentration in the gas flow, temperature.

Koch and Weber [66] studied the separation efficiency of bubble columns for gas-borne nanoparticles of sodium chloride and carbon agglomerates using water and water with surfactants as stagnant liquid. They found that the experimentally determined separation efficiency was recovered by employing the Fuchs model. This last introduced a deposition model in order to describe the absorption of aerosol particles during the bubble rise in a liquid, assuming that the internal circulation inside the rising gas bubble represents a Hill's vortex without retardation and neglecting the presents of contaminants on the bubble surface.

Many studies on bubble column efficiency also demonstrated that the removal efficiency increase with the height of the liquid inside the column, such as with the residence time of the particle in the liquid [20], [49], [65].

Meikap and Biswas investigated the fly ash removal efficiency in a multi-stage bubble column scrubber, finding removal efficiency more than 95% [75] for particles with diameter more than 5 µm. They certified that geometrical and flow parameters, together with the physical properties of particles and bubbles could affect the collection efficiency. Their column presented a vertical cylinder fitted with a total of five hollow disks termed as "stages" where the experiments, conducted both with a constant liquid batch and continuous liquid down-flow, showed an increase of the collection efficiency as the liquid flow rate increased.

The results of Charvet et al. [20] highlighted that the bubble size greatly affects the theoretical collection efficiency and they used the Pich's model to compare the experimental results with the theoretical model. Charvet's study affirmed that keeping constant the gas flow rate and column section ratio, if the bubble size decreases, the distance between ultrafine particles and the gas-liquid interface of each bubble decreases and the particle collection consequently increases.

Cadavid-Rodriguez et al.[67] investigated the removal of submicronic particles by a bubble column investigating the effects of the liquid height and a possible solid packing immersed in the liquid. The results pointed out that the minimum of the removal efficiency with the particle diameter was around 100 nm and then for particles from 150 nm to 1000 nm the removal efficiency increased from 20% to 85%, in strongly contrast with the Pich's model prediction. Cadavid-Rodriguez highlighted that the removal efficiency increased with the liquid height and the solid packing improved the bubble column performance.

In the Table 1.1 a summary remarks on several studies reported in the pertinent literature

Table 1-1 Summary remarks of the several authors studies on the bubble column application

Authors (year)	Particles	Gas carrier	Experimental unit	Liquid height	Bubble Diameter	Particles diameter	Gas flow rate	Total Removal Efficiency
Chervet et al. (2011)	Carbon	Air	Bubble column with perforated plate Diameter: 70mm	5 – 30 cm	3.86 - 3.93 mm	5 – 150 nm	1-8 L/min	13 – 98 %
Koch and Weber (2012)	Carbon agglomerates, Sodium Chloride	Nitrogen	Rectangular bidimensional bubble column (62mm x 13mm)	Up to 100 cm	2.07-2.14 mm	10-1000 nm	0.30-034 L/min	13-85%
Meikap and Biswas (2003)	Fly ash	Air	Vertical cylindrical Perspex 0.19 D and 2 m Height	180cm	2-5 mm	2-100 µm	3-6 10^{-3} Nm^3/s	88-98%
Bandyopadhyay and Biswas (2008)	Fly-ash soot	air	Tapered Column: D_1 =0.19 m	2.7-5.9 10^{-3} m^3	N/A	9.82 - 1.43 µm	3.75-6.2 10^{-3} m^3/s	77-99%

			D_2=0.1 m H=0.87 m					
Yuu et al. (1976)	Fly-ash Stearic acid	Air	Bubble Column	1.7-22 cm	0.17-0.44 cm	1.5-3.2 µm	0.5-2.0 L/min	15-92%
CAdavid-Rodrigues et al. (2014)	PVA particles	Air	Bubble column	5-10-20-30 cm	4-8 mm	10-1000 nm	4-12 l/min	20-90%

1.3 Wet Electrostatic Scrubbing

1.3.1 Principle of functioning

The wet electrostatic scrubber (WES) reactor is an upgrade of the traditional wet scrubber and it inherits all its advantages as the low-pressure drops, the reduced process costs and the simultaneous ability to capture soluble gaseous pollutants (SO_x, NO_x, HCl, soluble VOCs). It is a spray tower equipped with an electrified spray unit for electrically charged water droplets generation and, optionally, a particle pre-charging unit [12].

The idea of employing the electric field in capture devices was born from the observing of electrostatic phenomena at the basis of particle scavenging during thunderstorms, when the highest removal of atmospheric aerosol is achieved. In 1944 Penney [76] was the first to suggested the electrostatic scrubbing by two simple observations:

i. the particles emitted by industrial processes and diesel engines are generally bipolarly charged;

ii. water droplets can be easily charged and sprayed in a polluted gas to attract the particles charged with opposite sign.

Considering that the main particle scavenging mechanisms in a typical (non-electrified) wet scrubber are related to particle/drop collisions driven by hydrodynamic forces –mainly due to the Brownian diffusion for ultrafine particles and to the inertial impactions and hydrodynamic interceptions for micrometric ones- the collection efficiencies of industrial WS are higher than 90% for particle diameters coarser than 1µm and finer than 0.1µm, similarly to the typical values obtained with ESP and FF. On the contrary, the WS efficiency falls below 60% in the Greenfield gap, resulting less effective than ESP and FF. In this framework, the electrified wet scrubber takes advantages from Coulomb forces $\boldsymbol{F_E}$ between particles and water drops or from image forces $\boldsymbol{F_{IM}}$ between charged droplets and uncharged particles or uncharged droplets and charged particles.

For submicron particles, the attention is focused on, the inertial effects are negligible, and only the effects of electrostatic forces should be regarded. In this way, the collection efficiency depends mainly on the charging mechanism or the charge level.

The spray electrification improves the wet scrubber efficiency towards submicronic particles because spray unit for electrically-charged water droplets generation and, optionally, a particle pre-charging unit. The sprayed droplets act as a “diffused” collecting surface, replacing the plates of a conventional electrostatic precipitator. It is assumed that the particles are permanently captured by the drops as soon as they encountered their surface. [77], [78]. This last assumption regards the droplet-particles interactions that are still unclear and only this strong hypothesis is envisaged.

The functioning of WES unit depends on the characteristics of particles and droplets as well as on the dynamics of their interaction It has a high numbers of process variables, which are not defined definitively, because of a wide range of configurations from the spraying mode to reactor geometry but the design of this kind of reactor is far from being optimized [18] It is due to the lack of specific regulations on particle abatement in large-scale application and technological experiences with it [12]. From the mixture of the types of scrubbers, there are four main electrostatics scrubbers that we briefly describe in the following:

i. CO-flow Vertical Electrostatic scrubber (COVE): the gas flows downwards and the charged droplets are sprayed at the upper part of the chamber;

ii. CoUnter-flow Vertical Electrostatic scrubber (CUVE): the gas flows upwards and the charged droplets are sprayed at the upper part of the chamber;

iii. CRoss-flow Horizontal Electrostatic scrubber (CRHE): the gas flows horizontally and the charged spray generated at the upper wall of the chamber;

iv. Venturi-Nozzle Electrostatic scrubber (VNE): the charged spray is injected into the throat of the Venturi nozzle, which can be positioned at any angle (from vertical to horizontal).

According to Jaworek et al [79] reviews, five types of wet electrostatic scrubbers, based on different approaches on charging particles and droplets, were proposed:

i. Opposite-Polarity Electrostatic Scrubber (OPES): liquid droplets were charged to polarity opposite to that of dust particles, and the particles were deposited onto the droplets due to Coulomb attraction forces.

ii. Same-Polarity Electrostatic Scrubber (SPES): the droplets and dust particles were charged to the same polarity, and the repulsive force led the particles towards the chamber walls.

iii. Double-Polarity Electrostatic Scrubber (DPES): two sprays of droplets were charged to opposite polarities and mixed with the particles, which were captured by droplets.

iv. Charged-Droplets Electrostatic Scrubber (CDES): only droplets were electrically charged, while the particles remained un-charged; the droplets induced an image charge on particles that were collected.

v. Charged-Particles Electrostatic Scrubber (CPES): only particles were charged, while the droplets were un-charged; the capture mechanism was the same of CDES configuration.

vi. Charge-Transfer Electrostatic Scrubber (CTES): the particles were uncharged and the droplets were charged to either polarity; the evaporating droplets produce free ions or charged water clusters, which condense onto the particles, which became charged by this way, and next deposited onto the chamber walls due to the space charge force.

1.3.2 Particles and droplets charging mechanisms

Regarding the charging of dust particles, the following processes have been tested in the literature for general purposes: charging by ionic current [80], charging by ion beam [81], [82], contact charging via charge transfer from electrically charged electrode [83], triboelectrification during contact of particle with a material of different work function [84], photo-charging via particle bombardment with photons of sufficiently high energy [85], radioactive charging [86], thermos-emission charging at a high temperature [87], plasma charging in an ionized gas [88], and electron-beam charging [89]. However, for practical reasons, only the charging by ionic current generated by corona discharge appeared to be the most effective and suitable for the WES application [90]. To this goal, various types of DC corona, co-flow or cross-flow chargers, and cross-flow AC chargers have been developed [90]. Although experimental results and theoretical considerations have shown that AC chargers provide higher level of charge on the particles and the particle loss is lower than in DC chargers [80], the complex construction and supply system of AC chargers prevents them from wide-scale industrial applications, and co-flow corona chargers can be recommended for electrostatic scrubbers.

On the other hand, the charged spray can be generated by one of the following methods [90]:

i. Corona charging: the droplets flow through an ionic glow generated by a corona discharge generated on a needle tip set at high voltage,

ii. Induction charging: the electric charge is induced on the surface of liquid jet ejected from a mechanically-forced atomizer by an external electric field generated by HV induction electrode, while the nozzle is kept at ground potential

iii. Electro-spraying (electrohydrodynamic atomization-EHD): a needle is held at high potential and the liquid is atomized by purely electrodynamic interaction between the electric field and the liquid surface

The electric charge acquired by liquid droplets is spread on external surface, and the inner charge is zero. The charging quality depends on spraying feature as droplets size and flow rate. When a liquid droplet is surrounded in an electric field and charged, it exerts an electric force, which is opposite to the surface tension force. If the electric force overcomes the surface force, the droplet goes off. The point of equilibrium is a limit charge level called Rayleigh limit that for a droplet of a diameter d_D, it is expressed as:

$$Q_R = 8\sqrt{\pi\sigma_L\varepsilon_0 d_D^2} \tag{1.14}$$

where σ_L ε_0 d_D^2 are respectively the liquid surface tension, the vacuum electric permittivity and the droplet diameter.

In the corona charging mechanism, the sprayed droplets are charged at the same polarity of the voltage applied to the needle with a fraction of Rayleigh limit about 5% and it is the less used mechanism to charge liquid jets because of low charging levels. In the induction charging, the liquid spray goes through the electrode without touching it and the formed droplets acquire a charge with polarity opposite to the potential applied to the electrode and have a charging level of 10% of Q_R in the best conditions. Concerning the electrospray, it is a process of simultaneous droplet generation and charging by means of electric field [91]. In Figure 1.3, the mechanism is illustrated.

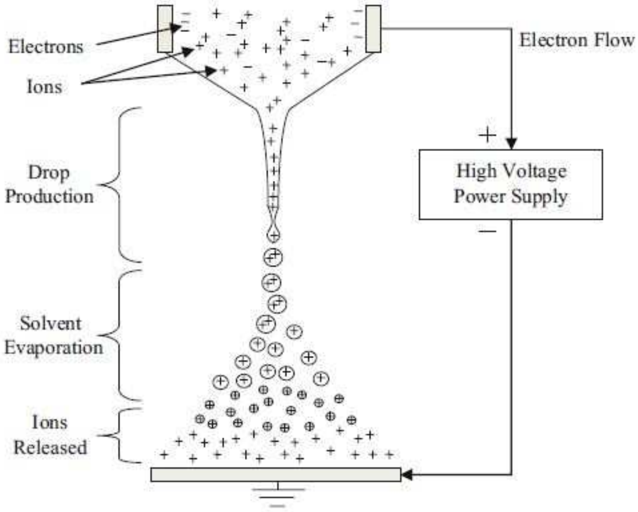

Figure 1-4 Droplets formation and charging through electrospray [92]

The electric field is applied directly on liquid flowing out from a capillary nozzle held at high potentials. The electrostatic force opposes the surface tension force on the interface: the liquid surface is deformed and the formed meniscus is called Taylor's cone [92] The cone breaks into droplets when the electric field strength is high enough to overcome the surface tension force. The advantages of this mechanism are related to droplets size. Indeed, they are very fine and, if charged positively, their mean size can be lower than micrometre. The droplets size distributions are very narrow and in specific conditions the droplets can be of equal size. The charge on droplets is the same polarity of voltage applied and the charge magnitude is close to one-half of Rayleigh limit. For a liquid of given physical properties, the spraying modes changes from one to another with the variation of potential and liquid flow rate. In Table 1.2, the meniscus and jet form, the geometry of liquid emitted and the sprayed aerosol characteristics obtained by atomizing distilled water are listed as described by Jaworek et al. [93].

Table 1-2- Spraying modes regimes in electro-spraying of distilled water [93]

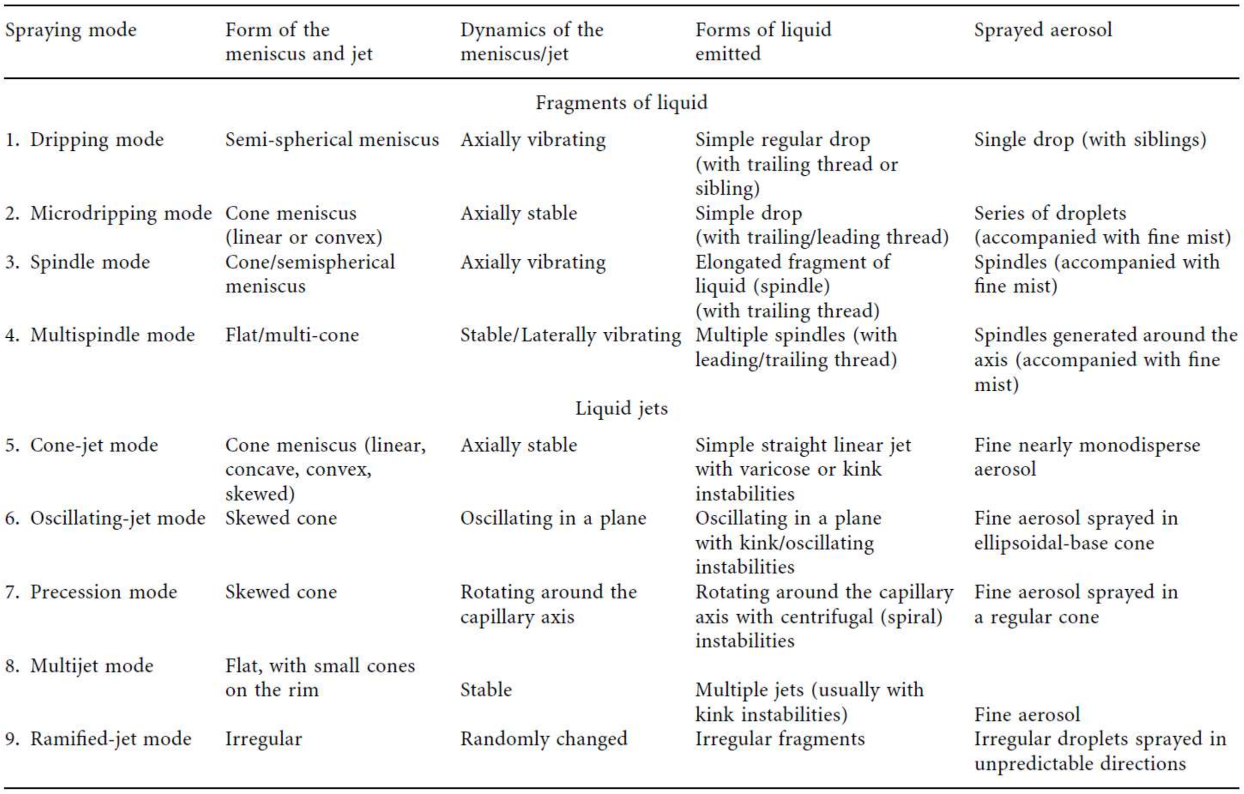

Spraying mode	Form of the meniscus and jet	Dynamics of the meniscus/jet	Forms of liquid emitted	Sprayed aerosol
		Fragments of liquid		
1. Dripping mode	Semi-spherical meniscus	Axially vibrating	Simple regular drop (with trailing thread or sibling)	Single drop (with siblings)
2. Microdripping mode	Cone meniscus (linear or convex)	Axially stable	Simple drop (with trailing/leading thread)	Series of droplets (accompanied with fine mist)
3. Spindle mode	Cone/semispherical meniscus	Axially vibrating	Elongated fragment of liquid (spindle) (with trailing thread)	Spindles (accompanied with fine mist)
4. Multispindle mode	Flat/multi-cone	Stable/Laterally vibrating	Multiple spindles (with leading/trailing thread)	Spindles generated around the axis (accompanied with fine mist)
		Liquid jets		
5. Cone-jet mode	Cone meniscus (linear, concave, convex, skewed)	Axially stable	Simple straight linear jet with varicose or kink instabilities	Fine nearly monodisperse aerosol
6. Oscillating-jet mode	Skewed cone	Oscillating in a plane	Oscillating in a plane with kink/oscillating instabilities	Fine aerosol sprayed in ellipsoidal-base cone
7. Precession mode	Skewed cone	Rotating around the capillary axis	Rotating around the capillary axis with centrifugal (spiral) instabilities	Fine aerosol sprayed in a regular cone
8. Multijet mode	Flat, with small cones on the rim	Stable	Multiple jets (usually with kink instabilities)	Fine aerosol
9. Ramified-jet mode	Irregular	Randomly changed	Irregular fragments	Irregular droplets sprayed in unpredictable directions

The classification made by Jaworek [91] described electro-spraying regimes observed at maximum liquid flow rates of about 3 mL/min. For distilled water, at larger flow rate, the main spraying regimes that we observed in our experiments were *dripping mode*, *short jet whipping mode* and *jet mode*, and they were in accord to Agostinho et al results [94]. In *dripping mode*, the droplets geometry changes from a regular sphere at low voltages to an ellipse when the potential increases and have diameter of about 300 µm. When the charge acquire is half of Rayleigh limit, sibling droplets start to form perpendicularly to capillary axis. In spindle mode, fragments of liquid elongate from the tip of the capillary. After the detachment of spindle-like jet, several dispersed droplets are formed with diameters ranging from 300 to 500 µm and the meniscus contract to a hemi-sphere and a new spindle forms [91], [93].

As the liquid flow rate and the charging potential increased so that the *dripping mode* was not observed anymore, a transition regime from *dripping* and *jetting* was found. The *transition regime* is indicated in the pertinent literature as *dripping faucet* (DF) [95]. In this regime, a small jet was formed and the droplets detached from it with size and frequency depending on operating conditions.

The *simple jet mode* was described by Agostinho et al. [94]. The authors used distilled water at flow rate ranging between 0 and 8 mL/min and charging potential from 0 to 11 κV in a needle of 250 µm ID and 500 µm OD. They defined the *simple-jet mode* as the regime at which the droplets formation occurred from a stable liquid jet exiting directly from the nozzle tip. However, the liquid jet was rather small compared with the jet formed in *jetting regime* [96]. At fixed liquid flow rate, by increasing the charging potential, Agostinho et al [94] observed a shift from the dripping to simple jet mode caused by the elongation of liquid from the nozzle tip due to the axial component of electric field. It accelerated the liquid generating smaller droplets (*short jet whipping regime*).

The analysis of charging mechanisms leads to the conclusion that the induction charging one could be the most suitable for large scale WES application. Indeed, the droplets charged in corona discharge acquire a charge much lower than those charged by induction or those generated by electro-spraying. Another disadvantage of using corona charging method is that the droplets are precipitated on the electrodes and isolators leading to increased leakage current or electric breakdown. Regarding the electro-spraying, the droplets reach the highest charge level but the employed flow rates, maximum mL/h, are too low for gas cleaning purpose at pilot scale. Therefore, the induction charging for liquid droplets, with its flow rate about L/min and charge level of 10% of Rayleigh limit, seems to be accepted as the more suitable mechanism, and the particles charging with a DC co-flow corona charger with polarity opposite to liquid is regarded as necessary condition to reach remarkable collection efficiencies. In case of low liquid flow rates, the electro-spraying is the most suitable configuration to produce small droplets and highly charged.

1.3.3 Scavenging Model

Di Natale et al. [18] [97], [98] developed a benchmark equation to evaluate the removal efficiency of submicron particles through a wet electrostatic scrubber based on the model of Seinfeld and Pandis in atmospheric research. The developed model that will be briefly described in the following is a stochastic modelling of wet electrostatic scrubbers due to:

i. Statistical size distribution of scavenging droplets,

ii. Statistical size distribution of dust particles,

iii. Turbulent flow of scavenging droplets,

iv. Turbulent flow of exhaust gas (Re>2×10^3)

v. Statistical charge distribution of submicron particles,

vi. Brownian motion of the particles.

The collection efficiency of particles with diameter d_p and residence time in the scrubber t_P, is defined as ratio of captured particles concentration and their initial concentration as:

$$\eta(d_p) = \frac{n(d_p,0)-n(d_p,t_P)}{n(d_p,0)} = 1 - e^{-\Lambda(d_p)t_P} \tag{1.15}$$

where $\Lambda(d_p)$ is the scavenging factor, expressed as in Eq. 1.16:

$$\Lambda(d_D) = \int_0^\infty \frac{\pi(d_D+d_p)^2 U_{D-P}}{4} EN\psi(d_D)d(d_D) \tag{1.16}$$

where d_D is the droplet diameter, N is the number of liquid droplets for meter cubic, $\psi(d_D)$ is the droplets diameter distribution and E is the collisional efficiency.

The collisional efficiency estimates the fraction of particles in the contact chamber that collide with the liquid droplets. If the collision efficiency has a unitary value, all the particles in the WE unit are collected by droplets; if it exceeds unity, then particles outside the volume swept by liquid droplets are collected too. The collisional efficiency depends on particle-droplet interaction and it is evaluated by adding the contributes of every mechanism [99] that will be considered in turn in the following.

The first mechanism is the *inertial impaction*. It is the most relevant capture mechanism for particles with d_p >1µm which *impact* against the droplets and depart from the gas stream. Fine particles with too inertia keep on following the gas streamline. For relatively large particles compared to collector size (i.e. the liquid droplet), the capture occurs by *directional interception*: the gaseous streamline flows close to liquid droplets and the particles that touch the collector are captured. If the particle inertia is high, the particles, which pass within a distance $d_p/2$, are collected, otherwise they are collected if their centre approaches closer than $d_p/2$ from the droplets. Both the *inertial impaction* and *directional interception* are mechanisms based on aerodynamic interaction of the two phases and depend on particles mass and size.

The *Brownian diffusion, Thermophoresis and Diffusionphoresis* are mechanisms based on aerodynamic capture by flux forces. Indeed, these occur when an external force acts on particles and lead them to be collected and are efficient for particles with negligible inertia*:* d_p < 1µm. The *Brownian diffusion* is the random motion of very small particles that may collide with liquid droplets. The collection efficiency depends on Prandtl (Pe) and Reynolds (Re) numbers. It is very small if the Prandtl number is less than 10 while it is satisfactory for high Reynolds numbers. *Thermophoresis* occurs when a gradient of temperature between gas and liquid takes place. If the gas stream is made by colder and hotter zones, the particles move towards the colder ones due to thermal force. Regarding that the liquid phase is colder than gaseous one, the *thermophoretical* motion promotes the collection mechanism because the probability that the particles may collide on liquid surfaces rises. This mechanism is independent on droplet density. *Diffusionphoresis* aids the capture efficiency when a gaseous concentration gradient exists or when Stephan flow takes place. The Stephan flow contribute is a consequence of condensation or evaporation in the liquid phase that causes the flow of gaseous compounds towards or away from the surface of a volatile liquid, respectively. This suggests that positive *diffusiophoresis* exists when particles to be. collected in the presence of liquid droplets exist in a saturated and cooled gaseous medium. Hot dry gases develop a negative phoretic force; the water evaporation pushes particles away from the collector.

The last mechanism is *electrostatic interaction*. Electrostatic attractions occur because the particle, the droplet, or both possess sufficient electrical charge to overcome the inertial forces; then the particle can be attracted by the droplet and collected. If only droplets or particles are charge, the electrostatic forces are also present due to image forces.

In WES, *the electrical interaction* mechanism contribute is added to *inertial impact* and *diffusion* ones, because these are dominant for particles ranging from 0.1-1 μm, which the investigation is interested to [100].

The collisional efficiencies for each mechanism could be estimated by relations present in the pertinent literature and listed in Table 1.3.

Table 1-3- Collisional efficiency for capture mechanisms

INERTIAL IMPACTION, E_{In}		
$E_{In} = \left[\frac{St - St^{*}}{St - St^{*} + 2/3}\right]^{3/2} \left(\frac{\rho_p}{\rho_w}\right)^{1/2}$	**(1.17)**	Slinn 1983[101]
$St = \frac{C_c \rho_p d_p^2 U}{18 \mu D}$	**(1.18)**	
$St^{*} = \frac{1/2 + 1/2 \ln[1+Re]}{1+\ln[1+Re]})$	**(1.19)**	
$E_{In} = \left[\frac{St}{St + 0.35}\right]^2$	**(1.20)**	Licht et al. 1988 [99]

$E_{In} = 3.4\, St^{9/5} \quad at\ St \leq 0.5)$	**(1.21)**	Kim et al. [102]
$E_{In} = 1 \quad at\ St > 0.5$	**(1.22)**	
DIRECTIONAL INTERCEPTION, E_{DI}		
$E_{DI} = 4H\left[\omega^{-1} + \left(1 - 2Re^{1/2}\right)H\right]$	**(1.23)**	Slinn [101]
$\omega = \frac{\mu_w}{\mu}$	**(1.24)**	
$H = \frac{d_p}{D}$	**(1.25)**	
$E_{DI} = \frac{(1-\alpha)}{(J' + \omega K)}\left[\left(\frac{H}{1+H}\right) + \frac{1}{2}\left(\frac{H'}{1+H'}\right)^2 (3\omega + 4)\right]$	**(1.26)**	Jung and Lee[103]
$J' = 1 - \frac{6}{5}\alpha^{\frac{1}{3}} + \frac{1}{5}\alpha^2$	**(1.27)**	
$\omega = \frac{\mu_w}{\mu}$	**(1.28)**	
$K = 1 - \frac{9}{5}\alpha^{\frac{1}{3}} + \alpha + \frac{1}{5}\alpha^2$	**(1.29)**	
$H' = \frac{d_p}{D}$	**(1.30)**	
BROWNIAN DIFFUSION, E_{BD}		
$E_{BD} = \frac{4}{Re\ Sc}\left[1 + 0.4\ Re^{\frac{1}{2}}\ Sc^{\frac{1}{3}} + 0.16\ Re^{\frac{1}{2}}\ Sc^{\frac{1}{2}}\right]$	**(1.31)**	Slinn [101]
$Sc = \frac{\mu}{\rho D_{BR}}$	**(1.32)**	
$D_{BR} = \frac{k_B C_C T}{3\ \pi\ \mu\ d_p}$	**(1.33)**	

ELECTROSTATIC INTERACTION, E_{ES}		
$E_{ES} = \frac{16\, K_C C_C\, q\, q_p}{3\, \pi\, \mu\, U\, D^2 d_p}$	**(1.34)**	Davenport and Peters [104]
$E_{ES,CD} = \left\{\frac{15\pi}{8}\left(\frac{\varepsilon_p - 1}{\varepsilon_p + 2}\right)\frac{2C_C[q/(\pi D^2)]^2 d_p^2}{3\, \pi\, \mu_g U\, \varepsilon_0 D}\right\}^{0.4}$	**(1.35)**	Nielsen and Hill [105]
$E_{ES,CP} = 2.89\left\{\frac{C_C q_p^2}{3\, \pi^2 \mu_g U\, \varepsilon_0 D^2 d_p}\right\}^{0.353}$	**(1.36)**	Nielsen and Hill [105]
THERMOPHORESIS, E_{Th}		
$E_{Th} = \frac{4a\left(2 + 0.6\, Re^{\frac{1}{2}} Pr^{\frac{1}{3}}\right)(T - T_{as})}{U\, D}$	**(1.37)**	Davenport and Peters [104]
$a = \frac{2\, C_C\left(k_g + 5\, Kn\, k_p\right)k_g}{5\, P(1 + 6\, Kn)\left(2k_g + k_p + 10\, Kn\, k_g\right)}$	**(1.38)**	
DIFFUSIOPHORESIS, E_{Dph}		
$E_{Dph} = \frac{4b\left(2 + 0.6\, Re^{\frac{1}{2}} Sc_w^{\frac{1}{3}}\right)\left(\frac{P_w^{\circ}(T)}{T} - \frac{P_w^{\circ}(Tas)}{Tas} RH\right)}{U\, D}$	**(1.39)**	Davenport and Peters [104]
$b = \frac{TD_w}{P}\sqrt{\frac{M_w}{M_g}}$	**(1.40)**	

1.3.4 Literature Review

In the pertinent literature, there are several works, theoretical and experimental, on the wet electrostatic scrubber as gas treatment system to remove submicrometric particles. They differ on the operative conditions (gas and liquid flow rates, applied voltage, etc.), chamber design, charging mechanisms and type (CDES, ODES, etc.). [106]

In Table 1.4, the main works are reported and among them the studies with operating conditions close to that one of this thesis are deepened.

Table 1-4-Literature review of Wet Electrostatic Scrubbing

References	Scrubber type	L/G	Particles size	Particles charging method	Liquid and droplets size	Liquid charging method	Collection Efficiency
Pilat et al.(1974)[107]	Double chamber: 1) Counter- current 2) Co-current V= 0.56/0.23 m^3	0.85-3.3 Kg/L	Dioctyl-phtalate d_p=0.3-4 µm Q_a=230 L/h c=5.3g/m3	Negative Corona Wire- Plate at V=- 27 kV P- CMR=53mC/kg	Water Q_{L1}= 4.5 L/min 20 nozzle d_D=50 µm Q_{L2}=3.8 gal/min 13 nozzle	Positive induction charging V= 5kv D- CMR=0.56mC/kg	68.8%w for WS 93.6%w for OPES
Balachandran et al (2001)[77], [78]	Rectangular chamber 1.8x1.8x2 m V= 6.5m^3	/	Smoke cigarettes $d_{p3,2}$ = 0.5- 2.5 µm C= 12mg/m^3 Batch System	Uncharged	Tap water Rotary atomizer nozzle Q_L= 16L/h Uncharged $d_{D3,2}$=87 µm charged $d_{D3,2}$=134µm	Induction charging at V=- 8 kV electrical shield a V=+3kV D- CMR= 9mC/Kg	CDES Efficiency rises from 40% (WS) to 90%
Cross et al (2003)[108]	Cylindrical “wind tunnel” D=650 mm V=1.1m^3/h		vg= 0.5-1.25 m/s Q_a=720-1800 m^3/h	Uncharged	Tap Water Air assisted nozzle $d_{D3,2}$=20-40 µm Q_L =2-8 mL/s	Induction charging at V< 3 kV	Efficiency Increases from 73 to 86.5 w

	Cross flow		Coal dust d_p=1-7 µm c= 30-500 mg/m^3				
Yang et al. (2003)[109]	Venturi scrubber, rectangular cross section, 250x250mm	0.4/1000 m^3/m^3 1.8/1000 m^3/m^3	d_p=0.5–5mm Q_a=5400m^3/s	Uncharged	Pneumatic atomiser d_D=30–120mm (1.4–2.8mC/kg)	Induction charging at V=2kV	89% (d_p=0.5mm) (79%—uncharged); 97% (d_p=5mm) (90%—uncharged) (estimated); water:6–24l/h (0.8–1.2l/m^3)
Jaworek et al [79]	Rectangular chamber 1.8x1.8x2m	0.05 L/m^3	Smoke cigarettes $d_{p3,2}$ = 0.5 - 1 µm Stationary 20–30mg/m^3 (uncharged) 4–10mg/m^3 (charged negatively)	Corona at V=- 10 kV	Tap Water Q_L= 41L/h $d_{D3,2}$=80 µm Stainless-Steel Needle ID=0.7 mm	Electro- spraying V=-11+11 kV	80-90% FOR CDES 50-60% FOR OPES

D’Addio et al. (2010)[98]	Cylindrical chamber H=200 mm ID=100 mm	1.15 Kg/Kg	Incense stick d_p=100-450 nm Q_a=0.5-5 m^3/h	Corona charging at V=- 9.5 kV	Distilled water + NaCl QL=0.15- 2.2 mL/ min d_D=0.9 µm Stainless steel needle OD=08 mm ID=0.25 mm	Electro- spraying at V=+3KV	OPES scavenging factor higher than CDES Confirmed by the model
Almuhanna E.A. et al (2012)[110]	V= 0.216 m3		Home dust dp= 14.7 µm	Uncharged	Tap Water Q_L= 120 mL/min d_D= 25-60 mic	Electrostatic nozzle D-CMR= 6.5 mC/Kg	Negatively charged water 80.3 % WS= 62.4 %
Di Natale et al (2014)[111]	Cylindrical reactor H= 3.5 m D=40 cm	1.15 Kg/Kg	Gasoline flame d_p=10-450 nm Q_a= 170 Kg/h	Negative Corona at V=- 13/-15 kV	Tap Water Full cone nozzle spray angle =45° d_D =290 µm QL=195Kg/h	Induction charging at V=- 15kV	WS <1% CDES 35& OPES 91%
Kim et al. (2014)[112]	Acrylic column H= 600mm D= 110 mm Counter-current flow	0.18 L/m3 0.35 L/m3	1,1,3,3-tetramethyl disiloxane Q_a= 0.46 m^3/min Dp= 0.1-1 mic	Uncharged	Nozzle ID= 1.6 mm Q_L= 80/160 mL/min	Electro-spraying Circular ring d=95 mm V= -16,-17,-18 kV	Q_{L1}= 50.8/67/77.1 Q_{L2}=62.2/81.7/91.2

			C= 90 mg/m3				

Pilat e al. (1974)[107] investigated the removal of dioctyl-phthalate particles (dp=0.4-4 µm) in a scrubber made up by two chambers with a volume of 0.56 and 0.23 m3 respectively. The gaseous stream (Q_A= 230 L/h) was fed counter current in the first chamber and co-current in the second one. The liquid was water sprayed by means 20 nozzles and 13 nozzles in the two chambers respectively. The authors studied the influence of Coulomb force in capture efficiency. In fact, the liquid droplets were charged by positive induction at V= 3 kV, while the particles were electrified by negative corona. They found that the overall particle collection efficiency increased from 68.8% in uncharged conditions to 93.6% in presence of electric field.

Balachandran et al. [77], [78] carried out experiments to explore the effect of electric charge on the removal of smoke particles from air. The contact chamber between the liquid and gaseous streams was a chamber 19×1.8×2 m3. The particles were produced by a designed smoke generator with a mean diameter d_{32}= 0.5-2.5 µm and were uniformly distributed in the volume by a fan. The liquid phase was made by water droplets produced by a rotary atomizer (d_{32}= 87 µm) and inductively charged with positive potential. In this configuration, CDES, the collection efficiency was two time better than that of WS configuration. Successively, the authors electrified the gas stream by negative corona too: the efficiency was four times better than the WS configuration.

In 2003, Cross et al. [108] utilized a cylindrical 'wind tunnel' reactor (D = 650 mm) working with air velocity in the range 0.5 to 1.25 m/s. The droplets were produced by an air assisted nozzle (model SU22/42 series manufactured by Spraying Systems Co.) able to produce droplet size ranges from 20 to 400 µm. The droplets were charged by induction at V=2 kV reaching a maximum specific charge of 3 mC/kg. The water in a range of 2 and 8 mL/s, was sprayed cross-flow respect to the air. The particles were coal dust dispersed and carried to the air. Two particle size distributions were studied; the smaller particles distribution ranges from 1 to 7 µm and was not charged. The results obtained showed that the droplet charge allowed an increase of particle efficiency from 73%w to 86.5%w. Based on their results, the authors identified general rules to increase the abatement efficiency, but these results are specific to the design utilized and are difficult to generalize.

Yang et al. [109] performed an electrostatically-assisted Venturi scrubber with a rectangular cross section 250×250×4 mm3. with a converging angle of 15° and a throat section 0.1×0.1×0.55 m3. The gas stream contained particles with d_p= 0.5-5 mm. The liquid spray was produced by a pneumatic atomizer with d_D=30-120 mm inductively charged with positive polarity. The liquid-gas flow rate ratio ranged from 0.4/1000 m3/m3 to 1.8/1000 m^3/m^3. The authors found that for d_p= 0.5 mm, the overall collection efficiency raised from 79% to 89%, while for d_p= 5mm the capture improved from 80 to 97% thanks to the electric contribute.

In 2006, Balachandran et al. [79] conducted experiments on smoke particles capture by means the contact chamber developed in previous study [77], [78] with a multi-electrospray nozzles as charging system for liquid stream. The liquid was de-ionized water with the addition of a surfactant and it was atomized and electrified by electro-spraying in procession mode at both positive and negative polarity. The experiments confirmed that the electrical forces between appositively charged droplets and particles improved the removal efficiency: the concentration of particles smaller than 1 µm was reduced of 80-90%.

D'Addio et al. (2013) [98] developed a wet electrostatic scrubber in lab-scale made by a cylindrical chamber in plexiglass 200 mm high and 100 mm large. The chamber was employed to investigate the removal efficiency of particles produce by incense stick (dp=100-450 µm) and charged by negative corona. The liquid phase was distilled water and sodium chloride with the addition of a surfactant. It was charged by positive electro-spraying exerted in dripping mode so that the droplets diameter was constant and about 0.9 micron. The authors described their results in light of a scavenging model that could take into account the electrical contribute in terms of Coulomb force (OPES configuration) and image forces (CDES configuration). It came out that the scavenging coefficient of WES unit in OPES configuration was higher than that for CDES configuration and far higher than conventional wet scrubbing of submicron particles. Their experiments were conducted by varying the gas temperature in WES too. They observed that when the gas was hotter than the liquid, the efficiency of WES was higher for particles larger than 250-300 nm and lower for particles finer than 150 nm. These results were due to synergic interactions among electric forces and phoretic ones that are not considered in models present in pertinent literature so far [113].

Almuhanna et al. (2012) [110] built an electrostatically-assisted wet scrubber to remove air particulates in a poultry house. The test particles were taken from home dust under controlled conditions, while the liquid was tap water generated by an electrostatic nozzle with mean diameter dD=25-6 µm. The removal efficiency improved from 16.2% for uncharged spray to 72.4% for negatively-charged spray.

In 2014, Di Natale et al.[111] designed a wet electrostatic scrubber made for pilot-scale application. It was made by a stainless-steel cylinder 3.5 m high and 0.4 m large. The particles (d_P= 165 nm) were produced by a gasoline flame generated with a naphtha lamp in open air, while the water droplets (d_D=288.5 µm) were generated by a full cone nozzle. Both particles and droplets were charged by negative corona and positive induction respectively. The experiments aimed to estimate the removal efficiencies of WES technology in WS, CDES and OPES configurations. The results confirmed that electrostatic interactions were more effective than hydrodynamic ones for fine and ultrafine particles.

In fact, the capture efficiencies increased from 1% for WS configuration to 28% when only the droplets were charge and to 88% when both the currents were electrified.

Kim et al. (2014) [112] utilized an acrylic column 600 mm high and 110 mm large in which the gas stream was fed counter current with the liquid phase. The particles were 1,1,3,3, tetra-methyl di-siloxane (dp=0.1-1 µm), while the liquid was made by water droplets produced by electro-spraying at three potentials V=- 16, - 17,- 18 kV. For two different liquid-gas flow rate ratios of 0.18 and 0.35 L/m3, the authors found out that the removal efficiency increased with the potential from 50.8% (uncharged spray) to 77.1% (charged spray) for the first L/G ratio, and from 62.2% (uncharged spray) to 91.2% (charged spray) for the second one.

Carotenuto et al.[18], [111] used an analytical model to predict the particle removal efficiency in industrial Wet Electrostatic Scrubbers. The proposed model considered the overall collision efficiency as the result of inertial impaction, directional interception, Brownian diffusion, electrostatic interactions, thermophoresis, and diffusionphoresis. The work analysed the effect of different processes parameters: contact time, specific water consumption, water/gas relative velocity, size and charge of sprayed droplets. Moreover, the model has been validated by a comparison with different experimental data available in literature, both for charged and uncharged scrubbers. Then it was applied to a reference case study to obtain generalizable results. As regards micrometric particles, the model showed that the collection efficiency increases for higher water/gas relative velocity, with a small effect of droplet diameter and a moderate increase with the droplet charge. On the contrary, for submicron particles, the water/gas velocity played a secondary role in the capture mechanisms, while a substantial increase of collection efficiency was observed by improving the droplet charge level and reducing the droplet size. Regarding the actual performances of water spraying and charging devices, the model predicted that a collection efficiency as high as 99.5% could be obtained reliably in a few seconds with a water consumption of 100 mL/m3 by adopting droplet diameters around 100 µm and charge to mass ratio from 1 to 3 mC/kg, corresponding to droplet charge equal to 10- 30% of Rayleigh limit.

2 MATERIALS AND METHODS

The experimental campaign was aimed to explore the particle removal efficiency of a system made up by a particle growth unit, as precondition technique, and a particle removal device, as either a bubble column or a WES (run as CDES). Two different set of experiments were carried out, as it is indicated in the scheme of experimental campaign in Figure 2.1.

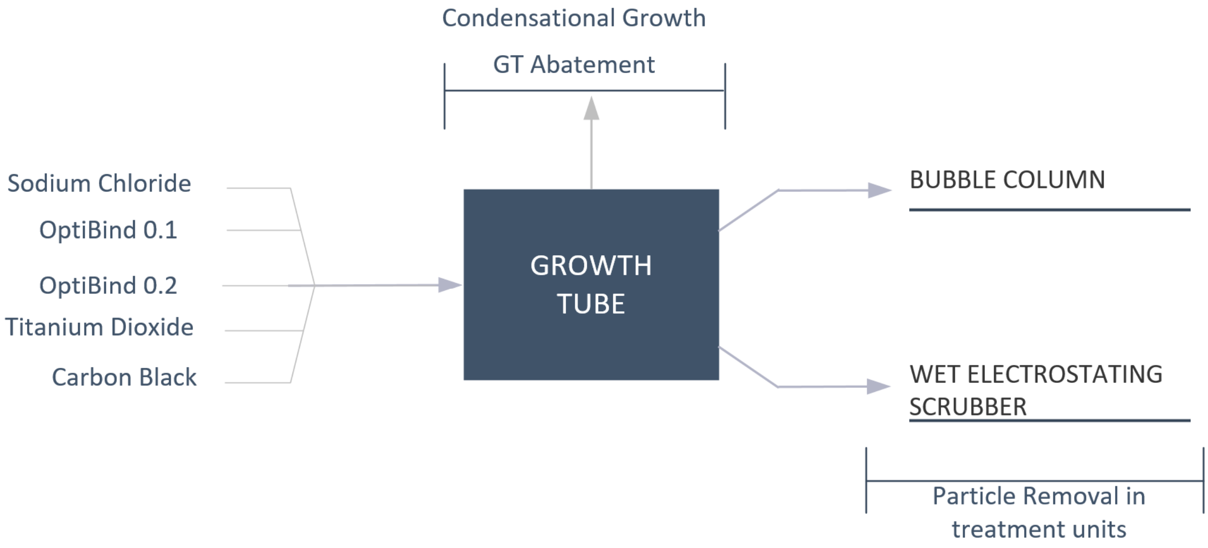

Figure 2-1- Schematic representation f experimental campaign

The experimental rig consisted in two main units: the growth unit (i.e Growth Tube) and the treatment units (i.e. Bubble Column or Wet Electrostating Scrubbing). The first set of experiments was carried out to measure the aerosol growth obtained in the growth unit and to verify the conditions at which the heterogeneous condensation took place. To this aim, it was identified a range of the oversaturation ratio at which the condensation growth was observed. The second set of experiments was meant to measure the particles abatement. It was evaluated in the growth tube and treatments units themselves and in the couplet systems. In this chapter, the experimental setup with a description of each unit, the experimental procedures, the data analysis and the tested materials are reported.

2.1 Experimental Setup

The first set of experiments was run in the lab-scale rig, which was composed by an aerosol generator, a growth tube (GT) particle diagnostic units and ancillary devices.

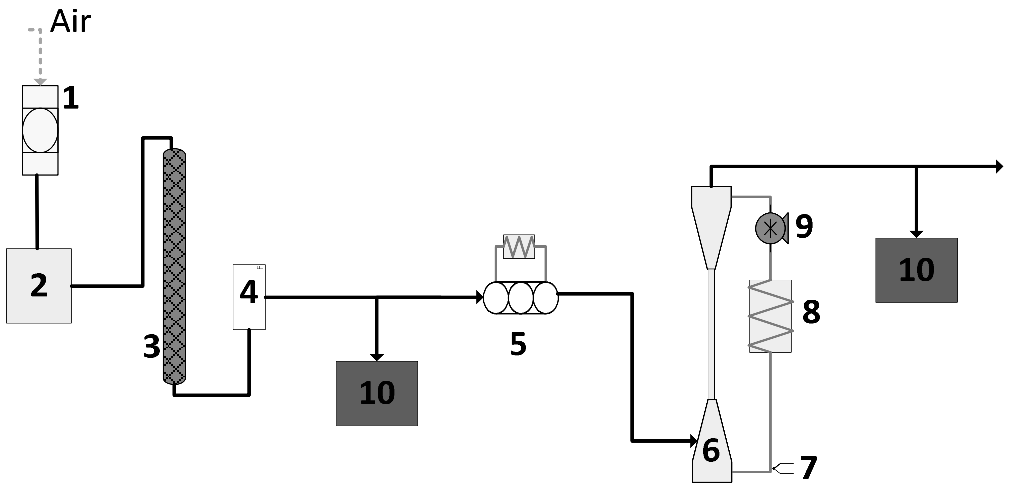

Figure 2-2 Experimental set up for heterogeneous condensation study: 1-HEPA filter; 2-Topas ATM221 aerosol generator; 3-Diffusion dryer; 4-Flowmeter; 5-Saturator; 6-Growth tube; 7- Thermocouple; 8-Thermostatic bath; 9- Verder gear pump; 10-Monitorining system.

Figure 2.2 shows the experimental set up aimed to the heterogeneous condensation study. The HEPA filter pre-treated the incoming air flow that was sent directly to the aerosol generator TOPAS ATM $221^{®}$ in order to develop an aerosol model.

The particles laden gas was produced with a commercial aerosol generator (TOPAS ATM 221), which details are illustrated ahead. The generated aerosol passed through a diffusion dryer to remove water and produce a dry aerosol, whose flow rate was controlled by a flowmeter. The gas passed through a bubble saturator at 30°C and then finally entered the growth tube, where the aerosol grows. Gas sampling points were placed at the inlet of the saturator and at the outlet of the growth tube.

The Figure 2.3 shows the experimental rig for the particle abatement study ether with the bubble column or the WES.

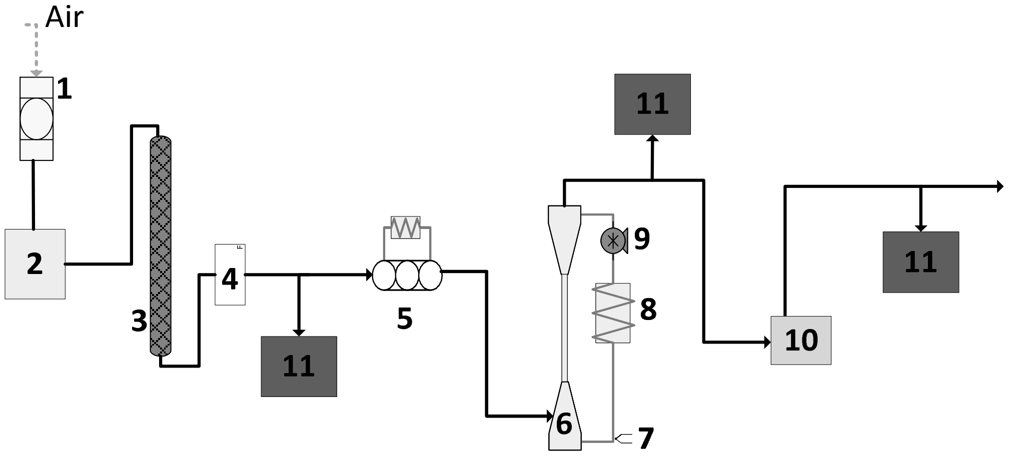

Figure 2-3 Experimental set up for particle abatement: 1-HEPA filter; 2-Topas ATM221 aerosol generator; 3-Diffusion dryer; 4-Flowmeter; 5-Saturator; 6-Growth tube; 7-Thermocouple; 8-Thermostatic bath; 9-Verder gear pump; 10- Either Bubble Column or wet electrostatic scrubber; 11- Monitoring system

The experimental set up is like the previous one, except that after the Growth Tube the gas was sent to the treatment device. Gas sampling points were placed at the inlet of the system and at the outlet of the growth tube and the removal units.

All the pipelines were PTFE flexible tube with internal diameter of 6 mm and were thermally insulated with a sheet of heat insulation tape and set as short as possible to minimize environmental interferences.

The diagnostic systems included devices to measure the temperature, relative humidity, and aerosol size distribution.

All the apparatus components and the diagnostic systems were described below.

HEPA filter

Whatman® in –line HEPA Cap, Figure 2.4, was used throughout the scientific, research and industrial environments, in a variety of air and gas filtration applications where high retention, dirt-holding capacity were required.

It retains 99.97% of all number of particles with a diameter bigger than 0.3 μm in air.

Figure 2-4 Whatman® HEPA filter

It is worth noticing that during blank experiments, feeding only compressed air in the system, the total particles number was of few units per cm3.

TOPAS® ATM 221

The analysed aerosol was obtained by using the TOPAS® ATM 221, Figure 2.5, equipped with a Laskin nozzl. This aerosol generator is able to produce a particles laden gas by feeding a suspension of the tested particle. The atomizer is the key part of the ATM 221. It is made of high quality stainless steel and works as a two-substance nozzle, based on the injection principle. The Laskin nozzle is immersed in the liquid suspension and injecting high velocity stream of compressed air produces an aerosol with a particle size distribution depending on the tested particles. The TOPAS® ATM 221 can compress air up to 2.5 bar and generate an aerosol with a gas flow rate of roughly 300 L/h with a number concentration depending on the initial particle concentration in the suspension and the adopted pressure.

Figure 2-5 Aerosol generator TOPAS® ATM 221

TOPAS® Diffusion Dryer DDU 570

The TOPAS® Diffusion Dryer DDU 570, Figure 2.6, was an additional equipment for the Aerosol Generator ATM 221 that was operated by compressed air.

The aerosol to be dried was streaming through a screen porous pipe which is surrounded by Silica Gel (desiccant with indicator) serving as drying agent. The Silica Gel caused a very dry atmosphere. The moisture in excess in the aerosol moved into the dry environment by the effect of diffusion.

Because the aerosol did not get into direct contact with the drying agent, only a very low particle loss occurred.

Figure 2-6 Diffusion Dryer DDU 570 with silica gel

Aerosol Saturator System

The bubble saturator system was composed by a Haake DC30, Figure 2.7, cooling unit. It consisted of a series of four ampoules filled with distilled water and covered by a jacket in which water flows at the controlled temperature of 30°C. The jacket aimed at the ampoules heating, so to humidify the passing aerosol. The outgoing aerosol presented a 30-31°C temperature and 100% of humidity.

Figure 2-7 Bubble saturator and Haake DC30 cooling unit

Growth Tube

Figure 2.8 shows the growth tube in which the heterogeneous condensation of the vapour occurred over the particles. It consists in a glass cylinder with a length of 40 cm and an internal diameter of

1.5 cm. The tube size was designed by taking into account the diffusion rate of vapour from the cylinder walls to tube centreline and the need of minimizing the interferences between the gas and the liquid flows. The liquid was fed into a bowl placed at the top of the cylinder and was filled up to the brim until a water film fell along the internal wall of the tube. The water was collected in a flask placed at the bottom of the cylinder. A gear pump guaranteed a uniform water circulation with a flow rate of 0.06 L/min.

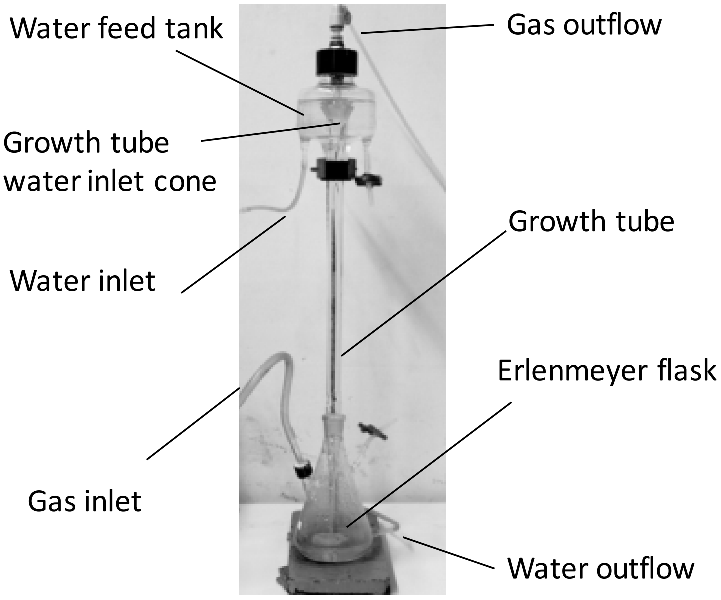

Figure 2-8 Scheme of the growth tube

The film temperature and the gas rate controlled the gas supersaturation level. In the growth tube, vapour condensation occurred until the temperature of the gas was lower than the one of the liquid film. To this aim, the liquid film was kept at a desired temperature, T_w, using a thermostatic bath, and liquid temperature at the bottom of the growth tube was measured. The gas flow, monitored with a flowmeter, entered the growth tube from the bottom flask, so that the water and the gas were in counter-current flow.

Bubble Column

The bubble column, Figure 2.9, consists in a glass bottle (with a 10 cm internal diameter and a 20 cm height) having a porous ceramic distributor (8 cm large) placed 1 cm above the bottom and a gas outflow at the bottle cap. The column was filled with nine cm of HPLC water at room temperature and its pressure drop was roughly 350 mmH_20 [114].

Figure 2-9 Bubble column scrubber

Wet Electrostatic Scrubber

The wet electrostatic scrubber, Figure2.10, consisted in a plexiglass cylinder 40 cm high and with an internal diameter of 4.5 cm. The WES is equipped with an electrospray housed on the top of the chamber. The lateral surface of the reactor presents two 10 mm holes for gas inlet and outlet, arranged at opposite side from each other.

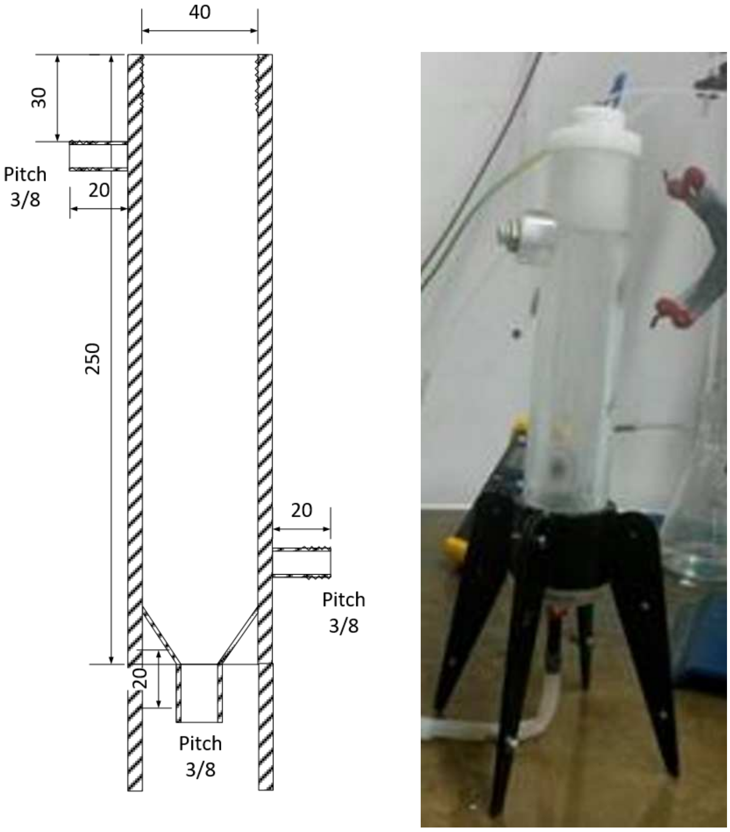

Figure 2-10 Wet electrostatic scrubber

A hole for water draining was placed at the bottom of the column. The electrospray, Figure 2.11, consists in a needle put coaxially to a grounded steel flat ring, encased in a PTFE box, with the tip at 1 mm below the lower surface of the ring. The needle is connected to a high voltage power supply device.

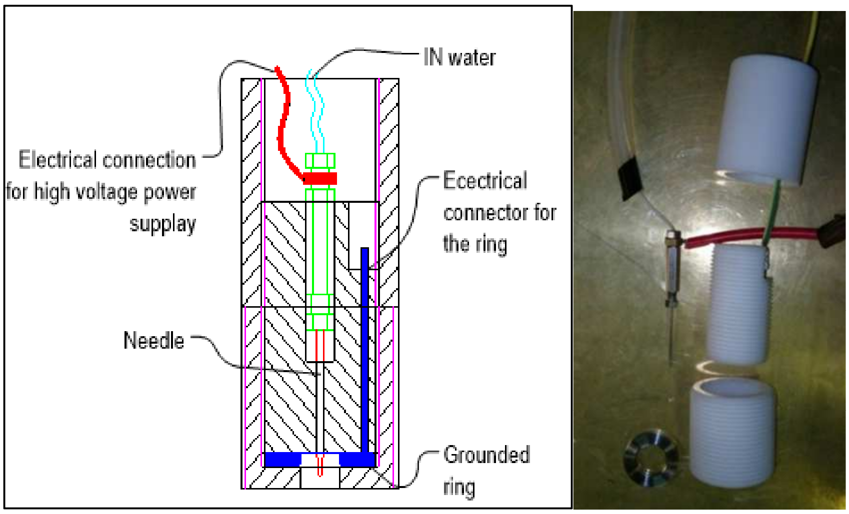

Figure 2-11 Charged droplets generator assembly

The liquid was fed into the needle using a Harvard syringe pump. The pump guaranteed a liquid flow rate ranging from µL/min up to mL/min. The high voltage system consisted in a Bertan 230 B supplied by Spellmann HV with reverse polarity up to 20kV.

Preliminary analysis was run to investigate the spray regimes establishing in this system. The operative conditions envisaged a liquid flow rate spanning from 1 to 6 mL/min and a positive potential from 1 up to 5 kV, the maximum value before discharges occurred.

Optical tests were carried out to investigate the instauration of different spray regimes. Figure 2.12 shows the regimes observed in this work at different couple liquid flow rate-high voltage.

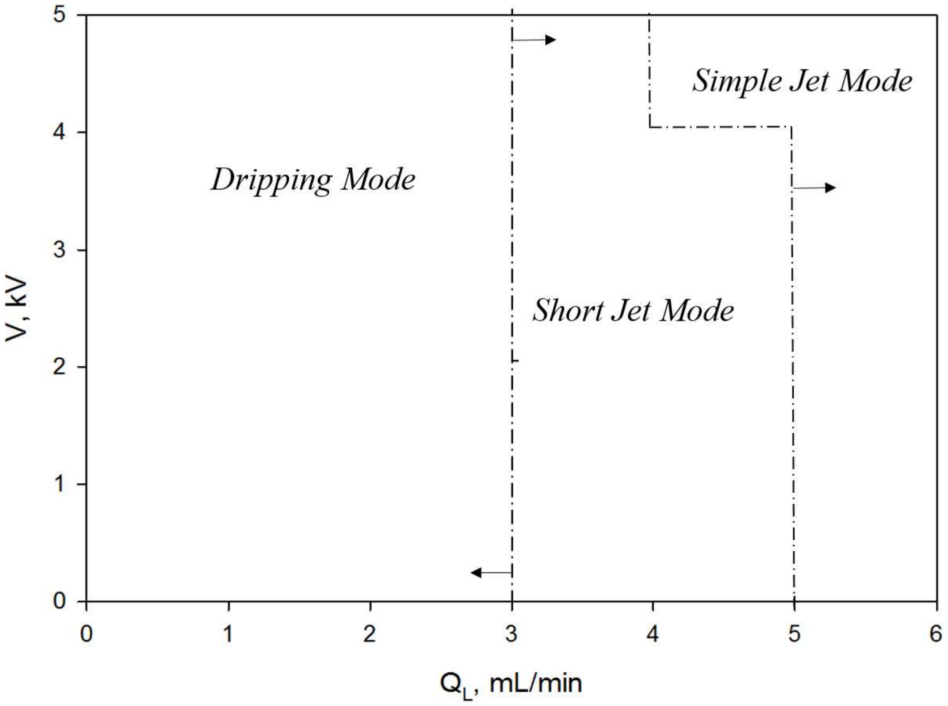

Figure 2-12- The spraying regimes for distilled water at positive polarity

The results were in accord to regimes described by Agostinho et al. (ag 2012). For the liquid flow rates exerted in this electrospray higher that those usually used in the pertinent literature (gomes, jaw, ganan calvo), we did not observe the transition from dripping mode to cone-jet mode as the voltage and the flow rate increased. The transition regime was labelled as short jet mode. It was identified by an acceleration of the liquid droplets caused by the electric field. It elongated the liquid and a short jet and smaller droplets were formed. By increasing both the voltage and the flow rate, the regime stabilized in the so-called simple jet mode. It was represented by a liquid jet with a constant diameter from which the droplets detached in dimension and frequency depending on operating conditions. In Figure 2.13, the observed regimes for Q_L= 4 mL/min are showed.

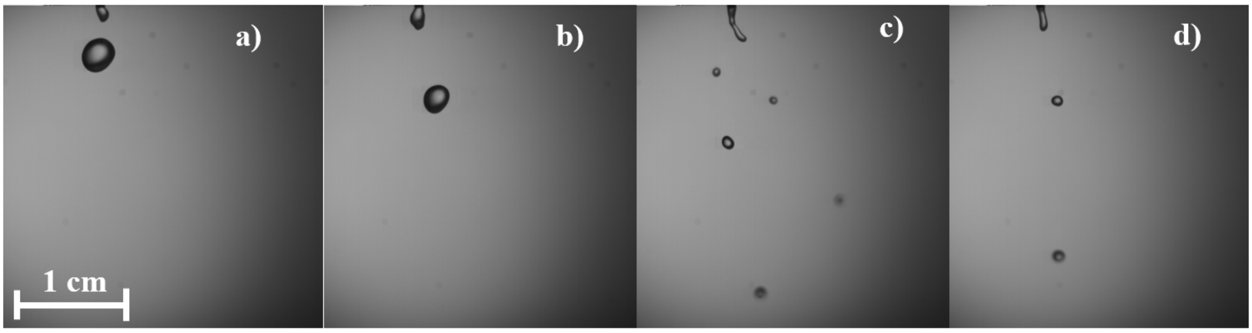

Figure 2-13- Regimes of electrospray at QL= 4 mL/min and V= 0 (a), 2 (b), 4 (c) and 5 kV (d).

The operating conditions of the tests with the WES coupled with the Heterogenous Condensation (HC) HC were 4 mL/min and 4 kV because in these conditions a stable simple-jet mode was observed, as reported in the Fig 2.13, and or the possibility of better highlighting particle efficiency improvements. In fact, a preliminary analysis was run to study the removal efficiency of the single WES at the different observed regimes. It was observed that in dripping mode the efficiency reached the maximum value of roughly 20%, while in jet mode the removal efficiency increased up to 80% at 5 mL/min and 5 kV.

The Diagnostic Systems

The diagnostic systems included devices for measure of temperature, relative humidity, and aerosol size distribution. The measurement of temperature was possible by means a thermocouple connected with a reader (RS mod.206-3722), instead, the datalogger DO2003® was used to measure the humidity.

The aerosol size distributions were monitored with two instruments: the scanning mobility particle size analyser SMPS TSI Model 3910 and the Laser Aerosol Spectrometer TSI 3340.

The Scanning Mobility Particle Sizer™ TSI 3910 allowed measuring solid particles in the range 10- 420 nm, appropriate for the submicrometric particles tested in this work, and can operate only at low humidity and without water droplets.

Figure 2-14 TSI® nanoscan model 3910

The Nanoscan 3910 is an electrical mobility based sizing technique. Electrical mobility, or the ability of a particle to traverse an electric field, is a convenient method to measure particle size, because it can be directly measured and is a first principle function of size. Electrical mobility is typically measured by using a Differential Mobility Analyzer (DMA). Inside a DMA, a charged aerosol particle experiences an electric field, causing it to move through the gas in which it is suspended. The particle also experiences an opposing drag force from the gas flow which can be calculated using Stokes law. These forces can be equated and the electrical mobility of the particle can be calculated. Figure 2-15 shows the operating principle of the instrument.

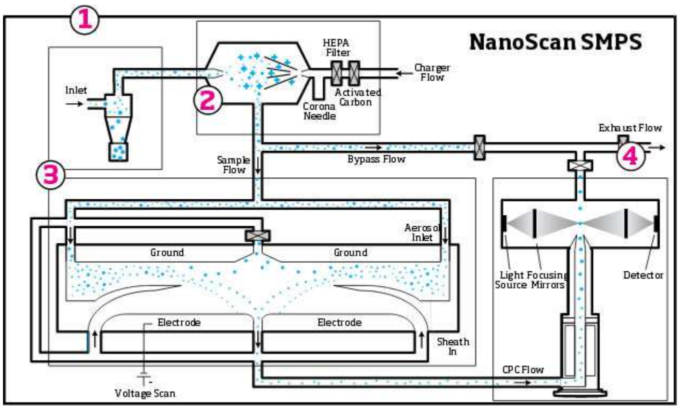

Figure 2-15 Nanoscan 3910 operating principle

Since the sample gas has to be dry and free of water drops, before entering the SMPS, it passes through a heater and a dilution system

The dilution system PALAS KHG 10, see Figure2.16, was a mixing chamber where an air stream coming from the filter HEPA was mixed with the aerosol and a volumetric dilution ratio of 10 and a temperature of 120°C was set up. These indications were also suggested by Diebold [114].

Figure 2-16 PALAS® KHG 10

The TSI 3340 can monitor a solid or a liquid aerosol with particle size between 90 nm and 7.5 µm. The principle of operation of the TSI 3340 was the light scattering, which depended on the refractive index of the monitored materials. The instrument was calibrated with polystyrene particles which have a refractive index lower than that of the water [1]. It means that the instrument underestimates the size of a water particle and we can say even less about the measure of a solid-liquid aerosol, since its refractive index is unknown. Therefore, this system is the only viable choice to treat this kind of aerosol, but we understand that the experimental results only have a qualitative value. [64] The Size range covered of the TSI 3340 partially covers the size range of submicrometric particles.

Figure 2-17 TSI ® Laser Aerosol (LAS) Spectrometer 3340

2.2 Materials

The experiments were carried out with different kind of particles characterized by a size particle spanning in the submicrometric range. The tested materials were calibrated polystyrene OptiBind particles with a mean volumetric diameter of 100 nm and 200 nm, titanium dioxide, sodium chloride, and carbon black powder.

The calibrated polystyrene particles were used in order to provide experimental data on which a nucleation model could be validated or developed. The salt and the TiO_2 were studied to examine the growth and the abatement of insoluble and soluble inorganic particles, respectively. Finally, the carbon black was employed because of its physical-chemical characteristics that could be assimilated to soot particles deriving from partial combustion processes.

The aerosols were obtained producing a liquid suspension of particles and ultrapure water, HPLC grade supplied by Sigma-Aldrich.

All the particles suspension solutions, expect the carbon black, were put 20 min in an ultrasound bath at 80 MHz in order to optimize the submicronic particles dispersion. A fully description of the methodology is described in the specific section.

Sodium chloride

Sodium chloride is an ionic compound with the chemical formula NaCl, representing a 1:1 ratio of sodium and chloride ions. Sodium chloride is the salt most responsible for the salinity of seawater and of the extracellular fluid of many multicellular organisms. It is largely used in many industrial processes, and it is a major source of sodium and chlorine compounds used as feedstocks for further chemical syntheses. A second major application of sodium chloride is de-icing of roadways in sub- freezing weather. Each ion is surrounded by six ions of the opposite charge. The surrounded ions are located at the vertices of a regular octahedron.

The characteristic hygroscopicity allows a high interaction among water gas and salt, promoting nucleation and growth phenomena. Due to its hygroscopic behaviour, the sodium chloride has a contact angle with the water of 0°, indicating a strong wettability.

The salt aerosol was generated by feeding to the aerosol generator a liquid solution composed by 0.31 grams of NaCl dissolved in 80 ml of HPLC water. The used salt was the common sodium chloride for food.

The averaged particles number distribution measured by both diagnostic systems is shown in the Figure 2.18.

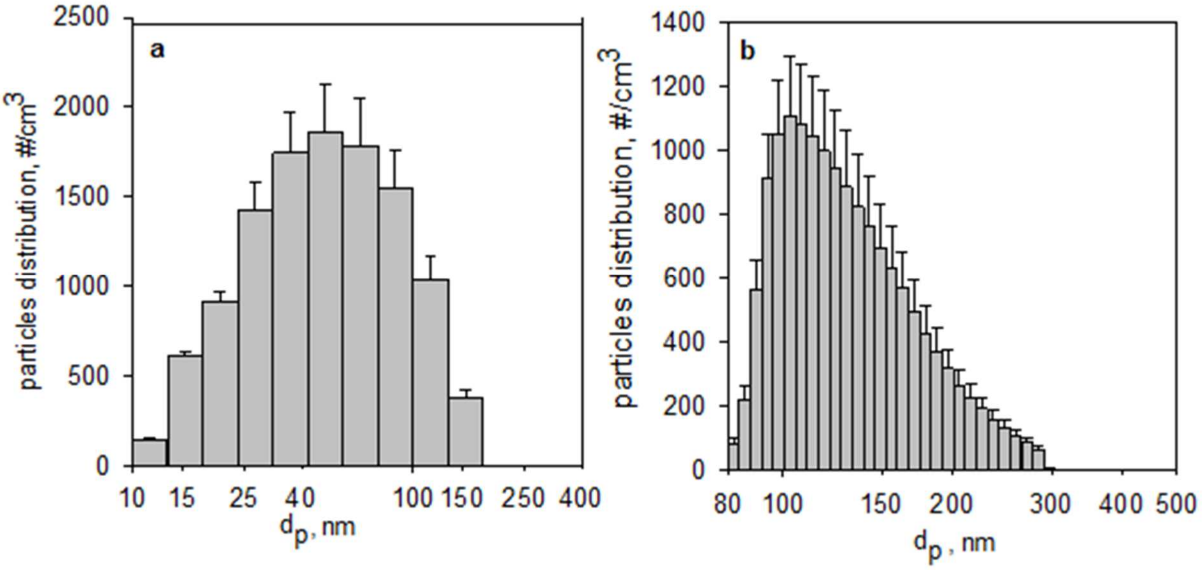

Figure 2-18 Aerosol Size Distribution (ASD) at inlet of growth tube of NaCl measured by Nanoscan 3910 (a) and TSI$^{®}$ 3340 (b)

The salt aerosol size distribution at the inlet of growth tube has a polydisperse size distribution ranging from 10 to 300 nm. The distribution revealed by the TSI 3910 had a mean diameter of 57 nm and a standard deviation of 34 nm, while that one measured by the TSI 3340 presented a mean diameter of 135 nm and standard deviation of 40 nm.

Calibrate Polystyrene Particles

Polystyrene (PS) is a clear, amorphous, nonpolar commodity thermoplastic that is easy to process and that can be easily converted into many semi-finished products like foams, films, and sheets. It is one of the largest volume commodity plastic, comprising approximately seven percent of the total thermoplastic market. It is a very good electrical insulator, has excellent optical clarity due to the lack of crystallinity, and has good chemical resistance to diluted acids and bases. It is also easy to fabricate into a large number of finished goods since it is a viscose liquid above its glass transition temperature that can be easily shaped. However, polystyrene has several limitations. It is attacked by hydrocarbon solvents, has poor oxygen and UV resistance, and is rather brittle, i.e. it has poor impact strength due to the stiffness of the polymer backbone. Furthermore, its upper temperature limit for continual use is rather low due to the lack of crystallinity and its low glass transition temperature of $T_g = 373$ K.

Polystyrene is a not biodegradable plastic and resistant to photolysis. It is a major contributor to the debris in the ocean. Although recyclable, polystyrene is not recycled in many parts of the world.

Two tested aerosol were formed by polystyrene nanoparticles with a nominal volumetric mean diameter of 98.5 nm and 198.5 nm, supplied by the Thermo-scientific under the commercial name of OptiBind 0.1and OptiBind 0.2, respectively, as a 10% w/w water suspension. The suspension also contains 0.05% w/w sodium azide as surfactant. The aerosol generator was fed with 50 ml of water HPLC grade (Sigma-Aldrich) in which 2 ml of either OptiBind 0.1 or OptiBind 0.2 suspensions were added.

The fig 2.21-2.22 show the aerosol size distribution at the inlet of the growth tube of the OptiBind 0.1 and OpriBind 0.2, respectively.

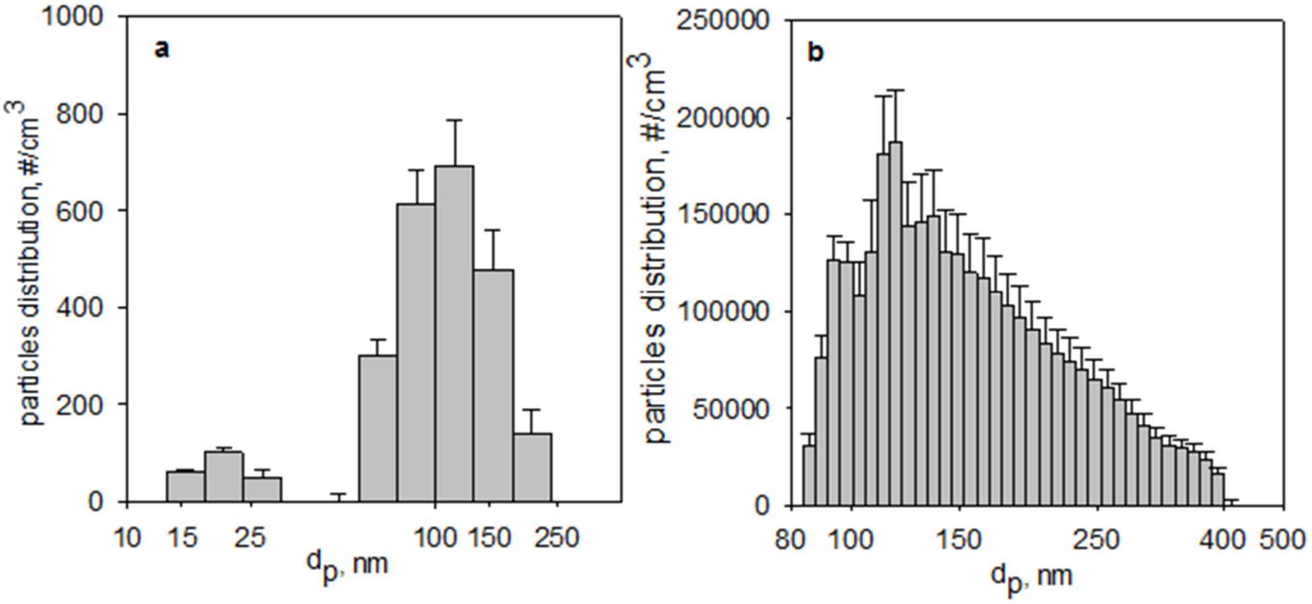

Figure 2-19 Aerosol Size Distribution (ASD) at inlet of growth tube of Optibind 100 measured by Nanoscan 3910 (a) and by TSI®3340 (b)

It was found that both instruments aerosol size distributions have a median value roughly at 98 nm, as expected. The TSI 3910, Figure 2.21 (a), measured a second peak of the distribution at 23 nm attributable to the presence of the surfactants in the supplied solution and the particles traces of water. According to TSI 3910, the polystyrene particles distribution spanned from 41 nm to about 176 nm and the total particle concentration in the gas was 3500 #/cm^3 (Figure 2.21 (a)), while according to TSI 3340 the ASD varied from 90 (the lower size limit of the instrument) to 400 nm and the total particle concentration in the gas was 3200 #/cm^3 (Figure 2.21 (b)). This discrepancy and the different number concentration were due to the different measurement principle of the two instruments and to the aerosol dilution, required before entering the TSI 3910.

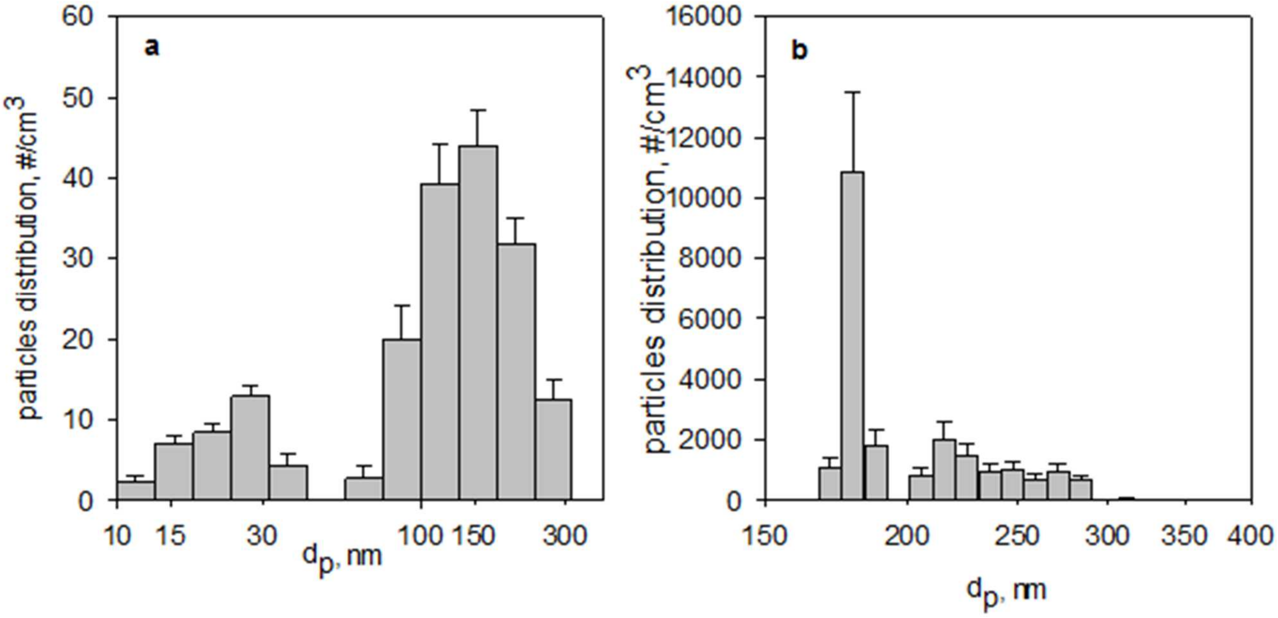

Figure 2-20 Aerosol Size Distribution (ASD) at inlet of growth tube of Optibind 200 measured by Nanoscan 3910 (a) and by TSI®3340 (b)

It was found that both instruments measured a marked peak at roughly 180 nm, as expected. The TSI 3910, Figure 2.22 (a), measured a second peak of the distribution at 23 nm attributable to the presence of the surfactants in the supplied solution and particles traces of the water. The TSI 3340 revealed a distribution tail from 200 to 290 nm.

Table 2.1 reports the count mean diameter(CMD), the Sauter diameter(d_{32}) and the standard deviation (σ) of the tested aerosols evaluated with both instrument measures.

Titanium Dioxide

Titanium dioxide is a naturally occurring mineral that is mined from the earth then further processed and purified for use in consumer products Titanium dioxide, also known as titanium (IV) oxide or titania, with molecular formula TiO_2 and molecular weight 79.87 g/mol, is a kind of powder. Titanium dioxide color is white and is a soft solid that melts at 1800°C. It has special application, such as insulation, corrosion, flags, etc. It is polymorphous and it exists in three types of crystal structures: rutile, anatase and brookite. Only rutile is used commercially. Titanium dioxide is safely used in many products from paint and food to drugs and cosmetics. It also plays a critical role in some sunscreen products to protect skin from the sun’s harmful ultraviolet radiation. It is insoluble in water, dilute alkali, dilute acid, but soluble in hot concentrated sulfuric acid, hydrochloric acid, nitric acid.

Although titanium dioxide is insoluble in water, it has a finite contact angle of 52°[37], that makes it a material with high wettability.

The titanium dioxide aerosol was generated by using a liquid solution composed by 0.32 mg of TiO_2 with 80 ml of HPLC water. The titanium oxide was supplied by Sigma- Aldrich. The Figure2.19 shows the inlet aerosol distribution of titanium dioxide revealed by the TSI 3910 (a) and TSI LAS 3340 (b).

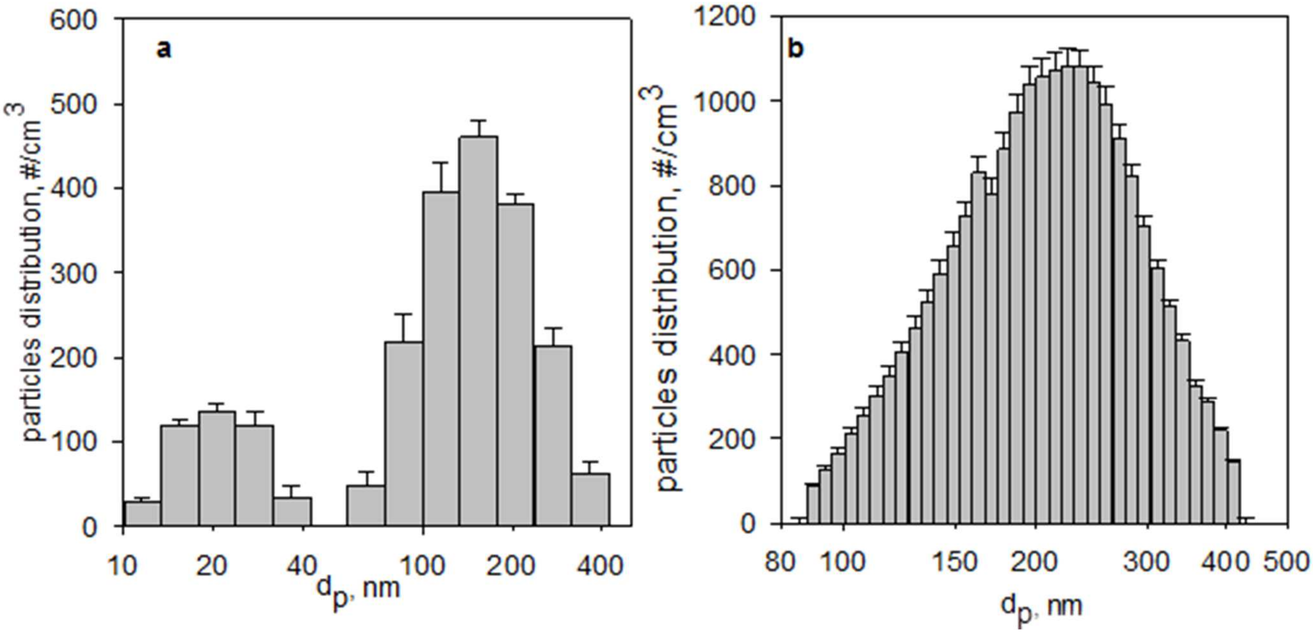

Figure 2-21 Aerosol Size Distribution (ASD) at inlet of growth tube of TiO_2 measured by Nanoscan 3910 (a) and by TSI®3340 (b)

The aerosol size distribution at the inlet of growth tube of the titanium dioxide measured by the TSI 3910, Figure2.17 a), had a bimodal distribution: a first peak at 150 nm due to the TiO_2 particles and the second peak at 20 nm due to the particle traces of the water. The TSI 3340 revealed a wide distribution with a peak at 220 nm and a standard deviation of 39 nm. Both diagnostic system revealed an aerosol size distribution ranging from 90 to 400 nm.

Carbon Black

Carbon black is virtually pure elemental carbon in the form of colloidal particles that are produced by incomplete combustion or thermal decomposition of gaseous or liquid hydrocarbons under controlled conditions. Its physical appearance is that of a black, finely divided pellet or powder. Its use in tires, rubber and plastic products, printing inks and coatings is related to properties of specific surface area, particle size and structure, conductivity and colour. Carbon black is not soot or black carbon, which are the two most common, generic terms applied to various unwanted carbonaceous by-products resulting from the incomplete combustion of carbon-containing materials, such as oil, fuel oils or gasoline, coal, paper, rubber, plastics and waste material. Soot and black carbon also contain large quantities of dichloromethane- and toluene extractable materials and can exhibit an ash content of 50% or more. Carbon black is chemically and physically distinct from soot and black carbon, with most types containing greater than 97% elemental carbon arranged as aciniform (grape- like cluster) particulate. On the contrary, typically less than 60% of the total particle mass of soot or black carbon is composed of carbon, depending on the source and characteristics of the particles (shape, size, and heterogeneity). Two other commercial carbonaceous products often confused with carbon black are activated carbon and bone black. Each is produced by processes different from commercial carbon black and possesses unique physical and chemical properties.

The carbon black is insoluble in water, therefore, after a literature research (Black et al. 1996), it was found that a water-ethanol solution at 50% in volume would be feasible to obtain a homogeneous suspension.

The carbon black is highly hydrophobic and with a low wettability has a contact angle of roughly 90 [37]

The carbon black used in this work was supplied by Sigma-Aldrich as nanometric powder. The carbon black aerosol was generated by feeding a suspension of 1.4 mg carbon black nanoparticles mixed with a water-ethanol solution 50% in volume. Since the homogeneous suspension started to disappear after 20 min, the tests envisaged the use of three different solution that were changed every 20 min.

The Fig 2.20 shows the aerosol size distribution of the carbon black at the inlet of GT measured by the TSI 3910 (a) and the TSI 3340 (b).

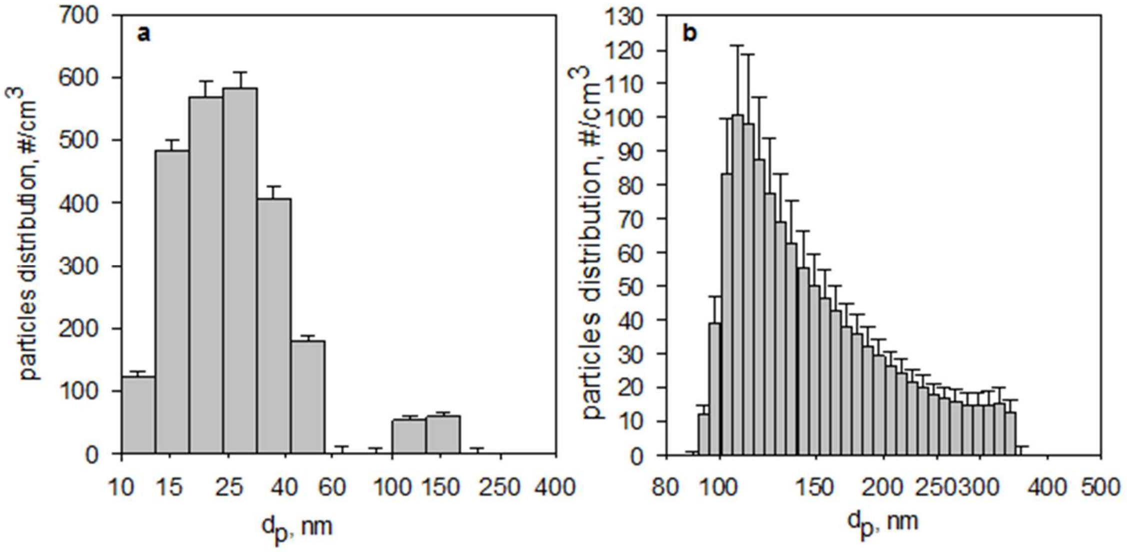

Figure 2-22 Aerosol Size Distribution (ASD) at inlet of growth tube of Carbon Black measured by Nanoscan 3910 (a) and by TSI®3340 (b)

The aerosol size distribution at the inlet of GT had a primary distribution at nanometric scale ranging from 10 to 60 nm with a peak at 25 nm. It is possible to observe a second fraction of carbon black particles characterized by a size of roughly 150 nm, revealed by both instruments. Table 2.1 resumes the ASDs properties of all materials as the count mean diameter (CMD), the mode and standard deviation σ, the Sauter diameter d_{32}.

Table 2-1-The mode, CMD, d_{32}, σ and pertinent range for each tested aerosol.

Tested aerosols	**Contact angle, °**	**mode**		**CMD, nm**		**d_{32}, nm**		**σ, nm**		**Pertinent range, nm**	
		TSI 3910	TSI 3340	TSI 3910	TSI 3340	TSI 3910	TSI 3340	TSI 3910	TSI 3340	TSI 3910	TSI 3340
Sodium chloride	-	49	103	57	135	96	161	34	40	11.5- 154	90- 283
Titanium dioxide	52	154	113	134	136	225	160	68	39	65-365	90-410
Carbon black	92	27	108	24	156	33	203	10	57	11.5-49	94-340
OptiBind 0.1	82	86	118	89	192	126	257	36	79	41-175	86-391
OptiBind 0.2	82	154	179	124	201	191	212	55	31	99-313	171- 283

2.3 Experimental campaign and procedure

For each tested aerosol, two different set of experiments were carried out. The first one was carried out to measure the aerosol grown obtained in the GT and to verify the conditions at which the heterogeneous condensation took place. Since at the exit of the growth tube a solid-liquid aerosol was generated, it was not possible to monitor it with the SMPS TSI 3910 and so the TSI 3340 was used. The aerosol size distributions were monitored at the GT exit and their evolution was studied by varying the water film temperature of the GT in the range 30-70°C.
The second set of experiments was meant to measure the particles abatement in the system GT-BC and GT-WES, monitoring the aerosol size distribution of the aerosol at the inlet of the system and at the outlet of both the growth and the abatement units. To this aim the SMPS TSI 3910 was used. As benchmark, the removal efficiency of the BC and WES bypassing the GT were evaluated as well.

The experiments were performed at a gas flow rate of 48 L/h with the GT operating at water film temperature between 30 and 70°C. Table 2.2 summaries the experimental tests.

Table 2-2- Summary of experimental tests

Test, N°	T_w, °C	Particle abatement	Particle Growth
1	-	WES/BC	-
2	30	GT-BC/GT-WES	GT
3	40	GT-BC/GT-WES	GT
4	50	GT-BC/GT-WES	GT
5	60	GT-BC/GT-WES	GT
6	70	GT-BC/GT-WES	GT

To assure the accuracy, reliability, and reproducibility of the collected data, all tests were performed in triplicate and average values with errors bars were reported. Before each test, we regularly performed three types of blank tests.

The first set of blank tests (named A) aimed to measure the size distribution of an aerosol, produced by feeding the aerosol generator with air, at the exit of GT operating at different water film temperature T_w. In this way, the eventual traces of particles monitored by the diagnostic systems at the exit of the GT were only ascribable to the occurrence of homogeneous condensation or to water droplets entrained in the gas from the liquid film.

The second set of blank tests, named B, consisted in feeding HPLC-grade water to the aerosol generator and was aimed to observe the presence of particles in the gas stream deriving from the salt content in the water or water drops which escaped the dryer and their possible growth in the GT.

The third blank test, named C, was run by feeding the aerosol generator with the all the tested particle solution and by stopping the water circulation in the growth tube. In this way, it was possible to check the occurrence of particle coagulation and of particle depletion due to the passage along the pipe line, from the entrance to the GT outlet sampling points.

The results of the tests A showed that no water droplets were entrained in the gas and no homogenous condensation occurred at any temperature. In tests B, the ASDs of HPLC water were measured both with the SMPS TSI 3910 and the LAS TSI 3340 and are reported, in Figure 2.23 a) and b), respectively.

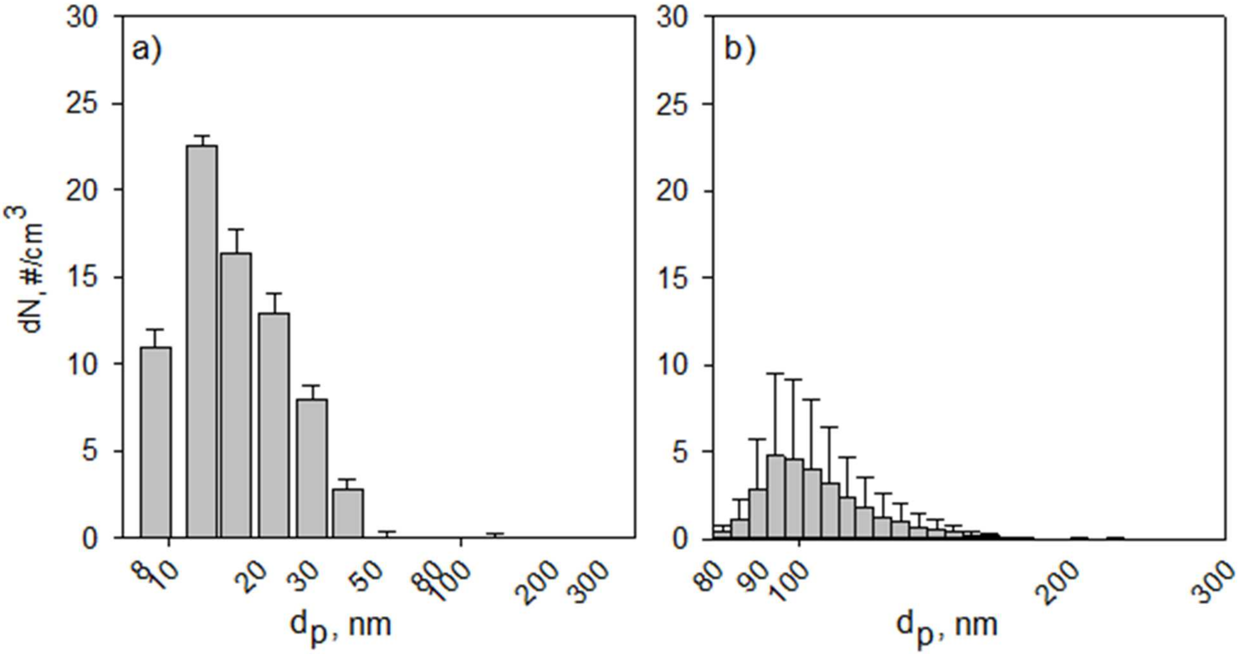

Figure 2-23 Typical particle size distribution of HPLC water obtained with TSI Nanoscan 3910 (a) and LAS TSI 3340 (b) in tests B.

The total particles number of the used water at the inlet of the GT measured by the SMPS TSI 3910 and LAS TSI 3340 were 73 and 30 #/cm^3, respectively. This aerosol size distribution was probably ascribable to two different kind of particles. The TSI LAS 3340 revealed that water droplets probably escaped from the dryer system (Figure 2.2 (3)). These were evaporated in the dilutor system and cannot be measured by the TSI 3910. Moreover, trace of nanoparticles of roughly 20 nm were revealed by the TSI 3910 ascribable to trace ions and impurities present in the HPLC-grade water, which are also reported in its technical datasheet (Sigma-Aldrich). Indeed, the blank tests B results at the exit of the GT showed that the particle traces in the HPLC-water enlarged with the temperature, giving an appreciable contribution to total particle number. Although the total number concentrations were low compared with the normal particle number produced during tests (about 3000 #/cm^3) all the aerosol size distributions used in the data analysis were evaluated subtracting the contribution of these enlarged particles. Finally, the tests C revealed that particle depletion and particle coagulation phenomena may be neglected, since the particle size distribution measured at the sampling points differed less than 3-4 %, which is within the experimental accuracy. These results allowed to attribute the overall removal efficiency of the GT to the water film.

A preliminary test to verify the existence of an upper limit of particle diameter above which all the particles were collected by the GT and the pipelines, was accomplished. To this aim, polystyrene calibrated nanoparticles with a mean volumetric diameter of 100,200 and 400 nm were tested. The aerosol size distributions at the exit of the GT operated a different water film temperature were monitored.

2.3.1 Experimental protocol for particle enlargement in the growth tube

This section describes the procedures used to perform tests on the particle growth reached in the growth tube by varying the oversaturation level. The final experimental protocol adopted was the result of careful and meticulous considerations aimed to minimize the error and the interferences from the environment. A particular attention was addressed towards the water in the GT and the pipelines. In fact, the water in the GT was changed at the beginning of each test in order to avoid particle entrainment at the interface from the liquid into the gas. The pipeline (has been) was cleaned at each test to remove the condensed water that could capture the grown particles, so altering the measurements. Each test lasted 5 min, after preliminary tests in which was observed that the steady state conditions were reached after about 1 min.

A list of operations executed during the test is reported below:

Test preparation:

1. The thermostatic bath is switched on and adjusted in order to have the desired water temperature, T_w, in the growth tube.
2. The saturator is switched on and fixed at the temperature of 30°C.
3. Flow rate sampled by the Laser Aerosol Spectrometer is adjusted in order to have an isokinetic sampling.

4. The particles suspension solution is prepared and put for 20 min in an ultrasound bath at 80mHz in order to optimize the submicronic particles dispersion.
5. The blank tests A, B and C are carried out.

Test execution:

6. The solution is fed to the aerosol generator and the pressure is set to the desired value in order to obtain a number particle concentration suitable for the monitoring system (3000 particles /s) and spanning from 1000 to 3000 particles/cm^3 at the inlet.
7. The valve 1 are set to measure the aerosol inlet to the growth tube by means the TSI LAS 3340 and each measure lasts 5 min.
8. The valve1 are set to measure the growth tube outlet by means the TSI LAS 3340 and each measure lasts 5 min.
9. The temperature of the thermostatic bath is adjusted in order to obtain another water temperature in the growth tube.
10. The test continues from the seventh step, after that the temperature of the T_w reached the new desired value.

Post processing:

11. The data acquired by the TSI® 3340 are elaborated in order to evaluate the aerosol size distribution and its cumulative distribution function (CDF), d_{32}, d^{5th} and d^{95th} and the total number concentration, considering the last 4 min of the measurement.

2.3.2 Experimental protocol for particle abatement in the systems GT-BC and GT-WES

Test preparation:

1. The thermostatic bath is switched on and adjusted in order to have the desired water temperature, T_w, in the growth tube.
2. The saturator is switched on and fixed at the temperature of 30°C.
3. The Palas dilutor is set to the temperature of 120°C in order to mix a pre-filtrated air with the incoming aerosol obtaining a volumetric dilution ratio of 10.
4. The particles suspension solution is prepared and put 20 min in an ultrasound bath at 80mHz in order to optimize the submicronic particles dispersion.
5. The blank tests A1, A2 and A3 are carried out.

Test execution:

6. The solution is fed to the aerosol generator and the pressure is set to the desired value in order to have a particle concentration suitable for the monitoring system
7. The valves are set to measure the aerosol inlet by means the SMPS TSI 3910 and each measure lasts 5 min.
8. The valves are set to send the aerosol to the growth tube.
9. The aerosol that exit the growth tube is sent to the SMPS TSI 3910 and each measure lasts 5 min;
10. The aerosol, which outcomes from the growth tube, is sent to the abetment unit.
11. The aerosol flow, which comes out from the abetment unit, is sent to the SMPS TSI 3910 and each measure lasts 5 min;
12. The temperature of the thermostatic bath is adjusted in order to obtain another water temperature in the growth tube and the test proceeds from the step seventh.

Post processing:

13. The data acquired by the TSI® Nanoscan 3910 are elaborated in order to evaluate the abatement efficiency of the growth tube and of the whole system, in terms of total number concentration and number concentration for each diameter, d_{32}, d^{5th} and d^{95th}.

2.4 Data Analysis

In this section the elaboration of the experimental data obtained by the diagnostic systems is reported.

2.4.1 Particles growth

The TSI 3340, used to examine the particles growth, provides the aerosol size distribution in the range 80-80 nm in terms of number particles concentration, per each channel, C_i. The instrument was set in order to divide the interval in 50 channels with a log distribution.

For each data test, the count mean diameter (CMD), the standard deviation (σ), the Sauter diameter (d_{32}), and the error (δ_x) of the particles number per each channel were calculated according to the equations (2.1-2.4):

$$CMD = \frac{1}{C_{tot}} \sum C_i d_i \tag{2.1}$$

$$\sigma = \frac{1}{C_{tot}} \sum C_i (d_i - CMD)^2 \tag{2.2}$$

$$d_{32} = \frac{\sum C_i {d_i}^3}{\sum C_i {d_i}^2} \tag{2.3}$$

$$\delta_{\ x} = \frac{\sigma_x}{\sqrt{N}} \tag{2.4}$$

where C_{tot} and d_i were the total number particles concentration and the mean value of the size channel of the distribution, while N was the number of samples.

Each distribution was normalised obtaining the probability density function *(PDF)* and then it was possible to estimate the cumulative distribution function (*CDF*) and the distribution mode. From the *CDF* was possible to evaluate the 5th and the 95th percentile diameters of the distribution.

A comparison of distribution of particles leaving the growth tube were made to show the evolution of particle growth with the increasing of temperature in terms of *CDF*, sauter diameter, mean diameter and the 5th and the 95th percentile diameters.

Although modelling of particle enlargement in the GT are not developed in this work, knowledge of the supersaturation profile is a valuable tool to interpret experimental findings. The variation of the water film temperature inside the GT led to different supersaturation profiles that govern the heterogeneous condensation. This profile can be derived following the modelling approach adopted by Tammaro et al. [55] on the basis of the analytical solution of the classical Greatz problem for heat and mass transfer. [116] In this study, we neglected the contribution to the supersaturation of the bottom flask, since experimental evidences showed that the aerosol leaving the flask did not present any appreciable change in term of particle size distribution and concentration as the water temperature increase. However, the temperature entering the cylindrical section of the GT was higher than that one at the inlet. This temperature was considered in the calculations. Knowing the supersaturation levels reached in the growth tube, a theoretical interpretation of the experimental findings was accomplished.

2.4.2 Particles abatement

The TSI 3910, used to examine the particles abatement, provides the aerosol size distribution in the range 11-400 nm in terms of number particles concentration, per each channel, C^j. The instrument divides the all range in 13 channels with a log distribution.

The total number removal efficiency, η_i^{tot}, of each unit and of the whole systems, GT-BC and GT- WES, were evaluated from the total number concentration at the inlet and outlet of each units ($C_{IN,\,i}^{tot}$;$C_{OUT,\,i}^{tot}$) according to the equation (2.5):

$$\eta_i^{tot} = \frac{C_{IN,i}^{tot} - C_{OUT,i}^{tot}}{C_{IN,i}^{tot}} \tag{2.5}$$

where *i* refers either to GT, BC, WES and GT-BC, GT-WES.

Beyond the total efficiency, it was possible to evaluate, for each unit, an efficiency for the jth particle size channel, η_i^j, with a particle number concentration of C^j, in #/cm^3 as:

$$\eta_i^j = \frac{C_{IN,i}^j - C_{OUT,i}^j}{C_{IN,i}^{tot}} \tag{2.6}$$

In order to better appreciate the contribution of the GT and either the BC or WES on the total removal efficiency and on the removal efficiency for each channel size, both the removal efficiencies were calculated as $-log(1-\eta_i)$. Where, for sake of simplicity, η_i stands for the total and per channel size efficiencies of each unit. Figure 2.24 (a) –(b) shows an example of the total removal efficiency and the removal efficiency per channel size as a function of the run tests and the channel size, respectively.

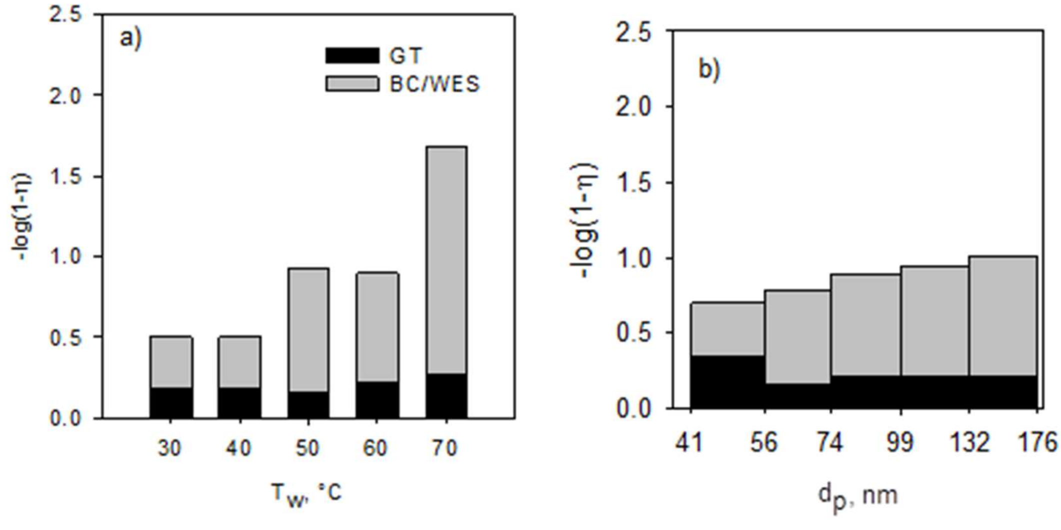

Figure 2-24- Example of the contribution of the GT and BC on the total removal efficiency as a function of the water film temperatures (a) and on the removal efficiency for each channel size as a function of channel size. (b)

The figure 2.24 plots the contribution of each unit on the removal efficiencies as stacked bars. The black bar represents the contribution of the GT while the gray one stands for the contribution of either the BC or the WES. The addition of the two stacked bars depicts the removal efficiency of the whole systems.

2.5 Quality assurance/quality control

To assure the accuracy, reliability and reproducibility of the collected data, each experimental measure was averaged over 10 samplings lasting 1 min each. Than all tests were performed in triplicate and the average values together with the standard deviation (σ) are reported. The TSI 3340 and the TSI 3910 have both a typical particle size accuracy within 5%. The dilutor system has an error of roughly 5% on the dilution ratio. The aerosol generator has a repeatability standard deviation lower than 3%. Besides, the experimental data replicates in terms of particle number concentration showed an error of about 25% with the TSI 3910 and about 20% for the TSI 3340.

3 RESULTS AND DISCUSSION

3.1 Particle growth

3.1.1 Experimental results

In this section, the experimental results and discussion on the particle growth are reported. The results of the preliminary test, aimed to verify the existence of an upper limit of particle diameter above which all the particles were collected by the GT and the pipelines, were reported. For sake of simplicity, only the results obtained with the polystyrene nanoparticles with the volumetric diameter of 400 nm are reported.

Figure 3.1 shows the ASD of the tested nanoparticles at the inlet and exit of the GT operating at the water film temperature of 25,35 and 45°C.

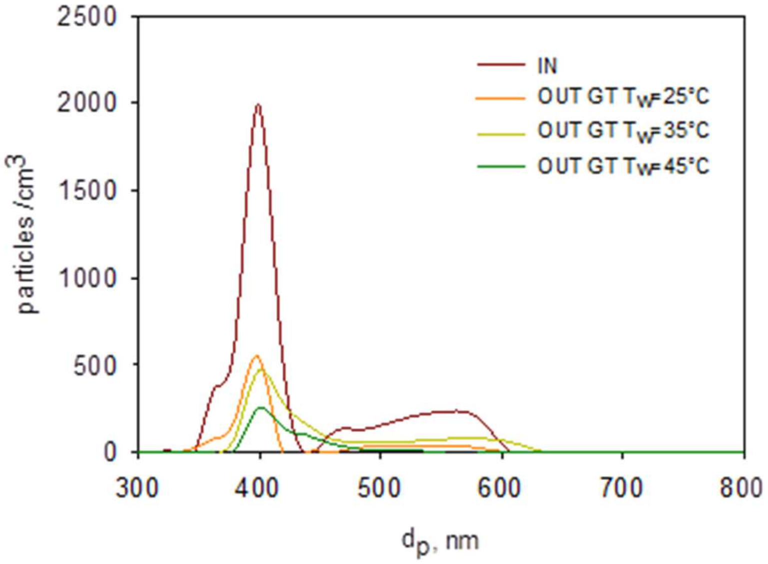

Figure 3-1- Aerosol size distribution of polystyrene calibrated nanoparticles with nominal diameter of 400nm at the inlet and outlet of the GT with a water film temperature of 25,35 and 45°C.

Figure 3-1 shows the results of a preliminary tests aimed to investigate the range of particles that are collected by the GT and the pipelines. The experimental results showed that the aerosol size distribution at the inlet had a peak at 400 nm and a tail ranging from 450 to 600 nm. At the exit of the GT the concentration of the particles decreased with the temperature and apparently, no particle growth was observed. This results suggested that the nanoparticles, indeed, grew and they were not revealed by the TSI LAS 3340 because the GT and the pipelines had a kind of “cut-off” for the particles larger than 500 nm, therefore all the particles that grew above this size were not measured.

In the light of these results, the aerosol size distribution of the tested aerosol at the exit of the GT had a particle size ranging roughly from 80 to 500 nm. Therefore, only the particles that enlarged towards size below 500 nm were detected and a concentration decrement was due to the loss of particles with size above the upper limit. This operative condition led to a generation of a narrow aerosol size distribution at the exit of the GT, whatever the materials, because all the grown detectable particles ranged from 200 to 400 nm.

The aerosol size distributions at the inlet and at the outlet of the growth tube operated a different water film temperature, T_w, are presented in terms of probability density function (PDF), cumulative distribution function (CDF), count mean diameter (CMD), mode, Sauter diameter (d_{32}) and 5th and 95th percentile.

Sodium Chloride aerosol

Figure 3.2 shows the PDF (left) and CDF (right) of the sodium chloride aerosol at the inlet and GT outlet as a function of the water film temperature, T_w. Table 3.2 reports the mode, CMD, the standard deviation σ, d_{32}, d^{5th} and d^{95th} percentile of the aerosol size distribution at the inlet and outlet of the GT at different T_w.

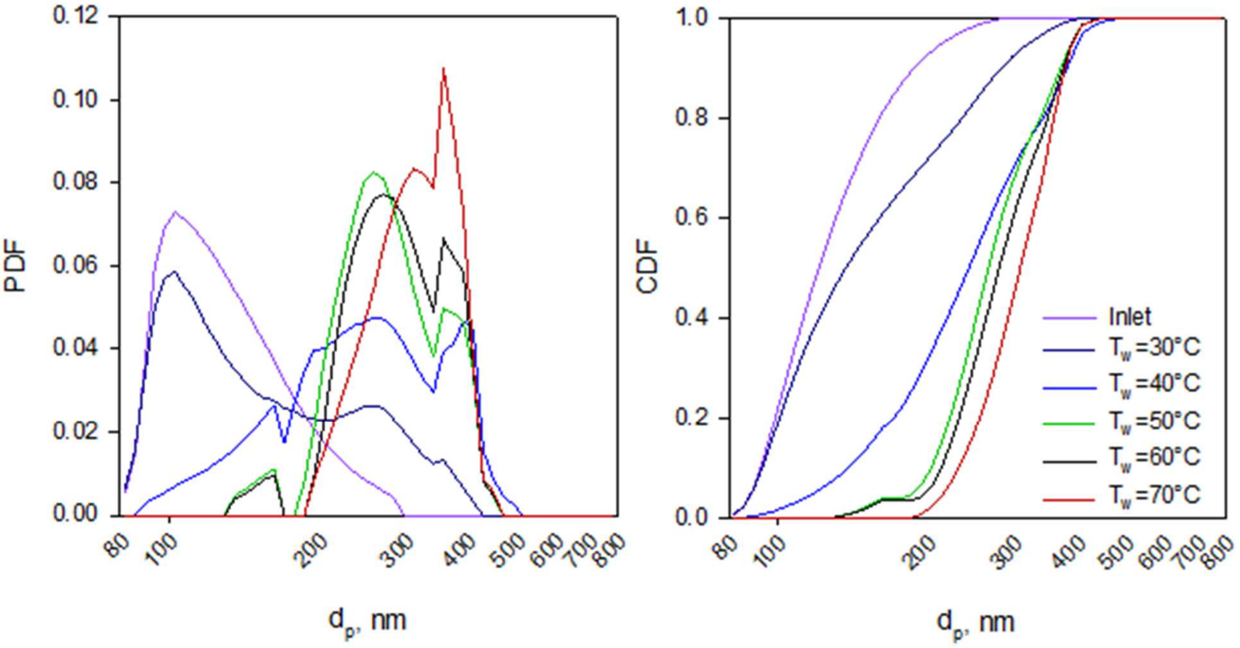

Figure 3-2 The sodium chloride aerosol size distribution as function of the particle diameter parametric with the temperature of the water film temperature: PDF (right) and CDF (left).

Table 3-1 Mode, CMD, standard deviation σ, d_{32}, d^{5th} and d^{95th} diameters of the sodium chloride aerosol size distribution at the inlet and at the outlet of the GT, as function of the water film liquid temperature, T_w.

T_w, °C	mode	CMD, nm	σ, nm	d_{32}, nm	d^{5th}, nm	d^{95th}, nm	C_{tot}, #/cm^3
INLET	103	135	52	161	90	215	15226
30°C	103	170	82	241	86	325	11336
40°C	259	258	90	317	120	400	24067
50°C	259	282	65	312	190	392	28498
60°C	271	294	64	320	196	391	30315
70°C	357	315	56	334	215	392	25253

The experimental results showed that the ASD at 30 °C presented particles larger than 300 nm, absent in the ASD at the inlet of the GT. It is possible to ascribe the presence of these particles to the condensational growth, that already at 30°C. Remembering that the aerosol enters the GT at 25°C, this results means that as soon as a gradient temperature, although minimum, was established the condensational growth occurred. Once the heterogeneous condensation took place, the ASD enlarged with the temperature and the particles ranging from 300 to 400 nm appeared and their number concentrations increased too. Indeed, the peaks of the distribution shifted from 100 nm at 30°C to 400 nm at 70°C. First a major peak at roughly 280 nm, as showed in the tab 3.1, appeared and then slightly shifted at 357 nm by increasing T_w. The occurring of the heterogeneous condensation at 30°C is confirmed by the CDFs (Figure 3.1 right diagram) that showed a marked shift towards larger particles at this temperature. As the temperature increased, the CMD, mode and d_{32} increased from 135 to 315 nm, 103 to 357 nm, 161 to 334 nm, respectively. The condensational growth occurring was confirmed by the increment of the d^{95th} that passed from 212 to 325. Due to the loss of particles above 500 nm, the aerosol size distribution at the exit of the GT tends to a narrow distribution: all the detected particles ranged from 200 to 450 nm, the largest were loss and the smallest grew in this range. As reported in Table 3.1, the total number concentration had a non-monotonic trend with the temperature. A completely understanding of this trend hides several processes that, at the moment, it was difficult to differentiate. Generally, the initial number concentration decreased at 30°C because in the GT some particle loss was inevitable. With the increased of the temperature and so of the grew particles, the number concentration increased due to the enlargement of particles not initially detected. At 70°C the concentration started to decrease due to the loss of the particles larger than 500 nm.

OptiBind 0.1 aerosol

Figure 3.2 shows the PDF (right) and CDF (left) of the OptiBind 0.1 aerosol at the inlet and outlet of GT as a function of the water film temperature, T_w. The table 3.2 reports the mode, CMD, the standard deviation σ, d_{32}, d^{5th} and d^{95th} percentile of the aerosol size distribution at the inlet and outlet of the GT at different T_w.

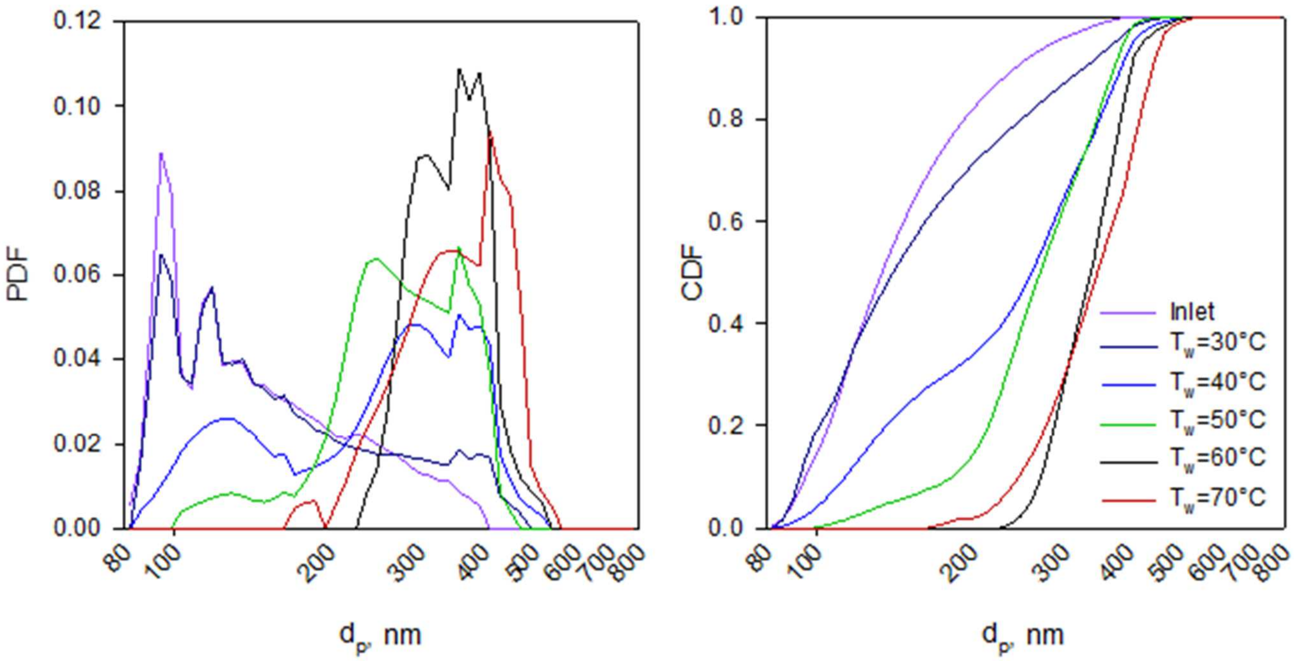

Figure 3-3 The OptiBind 0.1 aerosol size distribution as function of the particle diameter parametric with the temperature of the water film temperature: PDF (left) and CDF (right)

Table 3-2-Mode, CMD, standard deviation σ, d_{32}, d^{5th} and d^{95th} diameters of the OptiBind 0.1 aerosol size distribution at the inlet and at the outlet of the GT, as function of the water film liquid temperature, T_w.

T_w, °C	Mode	CMD, nm	σ, nm	d_{32}, nm	d^{5th}, nm	d^{95th}, nm	C_{tot}, #/cm^3
INLET	113	156	72	212	90	297	21204
30°C	94	179	92	278	90	380	18694
40°C	357	258	107	331	105	410	16057
50°C	357	280	80	318	105	391	12963
60°C	357	346	55	364	258	429	14045
70°C	357	310	128	337	149	450	5607

The PDFs in the left diagram of Figure 3.2 describe the ASDs of OptiBind 0.1 at the inlet and at the outlet of GT, parametric with the water film temperature. The Fig 3.2 shows clearly that for this material the enlargement due to heterogeneous condensation started at 40°C. At 30°C the ASD was similar to the inlet one, suggesting that no particles agglomeration occurred and therefore the particle growth at higher temperature was ascribable only to the condensational growth. With the temperature increase, the peak at 100 nm shifted to 357 nm at 40°C and then it unchanged as it can be noted from Table 3.2. The ASDs evolution was gradual with the temperature: at 30 and 40 °C it was clear that a distribution transition occurred because the peak at 100 nm slightly disappeared and a peak at 400 nm slowly appeared. The CDFs of Figure 3.2 (right) confirmed that the heterogenous condensation occurred at T_w= 40°C, at which was observed a substantial shift of the aerosol towards larger particles. As listed in Table 3.2, from 30 to 70°C, the CMD and the d_{32} increased monotonically passing from 156 and 212 nm to 310 and 337, respectively. As the temperature of liquid film gradually increased, the particles distribution became more and more narrow and this can be observed from the d^{5th} and d^{95th} trends. This behavior was due to the loss of the particles larger than 500 nm as it is possible noting by the decrement of the number particles concentration.

OptiBind 0.2 aerosol

The Figure 3.3 shows the PDF (right) and CDF (left) of the OtiBind 0.2 aerosol at the inlet and GT outlet as a function of the water film temperature, T_w. The table 3.3 reports the mode, CMD, the standard deviation σ, $d_{32,}$ d^{5th} and d^{95th} percentile of the aerosol size distribution at the inlet and outlet of the GT at different $T_{w.}$

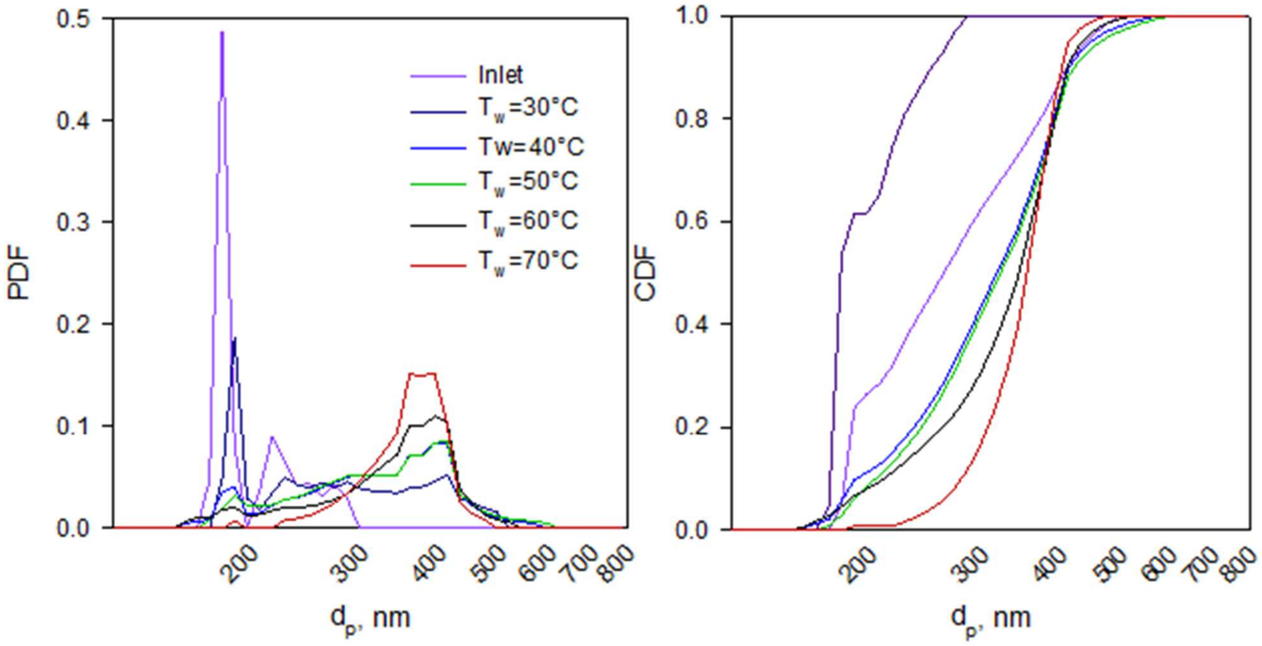

Figure 3-4 The OptiBind 0.2 aerosol size distribution as function of the particle diameter parametric with the temperature of the water film temperature: PDF (left) and CDF (right)

Table 3-3 Mode, CMD, standard deviation σ, d_{32}, d^{5th} and d^{95th} diameters of the OptiBind 0.2 aerosol size distribution at the inlet and at the outlet of the GT, as function of the water film liquid temperature, T_w.

Tw, °C	mode	CMD, nm	σ, nm	d_{32}, nm	d^{5th}, nm	d^{95th}, nm	C_{tot}, #/cm^3
INLET	179	201	31	212	170	260	22266
30°C	187	285	90	340	179	430	20485
40°C	391	321	92	365	179	450	12428
50°C	410	327	128	372	185	471	9422
60°C	391	335	180	367	180	435	12070
70°C	391	353	53	366	258	410	8616

The PDFs in the left diagram of Figure 3.3 describe the ASDs of OptiBind 0.2 at the inlet and at the outlet of GT, parametric with temperature T_w. The plot shows that the heterogenous condensation took place at 30°C as showed in Figure 3.3 (left) by the ASDs shift towards larger particles. Indeed, the evaluated parameters listed in Table 3.3 had the major variation passing from the inlet to 30°C. The peaks of the distribution shifted from 200 nm at 30°C to 400 nm as soon as $T_w \geq$ 40°C. As soon as the condensational growth took place, the ASD sfhifted towards larger particles as showed in the Figure 3.5 (right). At 70°C the initial peak at 200 nm completely disappeared and so all the particles were enlarged towards a size ranging from 260 to410 nm. The CMD of OptiBind 0.2 aerosol increased from 200 nm up to roughly 350 nm at the inlet and 70 °C, respectively. The maximum variation of the CMD and of the d^{95th} was observed between the inlet ASD and that one at the outlet of the GT operating at T_w= 30°C. By looking at variation of the mode of the ASDs with the temperature, reported in the table 3-3, it passed from 179 to 391 at 30 and 70°C respectively. The d^{5th} and d^{95th} percentile diameter showed that at 70°C all the grown detected particles enlarged to a similar size. The total number particle concentration, as for the sodium chloride aerosol, had a non-monotonic trend with the temperature and similar observations were envisaged. dropped off with the temperature: particles larger than the upper limit were captured by the GT and the pipelines.

Titanium dioxide aerosol

The Figure 3.4 shows the PDF and CDF of the titanium dioxide aerosol as function of the particle diameter parametric in the temperature, T_w, at inlet and outlet of GT. The table 3.4 reports the mode, CMD, the standard deviation σ, $d_{32,}$ d^{5th} and d^{95th} percentile of the aerosol size distribution at the inlet and outlet of the GT at different $T_{w.}$

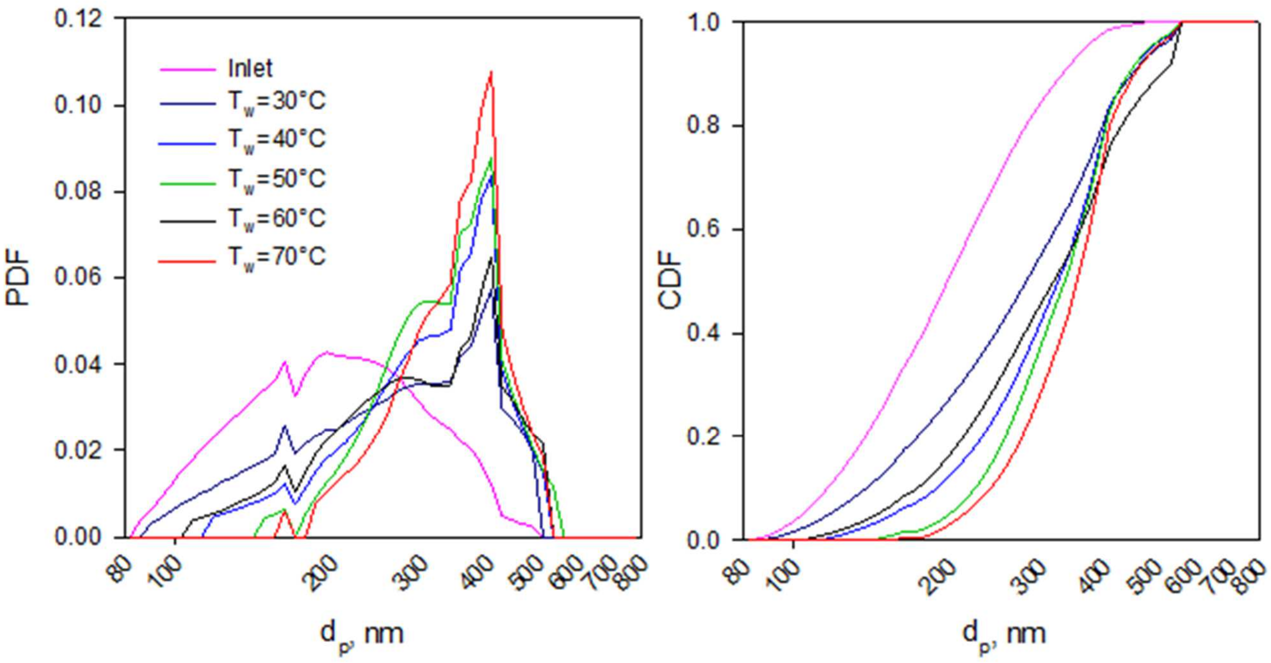

Figure 3-5 The titanium dioxide size distribution as function of the particle diameter parametric with the temperature of the water film temperature: PDF (left) and CDF (right)

Table 3-4 Mode, CMD, standard deviation σ, d_{32}, d^{5th} and d^{95th} diameters of the titanium dioxide aerosol size distribution at the inlet and at the outlet of the GT, as function of the water film liquid temperature, T_w.

T_w, °C	Mode	CMD, nm	σ, nm	d_{32}, nm	d^{5th}, nm	d^{95th}, nm	C_{tot}, #/cm^3
INLET	196	217	83	280	105	375	23754
30°C	410	299	125	397	115	516	15198
40°C	410	330	102	390	156	493	18050
50°C	410	344	89	389	200	493	19044
60°C	410	339	131	437	145	566	17912
70°C	410	360	86	401	215	516	17758

The ASD of the titanium dioxide at the inlet had a wide distribution ranging from 100 to 375 nm. The experimental data showed that as soon as the aerosol encountered the water film, a particle growth occurred, besides the low temperature gradient between the aerosol (T_g=25°C) and the water film (T_W=30°C). The wide distribution slowly was replaced by a narrower distribution. The mode of the ASD at the exit of the GT at 30°C was 410 nm, higher than that one at the inlet of the GT. The CMD and the d32 increased monotonically with the temperature passing from 217 to 360 and from 280 to 401, respectively. The generation of a narrow distribution was confirmed by the d^5 and d^{95} percentile diameters, that at 70°C were 215 and 516 respectively. As reported in the table 3.4, the total number concentration at the exit of the GT was lower than the inlet one and it increased up to 50°C and then dropped off at 60 and 70°C. This trend suggests that the GT and the pipeline contributed to capture the particles even when the heterogeneous condensation was absent. Moreover, the number concentration firstly increased with the temperature due to the measure of the enlarged particles not initially detectable and then decreased due to the loss of the largest particles. The transformation of the ASD observed at already 30°C was certainly ascribable to the condensation growth since the blank tests carried out without water in the GT revealed that the ASD at the GT outlet was like that one at the inlet, excluding any particle agglomeration.

Carbon black aerosol

The Figure 3.5 shows the PDF and CDF of the carbon black aerosol as function of the particle diameter parametric in the temperature, T_W at the inlet and outlet of the GT. The table 4.5 reports the mode, CMD, the standard deviation σ, $d_{32,}$ d^{5th} and d^{95th} percentile of the aerosol size distribution at the inlet and outlet of the GT at different $T_{W.}$

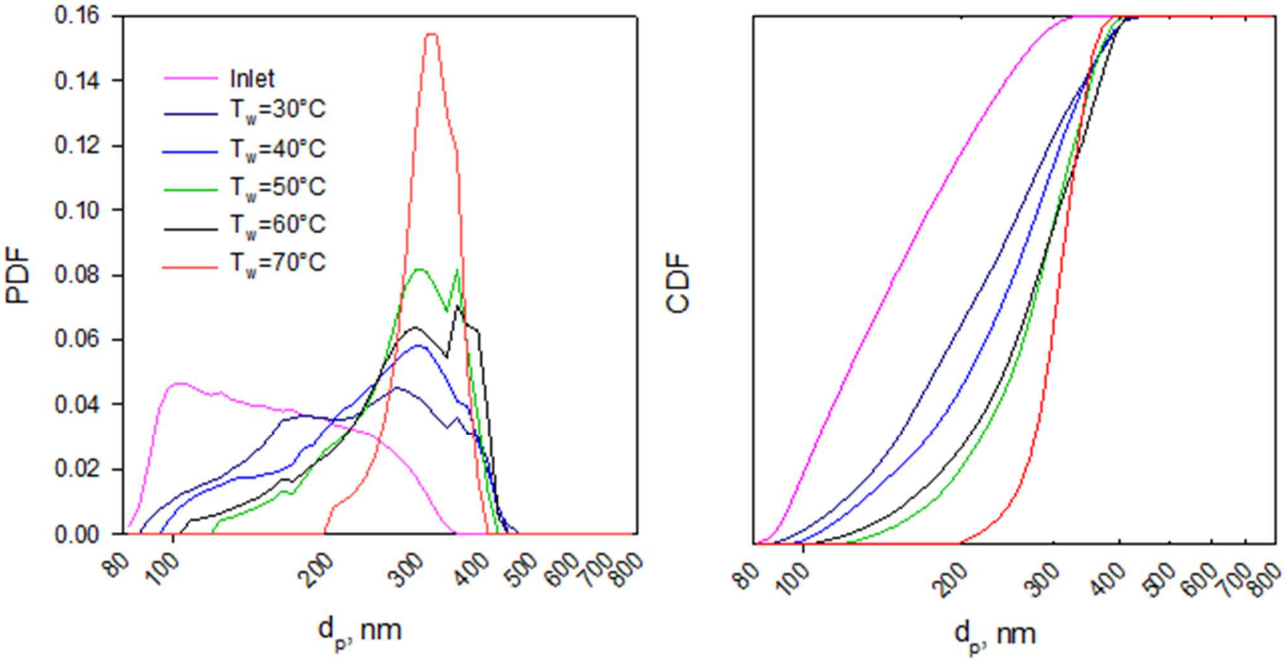

Figure 3-6 The carbon black size distribution as function of the particle diameter parametric with the temperature of the water film temperature: PDF (left) and CDF (right)

Table 3-5 Mode, CMD, standard deviation σ, d_{32}, d^{5th} and d^{95th} diameters of the carbon black aerosol size distribution at the inlet and at the outlet of the GT, as function of the water film liquid temperature, T_w.

T_w, °C	mode	CMD, nm	σ, nm	d_{32}, nm	d^{5th}, nm	d^{95th}, nm	C_{tot}, #/cm^3
INLET	103	166	60	210	90	280	1878
30°C	271	236	85	294	110	380	6601
40°C	297	255	82	301	118	380	14023
50°C	297	283	66	312	160	374	14342
60°C	357	283	77	320	142	390	12369
70°C	311	313	38	322	236	370	9538

The PDF, Figure 3.5 (left), illustrates a similar trend observed for the other tested aerosols. The carbon back aerosol started to grow at already 30°C, although its hydrophobic nature. This trend was confirmed by the CDF that had a marked shift to larger particles at 30°C. The PDF shape changed with the temperature from a wide distribution to a narrow distribution with a marked peak at 400 nm for water film temperature above 50°C. The increment of the mode, the CMD and the d_{32} confirmed the activation of the heterogeneous condensation at the minimum temperature gradient.

The narrow shape, confirmed by the trend of d^{5th} and d^{95th}, suggested that, once the conditions to trigger the nucleation were achieved, the particles started to growth tending to the same size independently from the initial one. The particle number concentration increased by passing in the GT for all the temperatures compared with the inlet. This behaviour was ascribable to the growth of particles not initially detectable. Indeed, as showed in the Figure (2-20), the ASD of the carbo black at the inlet had a bimodal distribution with a significant peak at 30 nm and a lower one at roughly 100 nm. The TSI 3340 at the inlet could detect only the second peak, therefore the smallest particles once reached the size above 80 nm due to the condensation of vapor, become detectable. The transformation of the ASD observed at already 30°C was certainly ascribable to the condensation growth since the blank tests carried out without water in the GT revealed that the ASD at the GT outlet was like that one at the inlet, excluding any particle agglomeration.

3.1.2 Condensational growth discussion

The condensational growth, or heterogeneous condensation, has been studied for the last decades and several theories were developed to describe the process under operating conditions typical of atmospheric conditions and of industrial plant effluents of wet scrubbers. The condensational growth consists in the enlargement of a particles due to the condensation of the vapor on the particles surface. The classical theory divides the process in two main steps: nucleation and growth. The first describes the generation of a liquid embryo on the foreign surface and the second its consequential growth. The critical point of this process lies in the formation of the first liquid cluster.

It's known that the particle surface plays a relevant role in the formation of a liquid cluster on it. Indeed, the affinity of the surface for water, in terms of both hydrophobicity or hydrophilicity toward liquid water or in terms of adsorption of water vapour determine the actual capacity of a particle to condensate water once exposed to a supersaturated environment. The most relevant distinction among model for the description of the condensational growth are related to the shape of the water deposited over the surface, as proposed by Fletcher. This was described either as a liquid embryo, or as a liquid layer surrounding the particles.

Fletcher [24] proposed the condensational growth of water vapor on a homogeneous spherical particle and modified opportunely the free energy of formation of a critical embryo by considering a geometric factor. Starting from the Fletcher model (Eqs. 1.3-5) and imposing a reference growth rate of one embryo per second, it is possible to estimate the size of the liquid embryo, D_g, that exposed to a supersaturation S grows with a velocity of 1 embryo per second on a particle surface with diameter d_p. This maximum size has to be compared with the size of the smallest embryo that is thermodynamically stable, as described by the Kelvin equation. If this is smaller than D_g, the embryo will growth, otherwise it will evaporate. In the Fletcher's theory, the role of the particle nature is represented by the contact angle, θ: for hydrophilic material θ→0° and for hydrophobic material θ→180°. For θ=0° the particle is completely wetted by the water and acts as a water droplet; for θ =180, the water embryo is a spherical drop virtually touching the particle surface on a single point.

In the first case, the condensation may take place as the homogeneous condensation of water over a liquid droplet, which is well described by the Fuchs's model [117]. This model also indicates the conditions under which a water droplet exposed to a certain water partial pressure can either evaporate or condensate: indeed, due to the curvature effect on the vapour pressure over a spherical particle, the actual saturation pressure over the particle surface is higher than that occurring on a flat surface or in the bulk of the gas phase. This means that, in spite of the temperature difference among the gas and the liquid surface, a drop can evaporate or condensate according to its size: there is a critical size above which condensation can take place.

The equations (3.1-4) determines the temperature of a droplet, T_d, with D_g as diameter immersed in a gas with a temperature T by the following equations:

$$T_d = T_g - \frac{I_c L}{2\pi\lambda D_g} \tag{3.1}$$

$$I_C = \frac{2\pi d_g M_w D}{R}\left[\frac{p_s}{T_d} - \frac{p_g}{T_g}\right] \tag{3.2}$$

$$p_s = p^0(T_d)\exp\left[\frac{4\sigma}{\rho_l}\frac{M_w}{RT_d D_g}\right] \tag{3.3}$$

$$p_g = p^0(T)\mathrm{S} \tag{3.4}$$

Where L is the latent heat, λ is the thermal conductivity of the gas, the p_s and p_g are the vapor pressure on the droplet surface and in the gas, respectivley; I_c is the mass flux.

The latent heat of condensation released must be transported away since the temperature of the droplet, and accordingly the vapor pressure at the droplet surface, would increase continuously causing condensational droplet growth to stop. The temperature of the droplet, in the condensation conditions, must be greater than temperature of the surrounding atmosphere so that the heat released can be carried off. Therefore, from the system of equations, it was evaluated in which conditions a droplet can growth by varying the operative conditions of T_g, S and D_g.

The debate on the nucleation theory is still open and different viewpoints are present in literature. Several authors, as Chen et al. [37] Van der Hage [36] pointed out that the Fletcher theory overestimates the supersaturation levels required to trigger the condensational growth. Indeed, Chen et al. [37] showed that the supersaturation required to enlarge submicrometric particles was lower than 36% compared with that one predicted by the Fletcher model. They concluded that the condensational growth process was preceded by the adsorption of at least a monolayer of water molecules on the particle surface, which decreased significantly the energetic barrier of the condensation process, so that the contact angle will become close to zero. Van der Hage [36] envisaged that in the condensational growth it is inescapable consider the adsorption effects but he did not come out with a definite equation to model his intuition.

In our study, we considered five different materials: sodium chloride as representative of soluble particles, the titanium dioxide as hydrophilic particles, polystyrene calibrated nanoparticles with two different mean volumetric diameters (100 and 200 nm) and carbon black as hydrophobic materials. The last particles are considered as highly hydrophobic but they exploit a moderate water adsorption capacity [118], making them interesting for a condensational growth study.

The experimental results on the condensational growth of these materials in the growth tube can be interpreted according the models of Fletcher and Fuchs. To this aim, the first step was to evaluate the supersaturation profile inside the GT, as proposed by Tammaro et al. [55]

for the different water film temperature, T_w. In this study, we neglected the contribution to the supersaturation of the bottom flask, since experimental evidences showed that the aerosol leaving the flask did not present any appreciable change in term of particle size distribution and concentration as the water temperature increase. However, the temperature entering the cylindrical section of the GT was higher than that one at the inlet. This temperature was considered in the calculations.

The Figure 3.7 shows the supersaturation profile inside the growth tube evaluated by the theoretical model of the tests N°1-5 that corresponded to the water film temperature of 30,40,50,60,70 °C, respectively.

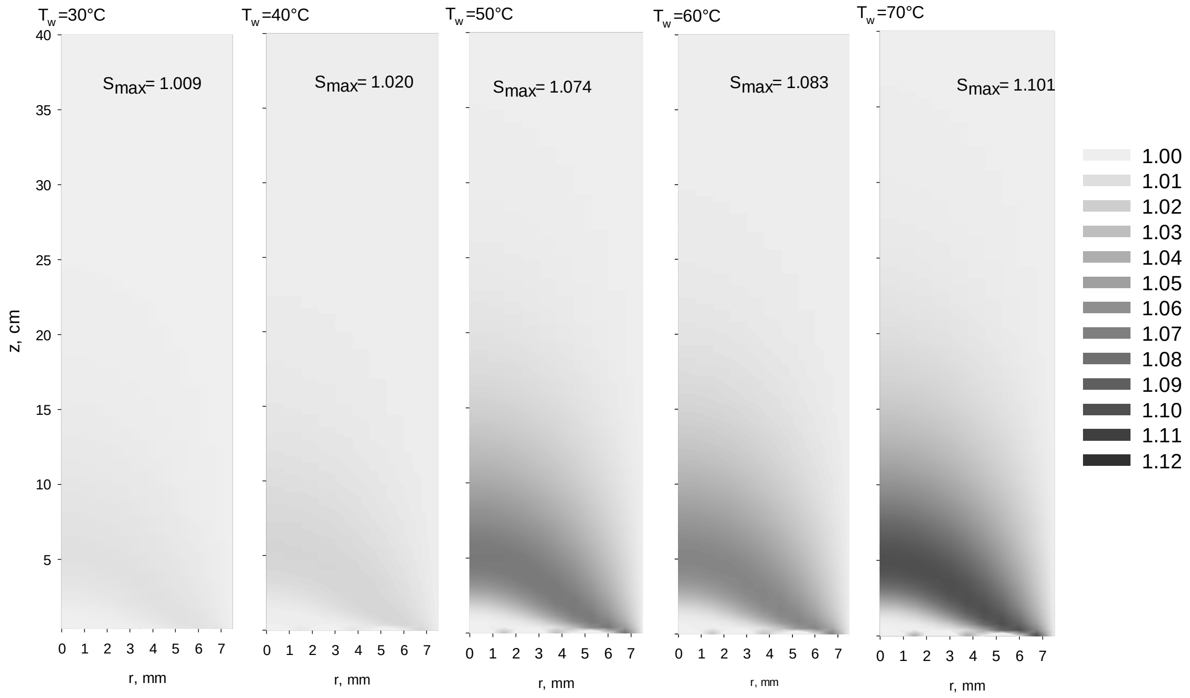

Figure 3-7 Supersaturation profiles in the half plane of the GT for the experimental tests.

Figure 3.7 shows that the supersaturation level varied with the temperature passing from a maximum of 1.009 at 30°C to 1.101 at 70°C. The maximum value was reached in the centreline of the GT for all the operating conditions and after the first 20 cm equilibrium conditions were achieved. The supersaturation zone was concentrated within the first 15 cm of the growth unit and spread with the temperature. From these profiles, it was possible to evaluate the distribution of the supersaturation levels and then the residence time distribution of the particles that are exposed to a specific level of supersaturation in the growth tube.

The supersaturation conditions inside the growth tube can be compared with the prediction of the Fletcher and the Fuchs models, in order to assess the critical embryo size for a reference condition (J=1 embryo/s) and the critical size of stable condensing embryos, respectively. The Fletcher model was evaluated by imposing a contact angle θ=0° and the specific value of the contact angle retrieved from the pertinent literature:

However, we noticed that in this last case, the supersaturation levels estimated by the Fletcher model were too high and out of scale compared with the actual supersaturation profiles reached in the growth tube. Indeed, this observation suggest that the Fletcher model overestimate the critical conditions and indicate the probable presence of a water layer surrounding the particles, as suggested by Chen et al. [37]. Similarly, our research group showed that soot particles formed by ethylene flame condensate effectively for a growth tube operated with a water temperature of 309 K and a gas temperature of

293 K [55] .To describe the data, a contact angle of 18°, which are very different from the presumed value close to 180° assumed for hydrophobic materials, as soot is supposed to be.

Furthermore, the water embryo size as a function of the supersaturation levels was evaluated by keeping constant the particle diameter equal to 280 nm. It was chosen this specific value because represents the smallest value of the d^{95th} of the aerosol size distribution of the tested materials.

The analysis of experimental data can be conducted by plotting the distribution of the resident time as a function of the supersaturation profiles and comparing them with the theoretical curves obtained by the two considered models for each water film temperature. For sake of clarity, the experimental data were plotted in two different figure 3.8 (a) for T_W= 30 and 40°C and figure 3.8- (b) for T_W=50, 60 and 70°C.

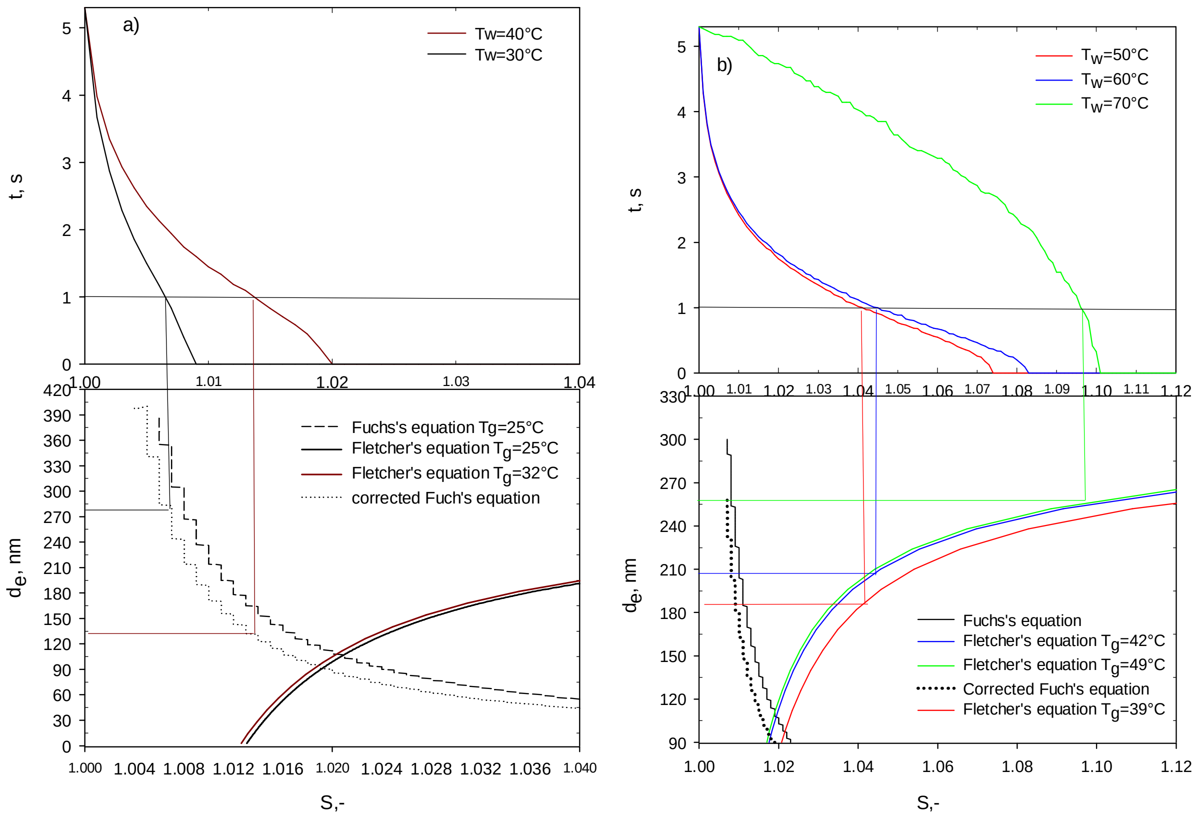

Figure 3-8-The exposed time of the particles as a function of the supersaturation levels (top). The particle diameter as a function of the supersaturation levels evaluated according the Fuchs's model, normal and corrected, and the Fletcher's one with d_p =280 nm and m=1.

The residence time distribution as a function of the supersaturation level showed that the aerosol was exposed for at least 1 second to values of S higher than 1.006, 1.014, 1.04, 1.045 and 1.095 at 30, 40, 50, 60 and 70°C respectively. By applying the Fuchs's model to our experimental conditions at 30°C and 40°C we noticed that the critical droplet size as a function of the supersaturation level was almost constant and so, for the sake of simplicity, we only plotted the curve at 30°C in Figure 3.8(a). Similar results were obtained from 50 to 70°C and only the curve obtained at 60°C was plotted in Figure 3.8(b). The curves of the water embryo evaluated by the Fletcher model for $\theta=0°$ as function of the supersaturation levels were evaluated for each temperature. The intersection of the Fletcher's and Fuchs's curves provides the minimum water embryo size that is thermodynamically stable and that can grow by exposure of 1 s to the corresponding value of S on the abscissa. According to Fletcher's equation the smallest embryo that is generated at 30 and 40°C on a particle with d_p=280 nm and it is stable to grow has a size of 100 nm roughly and needs a supersaturation level of 1.02 to survive. This is however, inconsistent with the actual supersaturation level inside the growth tube.

In fact, the experimental data showed that already at 30°C all the tested aerosol growth, it means that 100 nm grew in the GT as soon as the supersaturation level was above 1.005, grew. According to Fletcher's curve, at this supersaturation level it is impossible to generate any water embryo of any size, therefore it is possible to envisage that the particles was completely covered by a film liquid that made it to act as a droplet. However, according to Fuch's equation, at a supersaturation level of 1.006 only droplets above 360 nm can enlarge for vapor condensation, but still this theoretical result is in discrepancy with the experimental evidences since no particles larger of 280 nm entered the GT.

Indeed, we believe that the reason for this discrepancy lies in the consideration that Fuchs and Fletcher models include energy terms related only to the physical condensation of water on the particle surface. This however neglects the adsorption energy, which plays a critical role in forming a liquid layer around the particles. The pertinent literature, currently provide information only for the adsorption of water on different kinds of carbon black. These studies indicated that even below saturation conditions at 25°C, for S=0.9-0.95, carbon blacks may exploit multilayer adsorption with a number of surface layer from 5 to 50 according to the specific material properties [119]. This adsorbed water is strongly bonded to the surface, thanks to the adsorption energy and its stability is higher than that considered by Fuchs and Fletcher. A special mention should be given to sodium chloride. This is a soluble material in water, so its condensational growth involves different steps compared with the insoluble materials as Lee et al. (Li et al.) pointed out. At this moment, the interpretation of condensational growth of this particular material is still at an early stage and its study is keep continuing.

As an additional confirmation of the presumed role of adsorption phenomena on the stability of water embryos during the nucleation phase, we can cite the number of studies reported in the pertinent literature and pertaining to the properties of interfacial water. A synthetic review on these properties is reported in the text of Pollack [120], which described several experimental evidence on how the water at the interface of several materials, included polymers, have a different mesoscale structure which is more stable, more viscous, more elastic and has a higher surface tension. These properties are, of course, an effect of adsorption phenomena over the surface. If these properties are included in the same Fletcher or Fuchs models, we can similar observe a shift of the two models towards smaller stable embryos and condensing droplets.

In light of these considerations, it appears that the critical point of the condensation models lies in the assumption that the embryo stability is only related to the minimization of the free Gibbs's energy between the liquid and vapour water phases. These models do not take into account any contribution of the particle surface associated to the energy of adsorption, and the way it changes moving along the subsequent water layers, and the modification of the interfacial water properties.

At the moment, to provide a first descriptive model for our experimental data, we considered a correction factor in the Eq.(3.5) representing the critical diameter calculated according the Kelvin's equation, that is hidden in the Fuchs's and the Fletcher models for the definition of p_s.

$$ln(S) = \beta \frac{4\sigma M}{\rho R_v T D_g} \qquad (3.5)$$

The curve obtained with β=0.8 was plotted in the Figure 3.8, which shows that indeed a particle with a dimeter of 280 nm covered by a layer of water can growth exposed to a supersaturation level of 1.006. Again, we remember that we are assumed that all particles are covered by a uniform layer of water, as suggested by experimental evidences.

Indeed, the factor β=0.8 was tuned to consider the condensation of particles of size 280 nm although this value should be different if smaller diameters are considered.

For the water temperature of 40°C according the Fletcher's equation, still any embryo was stable to growth exposed at the supersaturation level of 1.014. According to Fuchs's all the particles covered by a liquid layer and larger than 160 nm were able to growth for vapor condensation. For the water temperatures above 50°C the Fletcher's model started to identify possible embryo that are thermodynamically stable and have the conditions to grow with a rate of one embryo per second. Indeed, embryo of size 180, 200 and 260 were generated on the particle surface and can growth. Therefore, under these conditions, the condensational growth can occur through either the growth of particles smaller than 90 nm, covered by liquid layer, or the generation of stable liquid embryos. It worth to underline that these embryos were evaluated on a particle with a diameter of 280 nm, but as the supersaturation increase, smaller particles can house stable embryo that are able to grow.

In order to explain the implementation of the correction factor a thermodynamic study was accomplished.

The thermodynamic of the homogeneous and heterogeneous condensation

The free energy of a liquid embryo generated on a foreign surface leads to different scenarios that is possible to describe as following:

1. Heterogeneous condensation on an insoluble, homogeneous, spherical particle with high wettability (contact angle, ϑ, =0);
2. Heterogeneous condensation on an insoluble, heterogeneous surface where the interface solid liquid keeps constant with the embryo growth (ϑ=ϑ(r_e));
3. Heterogeneous condensation on an insoluble, heterogeneous surface where the interface solid liquid changes with the embryo growth (ϑ=constant);
4. Heterogeneous condensation on a soluble, homogeneous, spherical substance;

It can be assumed that the studied materials in this work fall within the first class.

The variation of the free energy of a liquid shell surrounding a spherical, homogeneous and insoluble particle is as following [23,24] :

$$\begin{aligned} \mathrm{d}G_{het} &= \mu_l dn_l + \sigma dS_{lg} + \mu_v dn_g + \left(\sigma_{ls} - \sigma_{gs}\right) dS_{gs} \qquad (3.6) \\ &= (\mu_l - \mu_v) dn_l + \sigma dS_{lg} + \left(\sigma_{ls} - \sigma_{gs}\right) dS_{gs} \end{aligned}$$

Where S_{gs} is the contact surface between the solid and the liquid; σ_{ls} *and* σ_{gs} are the surface free energy between the liquid and the solid, and the solid and the gas, respectively.

The terms in the Eq. (3.6) can be expressed as a function of the embryo radius:

$$dn_l = \frac{\rho}{M} dV = \frac{\rho}{M} d \frac{4}{3} \pi \left({r_e}^3 - {r_p}^3\right) = \frac{\rho}{M} 4\pi (r_e)^2 \, dr_e \qquad (3.7)$$

$$dS_{lg} = d4\pi (r_e)^2 = d4\pi (r_e)^2 = 8\pi (r_e) dr_e \qquad (3.8)$$

$$dS_{gs} = 0 \qquad (3.9)$$

$$\mathrm{d}G_{het} = (\mu_l - \mu_v) \frac{\rho}{M} 4\pi (r_e)^2 \, dr_e + \sigma 8\pi (r_e) dr_e \qquad (3.10)$$

$$\frac{\mathrm{d}G_{het}}{dr_e} = (\mu_l - \mu_v) \frac{\rho}{M} 4\pi (r_e)^2 + \sigma 8\pi (r_e) = 0 \qquad (3.11)$$

$$r_e{}^* = -\frac{2\sigma M}{\rho(\mu_l - \mu_v)} \tag{3.12}$$

When (μ_l- μ_v) is considered as the chemical potential difference between the liquid and the vapour phase. The critical embryo assumes the same equation of the Kelvin equation (Eq. (1.2)) where μ_l is assumed as a pure liquid. This model neglects the physical-chemical interactions between the solid and the condensate phase. Since it was assumed that the contact angle solid-liquid was equal to 0, it means that the particle acts as a liquid droplet of the same radius and so its growth rate can be described according the Fuchs' model [117] and from the Fletcher model with ϑ=0. [24]

In order to take into account the physical-chemical interactions between the solid and the condensate phase the potential of the liquid phase has to be defined as the potential of an adsorbed phase, expressed as:

$$\mu_l = \mu_v{}^0 + R_v T ln p^{eq} \tag{3.13}$$

The equilibrium pressure p^{eq}, conceptually similar to the vapor pressure is given by Piasecki and W. Rudziński as the invers of the adsorption isotherm is the inverse of the adsorption isotherm. The adsorption isotherm needs to describe the multilayer adsorption which is mostly described with the following models:

BET
$$\frac{q_e}{q_s} = \frac{C_{BET} C_e}{(C_s - C_e)\left[1 + (C_{BET} - 1)\frac{C_e}{C_s}\right]}; \quad 0 < \frac{C_e}{C_s} \leq 0.5 \tag{3.14}$$

FHH
$$\frac{q_e}{q_s} = -\left[\frac{\alpha}{RT} ln\left(\frac{C_e}{C_s}\right)\right]^b; \quad \frac{C_e}{C_s} \geq 0.8 \tag{3.15}$$

In this work, the FHH isotherm is considered and its inverse is derived and assumes the following expression:

FHH
$$ln\left(\frac{C_e}{C_s}\right) = \frac{\alpha}{RT}\left[\frac{q_s}{q_e}\right]^b \tag{3.16}$$

Or

$$ln\frac{p^{eq}}{p^0(T)} = -\frac{\alpha}{RT}\left[\frac{V_s}{V_e}\right]^b \tag{3.17}$$

The liquid potential is now derived as following:

$$\mu_l = {\mu_v}^0 + R_v T ln\left(p^0(T) exp\left(-\frac{\alpha}{RT}\left[\frac{V_s}{V_e}\right]^b\right)\right) \tag{3.18}$$

$$= {\mu_v}^0 + R_v T\left(ln\left(p^0(T)\right) - \frac{\alpha}{RT}\left[\frac{V_s}{V_e}\right]^b\right)$$

And so the potential difference between the two phases:

$$(\mu_l - \mu_v) = {\mu_v}^0 + R_v T\left(ln\left(p^0(T)\right) - \frac{\alpha}{RT}\left[\frac{V_s}{V_e}\right]^b\right) - {\mu_v}^0 - R_v T lnp \tag{3.19}$$

$$= -R_v T lnS - \alpha\left[\frac{V_s}{V_e}\right]^b$$

Considering this potential difference, the critical embryo assumes the following expression:

$$\frac{\mathrm{d}G_{het}}{dr_e} = \left(-R_v T lnS - \alpha\left[\frac{V_s}{V_e}\right]^b\right)\frac{\rho}{M}4\pi {r_e}^2 + \sigma 8\pi r_e = 0 \tag{3.20}$$

Where:

$$V_e = \frac{4}{3}\pi\left({r_e}^3 - {r_p}^3\right) \tag{3.21}$$

And so:

$$\frac{\mathrm{d}G_{het}}{dr_e} = 0 \tag{3.22}$$

$$\left(-R_v T lnS - \alpha\left[\frac{V_s}{\frac{4}{3}\pi\left({r_e}^3 - {r_p}^3\right)}\right]^b\right)\frac{\rho}{M}4\pi {r_e}^2 + \sigma 8\pi r_e = 0$$

The following equation does not present an analytical solution of r_e and so a numerical analysis is accomplished.

Moreover, it is worthy underline that explicit with respect to *lnS* the equation becomes:

$$lnS = \frac{2\sigma M}{\rho R_v T r_e} - \alpha\left[\frac{V_s}{V_e}\right]^b \tag{3.23}$$

From the Eq. (3.23) it is possible to note that the first term is the same of the Kelvin equation and the second term takes into account the solid-liquid interactions. It is worthy to underline that the mathematical approach to the thermodynamic of the heterogeneous condensation led to the same relation proposed by Laaksonen (Eq.(3.23).[42] The presence of the second term in the Eq. (3.23) justified theoretically the implementation of the correction factor in the Eq. (3.5).

3.2 Particle Abatement

3.2.1 Experimental results on the particle abatement

In this section, the results of the aerosol treatment are presented in terms of total number removal efficiency and removal efficiency for each size channel, Eq. (2.5) and Eq. (2.6), respectively. The results were reported as stacked bars that represent the contribution of the GT and of the treat unit, BC or WES, on both removal efficiencies, as described in the section 2.4.2. The efficiency of each unit, η_i, was graphed as $-\log(1-\eta_i)$ as a function of the channel size and the operating water temperature in order to better appreciate the contribution of the GT and the BC or WES on the removal efficiencies of the whole system.

Sodium Chloride aerosol

Figure 3.9 shows the total removal efficiency of the GT-BC (left) and GT-WES system (right) at the different water film temperatures. For this kind of aerosol, only the total removal efficiency of the whole system GT-BC and GT-WES as a function of the water temperature are reported. Indeed, it was not possible to estimate the contribution of the single GT and treat units, since the salt entering in the dilutor system recrystallized and so a substantial change of the ASD was observed compared with the inlet one.

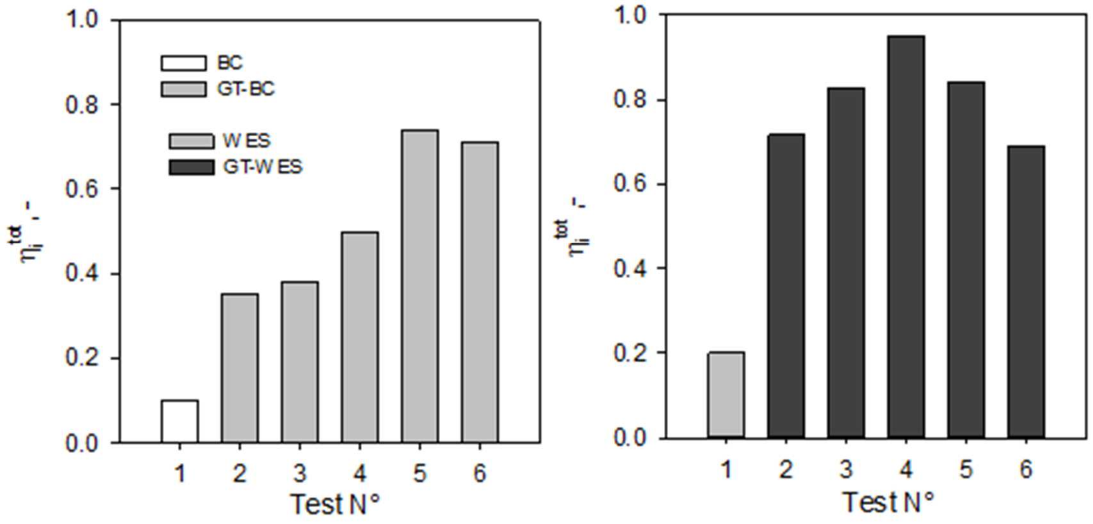

Figure 3-9- Total removal efficiency of the GT-BC and GT-WES systems for the salt aerosol treatment.

The total removal efficiency of the GT-BC system increased significantly with the temperature reaching the maximum value of roughly 80% at 60°C. The removal efficiency of the GT-WES system was always higher than the GT-BC system and reached the maximum value of 95% at 50°C. It worth remembering that the salt aerosol had a wide aerosol size distribution ranging from 15 to 250 nm with a peak at 100nm. According to the Pich's model, the theoretical efficiency of the bubble column has a minimum around 100 nm, therefore in absence of the condensational growth, the particles are poorly captured by the bubble column. Once the heterogenous condensation was active, the particles started to enlarge towards diameter above 300 nm and so they were easily captured. Indeed, at this size Cadavid-Rodriguez et al. [67] showed that the removal efficiency of a bubble column improved. Concerning the removal efficiency of the GT-WES, the maximum removal efficiency revealed at 50°C suggests that the system had an optimum to capture the particles in the particles range from 200 to 300 nm.

OptiBind 0.1 aerosol

Figure 3.10 shows the contribution of the single units in the GT-BC and GT.WES systems for the Optibind 0.1 aerosol treatment plotting $-log(1-\eta)$ as a function of the particles size at the different water temperatures. Figure 3.11 shows the contribution of the single units in both the GT-BC and GT-WES systems on the total removal efficiency plotting $-log(1-\eta)$ as a function of T_W.

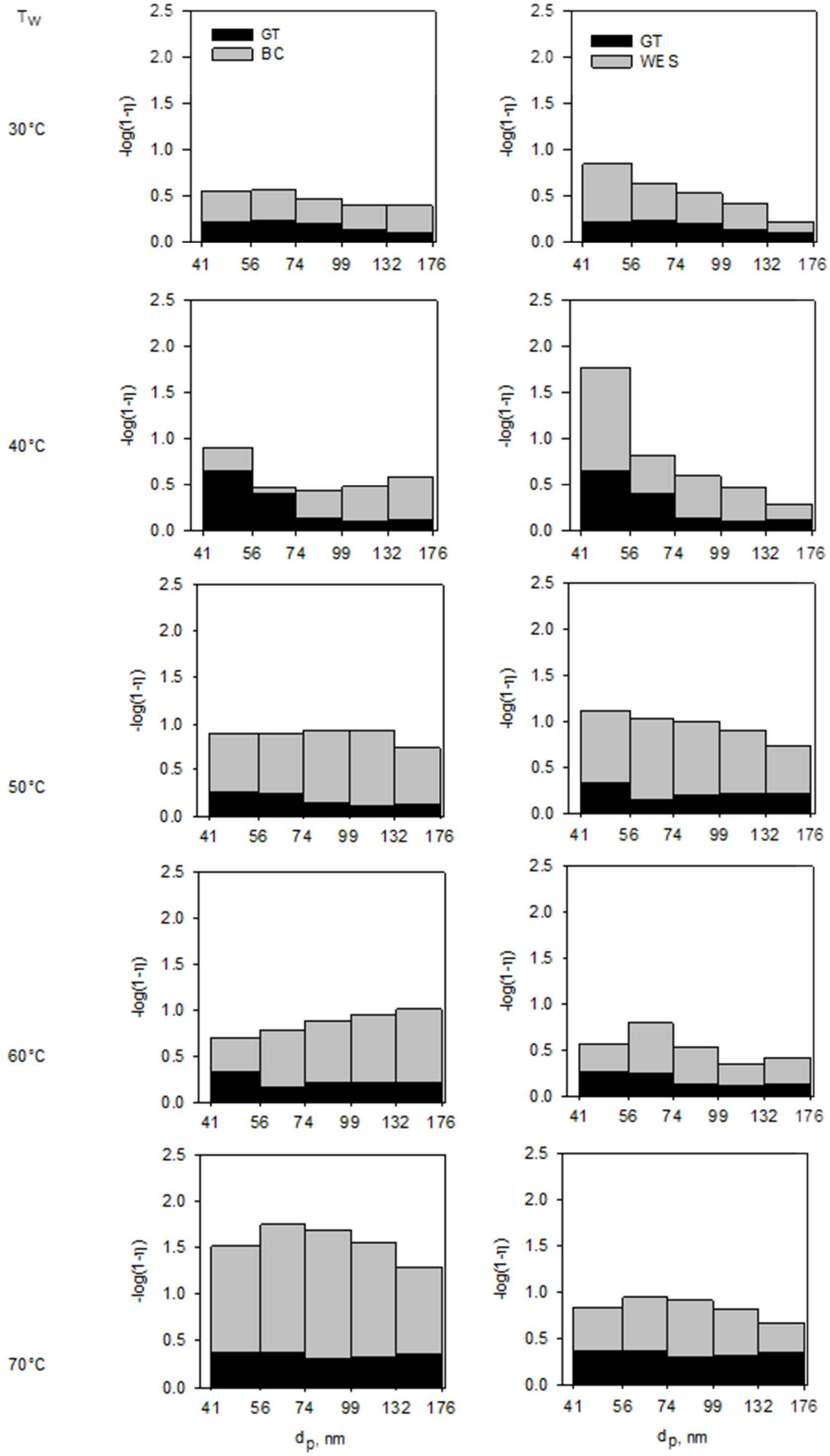

Figure 3-10-The contribution of the GT and BC and WES in the whole system on the removal efficiency of the OptiBind 0.1 for j_{th} particle size for the different T_w.

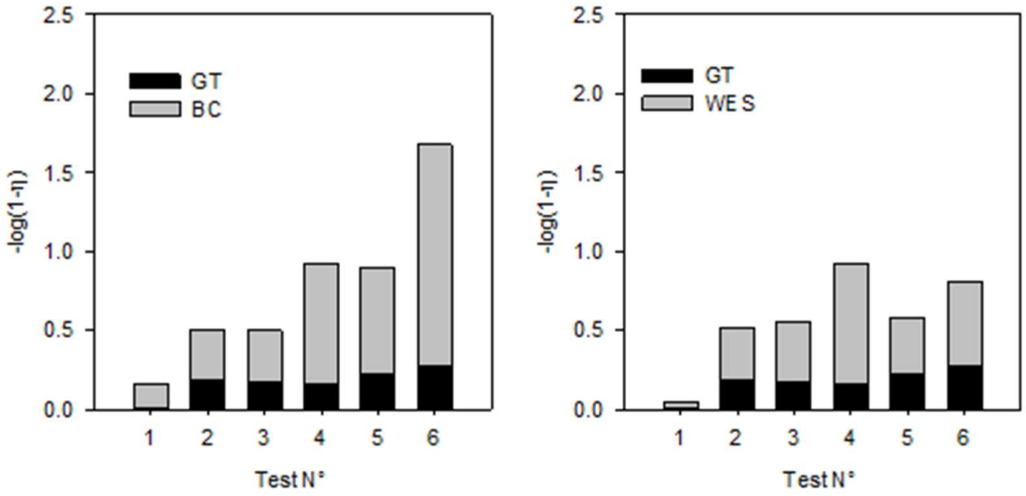

Figure 3-11-The total removal efficiency of OptiBind 0.1 in the GT-BC(a) and in the GT-WES (b) systems for the different operative conditions.

Figure 3.10 shows that the contribution of the GT on the removal efficiency did not change significantly with the temperature, while an important increase of the BC contribution with the temperature for all the particle size was observed. The bubble column had a non-monotonic trend with the particle size at 30°C, that slightly disappear with the temperature reaching quite similar contribution for all the particles range. This result suggests that the particles entering the GT unit, once enlarged to a size above 300 nm, as showed in the Figure 3.3, were easily and similarly captured by the bubble column.

The maximum capture efficiency of the WES was observed for the particles ranging from 41 to 56 nm at 30°C and 40°C. At 50°C all the particles were captured in a similar way, indeed all of them were larger than 200 nm, as showed in the Figure 3.3. The WES reached the maximum contribution at 50°C, confirming the results observed with the salt aerosol treatment. This experimental evidence highlighted the presence of an optimum between the lab-scale WES and the GT. This aspect needs a deep study to be fully understood. The Figure 3.9 clearly shows the improvement of the bubble column when the heterogenous condensation was active and its contribution on the particles capture almost triplicated passing from 30 to 70°C, as reported in Table3.6. The WES benefited of the heterogeneous condensation mainly at 50°C and reached the maximum value of 82%. The GT-BC system had a maximum efficiency of 98.5% at 70°C and was higher than the efficiency of the GT-WES system, that at 70°C was 84%. The removal efficiency of the WES and the BC when the GT was bypassed were lower than that one with the GT operating at T_w=30°C. This results suggests that since it was not observed an appreciable growth, the particles were surrounded by a thin liquid layer that facilitate their capture.

Table 3-6-Summary of the experimental results on the total particle removal efficiency of the OptiBind 0.1 in the growth tube, η_{GT}, bubble column η_{BC}, wet electrostatic scrubber η_{WES}, the GT-BC $\eta_{GT\text{-}BC}$ and and the GT-WES $\eta_{GT\text{-}BC}$ sequences

Test N°	T_w, °C	Total number removal efficiency %				
		$\eta_{GT\text{-}BC}$	$\eta_{GT\text{-}WES}$	η_{GT}	η_{BC}	η_{WES}
1		-	-	-	30±7.5	10
2	30	58±2.5	69±8.7	33.0±3.6	37.8±8.5	54.2±5.3
3	40	66.5±5.6	72.2±9.5	33.5±9.6	50.1±8.5	58.9±5.3
4	50	89.2±2.7	82.7±1.7	30.7±8.2	85.5±9.1	82.7±4.2
5	60	96.8±2.2	73.8±9.4	39.7±8.9	91.2±5.0	46.5±6.4
6	70	98.5±1.6	84.0±7.9	46.5±6.3	93.6±9.0	71.1±7.5

OptiBind 0.2 aerosol

Figure 3.12 shows the contribution of the single units on the removal efficiency of the GT-BC and GT.WES systems for the Optibind 0.2 aerosol treatment. It was plotted $-log(1-\eta)$ as a function of the particles size for the different water film temperatures. Figure 3.13 shows the contribution of the single unit on the total removal efficiency of both the GT-BC and GT-WES systems, plotting - $log(1- \eta)$ as a function of the operative conditions.

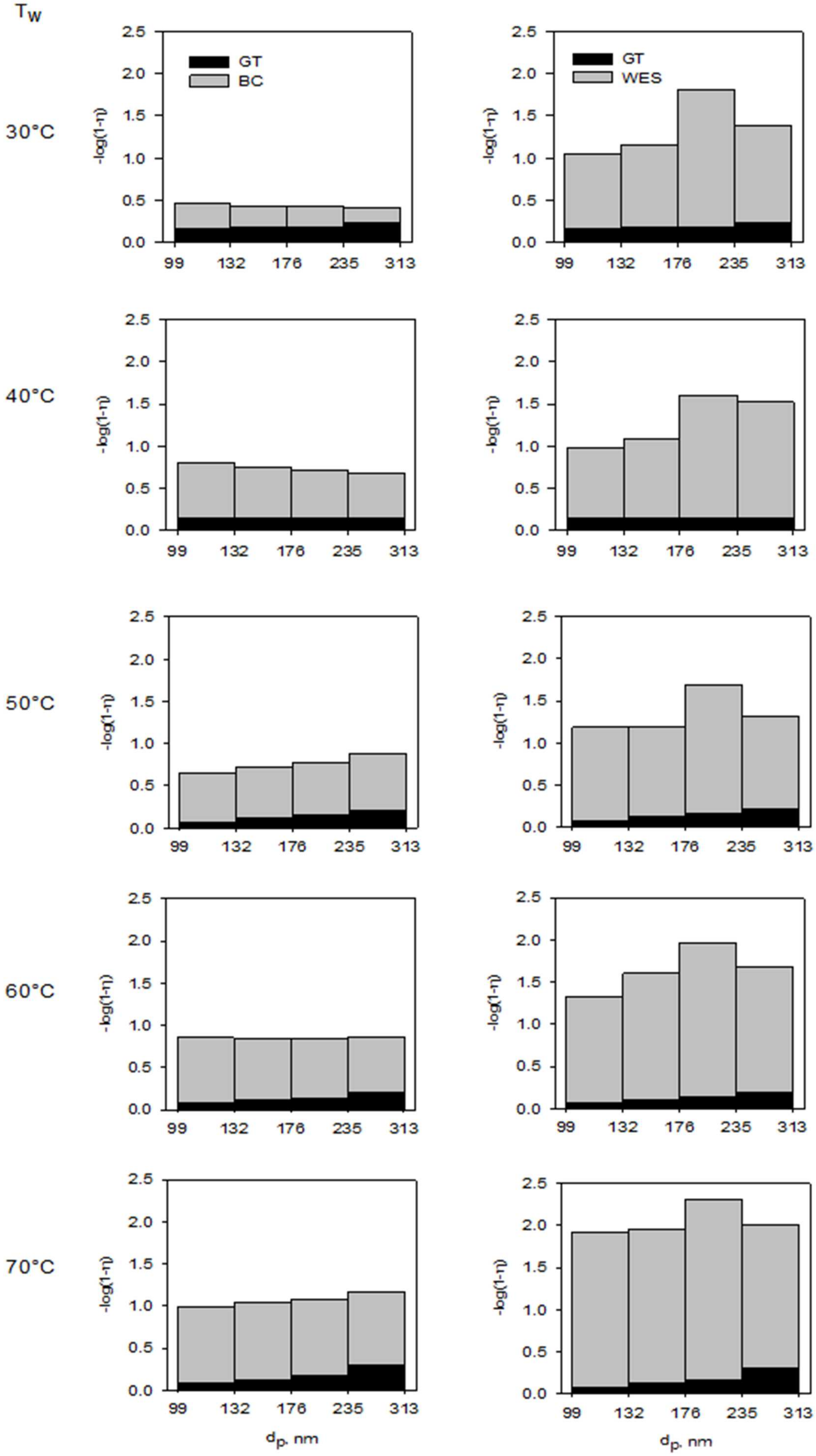

Figure 3-12- The contribution of the GT, BC and WES in the whole system on the removal efficiency of OptiBind 0.2 for jth particle size for the different operative conditions.

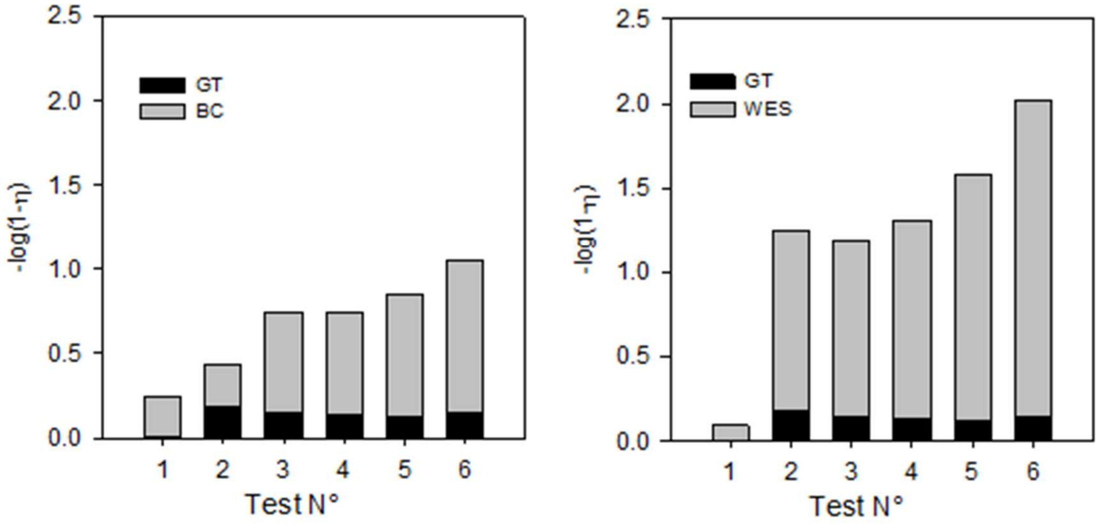

Figure 3-13-The total removal efficiency of the OptiBind 0.2 in the GT-BC (left) and in the GT-WES (right) systems for the different operative conditions.

The Figure 3.12 shows that the GT contribution was quite constant with the temperature and with the particle diameter. Like the GT, the BC efficiency had a constant trend with the particles size, indeed the bubble column had a minimum for the particles of 100 nm, while the OptiBind 0.2 particles had a mean volumetric diameter of 200 nm. The contribution of the BC increased when the heterogeneous condensation occurred suggesting that larger particles were easily captured. The WES was able to capture mainly the particles in the range from 176 to 235 and this trend was preserved with the temperature. As the BC, the WES took advantage of the condensation growth and an improvement of the removal efficiency was observed for all the particle size. This results underlines that all the particles were enlarged by the condensational growth. Moreover, it is worthy to note that passing from 50 to 60°C the increment of the WES contribution on the capture of the particles between 99 and 132 nm was lower than the others particles ranges, suggesting that only a fraction of these particles enlarged towards a size more easily capturable by the WES. Both the units had the best performances at 70°C, as reported in the Table 3.7. The BC passed from 44% to 87%, while the WES, that already at 30°C had a high removal efficiency of 91% improved up to 98.6%. The GT-WES system had a higher efficiency than that one of the GT-BC for all the temperatures and reached a value of 99% at 70°C. The high performance of the WES at 30°C suggests that although the condensational growth was apparently very limited at this temperature, the removal efficiency increased because of the presence of a liquid shell surrounding the particles, which allows improving the efficiency of the aerosol impacts with the water droplets. Indeed, the removal efficiency of the WES without GT was 20%.

Table 3-7-Summary of the experimental results on the total particle removal efficiency of the optiBind 0.2 in the growth tube, η_{GT}, bubble column η_{BC}, wet electrostatic scrubber η_{WES}, the GT-BC η_{GT-BC} and and the GT-WES η_{GT-BC} sequences

Test N°	**T_w, °C**	**Total number removal efficiency %**				
		η_{GT-BC}	**η_{GT-WES}**	**η_{GT}**	**η_{BC}**	**η_{WES}**
1		-	-	-	43.2±4.2	20±9.5
2	30	63.1±2.5	94.3±8.7	34.1±3.6	43.6±8.5	91.4±5.3
3	40	82.0±5.6	82.1±9.5	28.3±9.6	74.9±8.5	90.9±5.3
4	50	75.5±2.7	93.3±1.7	26.2±8.2	66.9±9.1	90.2±4.2
5	60	85.8±2.2	97.3±9.4	24.2±8.9	81.3±5.0	96.5±6.4
6	70	91.2±1.6	99.1±7.9	28.9±6.3	87.6±9.0	98.6±7.5

Titanium dioxide aerosol

Figure 3.14 shows the contribution of the single units on the removal efficiency of the GT-BC and GT.WES systems for the titanium dioxide aerosol treatment. It was plotted $-log(1-\eta)$ as a function of the particles size for the different water film temperatures. Figure 3.15 shows the contribution of the single unit on the total removal efficiency of both the GT-BC and GT-WES systems, plotting $- log(1-\eta)$ as a function of the operative conditions.

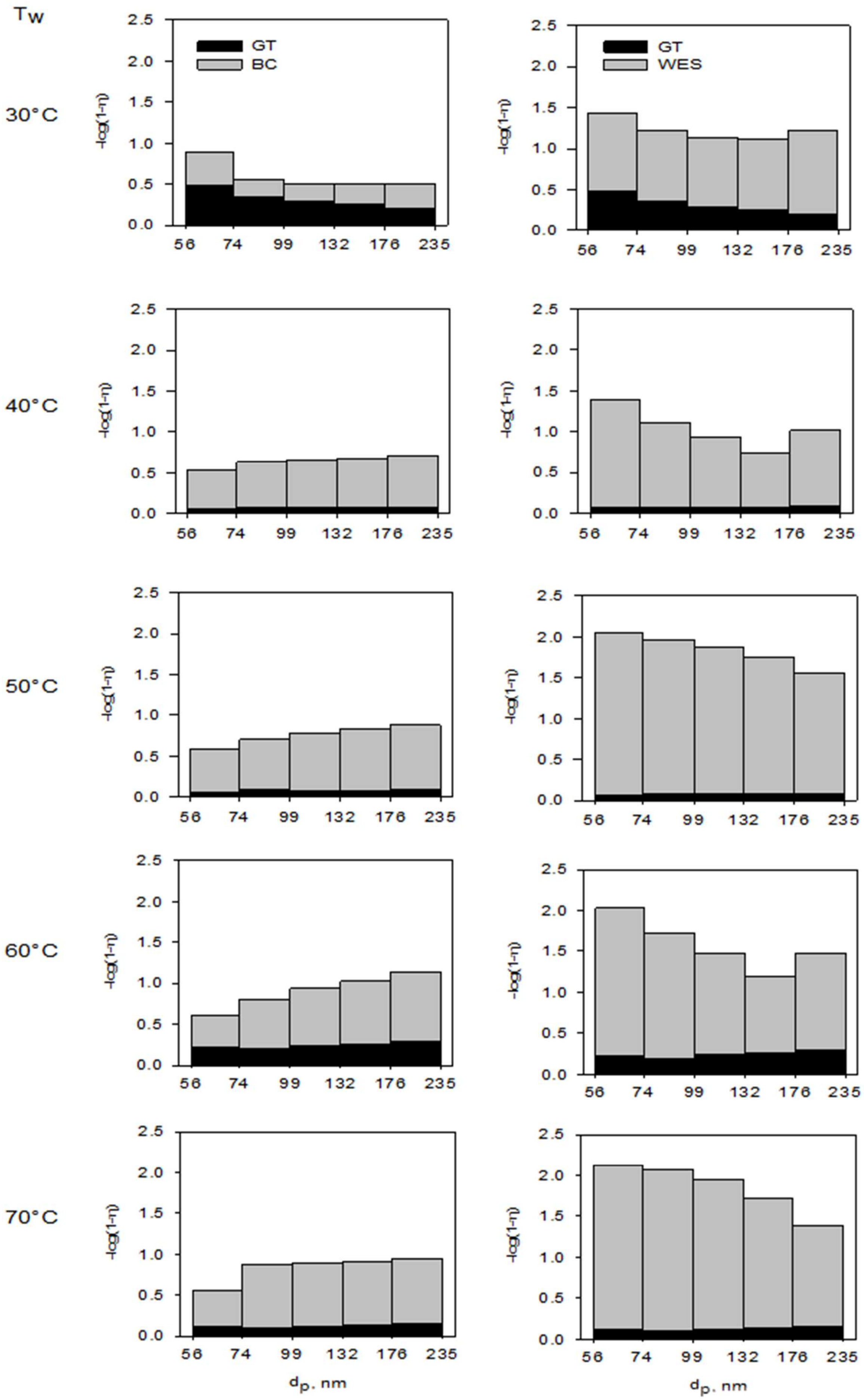

Figure 3-14- The contribution of the GT and BC and WES in the whole system on the removal efficiency of titanium dioxide for jth particle size for the different operative condition, T

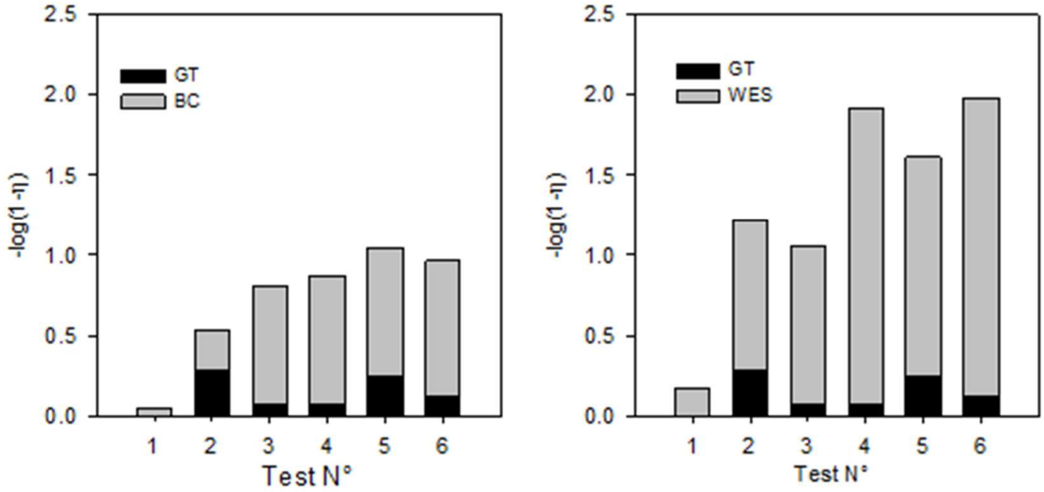

Figure 3-15- The total removal efficiency of titanium dioxide of the GT-BC (a) and of the GT-WES (b) systems for the different operative conditions

The GT contribution on the removal efficiency was constant with the particle size and its maximum contribution was observed at 30 and 60°C. The BC had a non-monotonic trend with the particle size ranging from 99 to 132 at 30°C and this trend slightly disappeared with the temperature. From the Figure 3. 14, the titanium dioxide started to growth at already 30 °C, therefore the minimum of the removal efficiency means that this fraction of particles did not grow. With the temperature increase, all the particle underwent to condensation growth and so the bubble column improved significantly its removal efficiency. The maximum increment was observed at 70°C when all the particles were growth in a size range from 200 to 400 nm. The contribution of the WES on the removal efficiency had a non-specific trend with the particle diameter, but, as the BC, it increased with the temperature and reached the maximum value of 98% at 50 and 70°C, as reported in the table 3.8. The BC efficiency doubled passing from 30 to 70°C. The GT-WES system had a higher efficiency than the GT-BC one. Indeed, the first system captured always the 90% in number of the particles, while the GT-BC system reached the maximum value of 88% at 70°C. The removal efficiency of the WES and the BC when the GT was bypassed were lower than that one at the water film temperature of 30°C. Indeed, at this temperature it was observed already a significant aerosol enlargement.

Table 3-8-- Summary of the experimental results on the total particle removal efficiency of the titanium dioxide in the growth tube, η_{GT}, bubble column η_{BC}, wet electrostatic scrubber η_{WES}, the GT-BC η_{GT-BC} and and the GT-WES η_{GT-BC} sequences

Test N°	**T_W, °C**	**Total number removal efficiency %**				
		η_{GT-BC}	**η_{GT-WES}**	**η_{GT}**	**η_{BC}**	**η_{WES}**
1		-	-	-	10±6.5	34±5.3
2	30	70.3±3.9	93.8±8.7	48.6±5.7	42.2±8.5	88.1±5.3

3	40	77.9±2.6	91.2±9.5	15.8±2.7	73.8±8.5	89.5±5.3
4	50	82.9±0.7	98.7±1.7	16.6±3.6	79.5±9.1	98.5±4.2
5	60	88.4±1.1	97.5±9.4	43.3±12.1	79.6±5.0	95.7±6.4
6	70	87.6±7.1	98.9±7.9	25.6±15.6	83.4±9.0	98.5±7.5

Carbon black aerosol

Figure 3.16 shows the contribution of the single units on the removal efficiency of the GT-BC and GT.WES systems for the carbon black aerosol treatment. It was plotted *-log(1-η)* as a function of the particles size for the different water film temperatures. Figure 3.17 shows the contribution of the single unit on the total removal efficiency of both the GT-BC and GT-WES, plotting - *log(1-η)* as a function of the operative conditions.

.

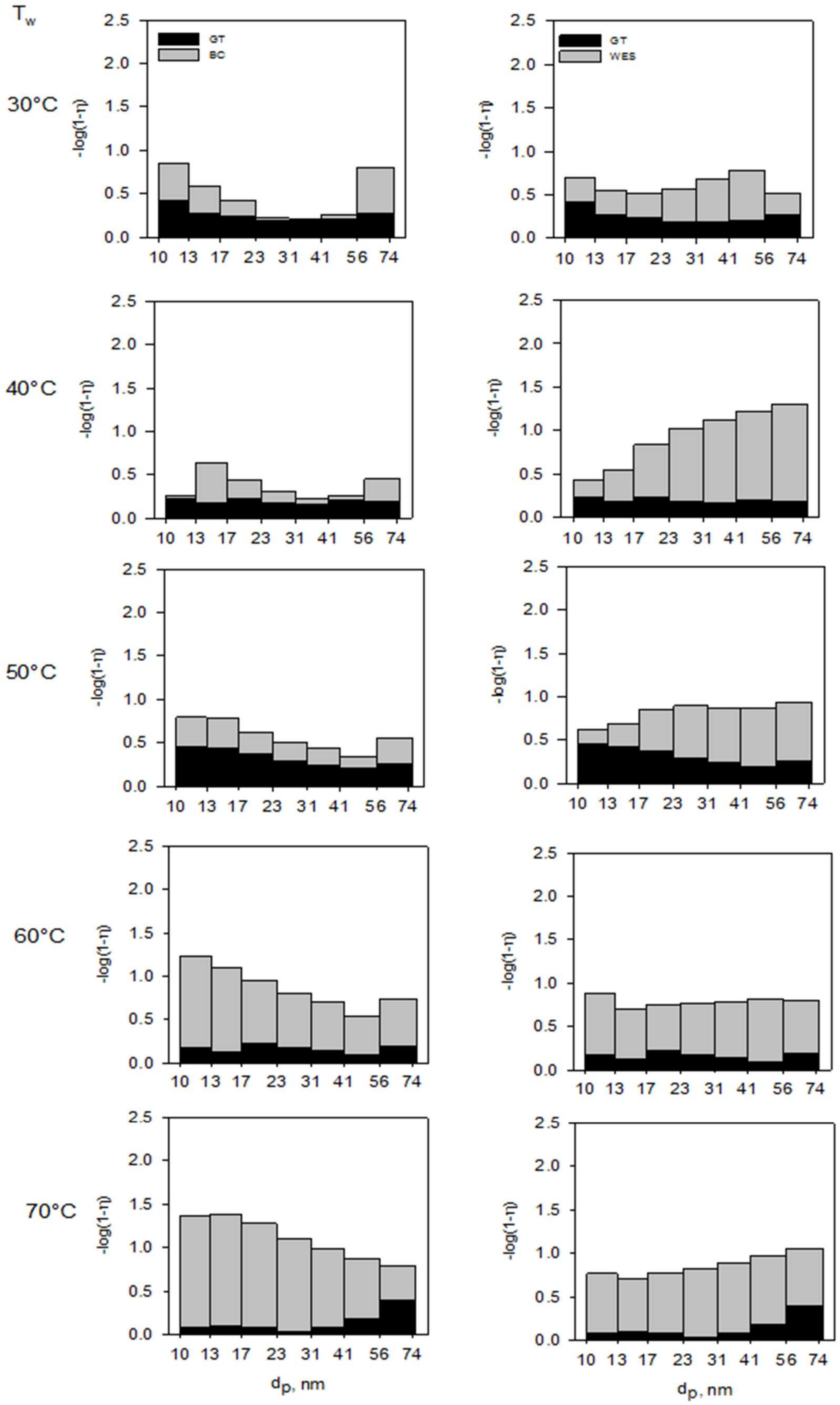

Figure 3-16 he contribution of the GT and BC and WES in the whole system on the removal efficiency of the carbon black for jth particle size for the different operative temperature Tw.

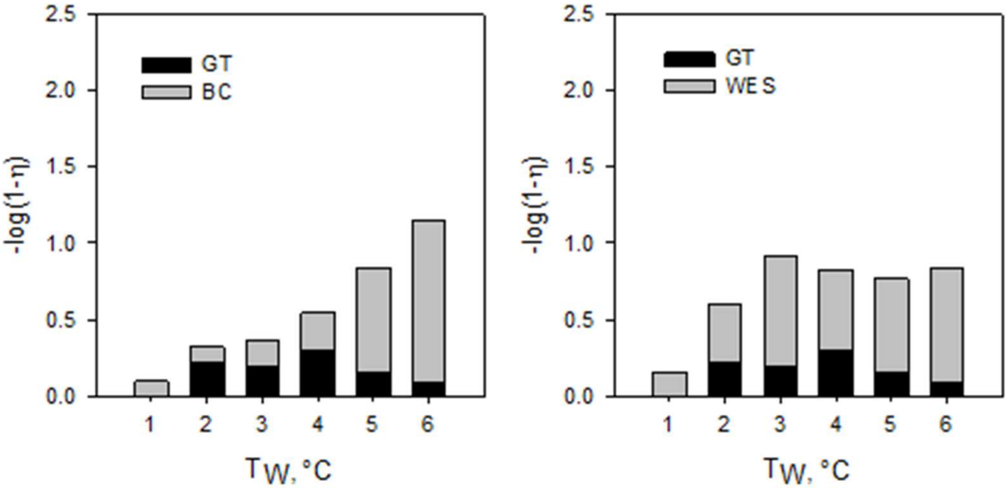

Figure 3-17- The total removal efficiency of the carbon black of the GT-BC (a) and of the GT-WES (b) systems for the different operative conditions

The contribution of the Gt was not negligible on the removal efficiency and its maximum contribution was observed at 50°C while the minimum at 70°C. The contribution of the GT dropped off with the temperature because these nanoparticles were strongly affected by the Stefano flow that took place in the growth tube when the water temperature raised. The removal efficiency of the bubble column had a non-monotonic trend with the particle size with a minimum ranging from 27 to 48 nm. This trend slightly disappeared once the heterogeneous condensation occurred and at 60°C the maximum increment on the removal efficiency was observed. These experimental results suggests that the particles growth observed at already 30°C was due to the enlargement of that fraction of particles with an initial diameter around 100 nm that were poorly detectable with the SMPS 3910 due to their low concentration. At 60°C, in the growth tube a supersaturation level that trigger the condensation growth of also the smallest particles was reached. The removal efficiency of the WES had a non-monotonic trend with the particle size with a maximum in the range from 31 to 54 nm. This trend disappeared when the heterogeneous condensation was active and in particular the capture of the particles in the range 56-74 nm significantly incremented already at 40°C. At 60°C the capture mechanisms of the WES improved and become similarly for all the particle size. The Figure 2.15 shows that the contribution of the BC and WES on the total removal efficiency clearly improved with the temperature. Both the BC and the WES improved significantly their performance when the heterogeneous condensation was active passing from 20% to 91% and from 57% to 82% respectively, as reported in the table 3.9. The GT-BC system had a higher efficiency than the GT-WES system at the temperatures of 60 and 70°C at which value of 85% and 92% were reached, respectively. The BC efficiency without GT was quite similar at that one with the GT operating at 30°C. This observation confirmed that the observed aerosol enlargement was due to the grow of particles larger than 74 nm that were not measured by the TSI 3910.

Table 3-9-- Summary of the experimental results on the total particle removal efficiencyof the cabon balck in the growth tube, η_{GT}, bubble column η_{BC}, wet electrostatic scrubber η_{WES}, the GT-BC $\eta_{GT\text{-}BC}$ and and the GT-WES $\eta_{GT\text{-}BC}$ sequences

Test N°	**Tw, °C**	**Total number removal efficiency %**				
		$\eta_{GT\text{-}BC}$	$\eta_{GT\text{-}WES}$	η_{GT}	η_{BC}	η_{WES}
1		-	-	-	21±2.3	31±3.4
2	30	52.4±6.8	74.5±8.7	40.6±9.8	20.2±8.5	57.5±5.3
3	40	57.5±10.1	88.0±9.5	35.8±8.8	33.8±8.5	81.3±5.3
4	50	71.6±9.8	85.0±1.7	50.4±5.6	42.3±9.1	69.8±4.2
5	60	85.5±9.2	82.9±9.4	30.8±1.1	79.1±5.0	75.4±6.4
6	70	92.8±4.5	85.2±7.9	18.16±2.7	91.2±9.0	82.2±7.5

3.2.2 Discussion

Particle capture in the HC-WES and HC-BC

The interpretation of the experimental results on the removal efficiency at this moment presents several issues. Firstly, it was not possible to correlate the removal efficiency with the effective diameter of the particles that entered the treatment units. Indeed, the removal efficiency was based on how many of the original particles entering the systems were removed. This implied the use of the TSI SMPS 3910 whose pre-treatments prevented the measure of the liquid aerosols. Besides, the aerosol size distribution measured at the exit of the growth tube should be considered only as qualitative, because the actual size of the particles is miscalculated by the calibration algorithm of the optical counter. Indeed, the measurements of the aerosol size with the TSI LAS 3340 is affected by an unknown calibration effect (expected to be within a +30% increase of the measured size) and by the lower detection limit of the instrument that is 80 nm. Therefore, it is not possible to know exactly what is the aerosol size distribution entering the BC or the WES, although one can effectively measure how the GT affect their removal efficiency toward the raw solid particles.

In the next paragraphs, the analysis of experimental evidences on bubble column and wet electrostatic units is reported.

Condensational growth assisted Bubble column

Although these difficulties, a try to apply the Pich’s model to describe the experimental efficiencies of the bubble column was accomplished. To this goal, an optical analysis was performed and so the bubble size distribution of the bubbles was estimated, as shown in the Figure 3.18.

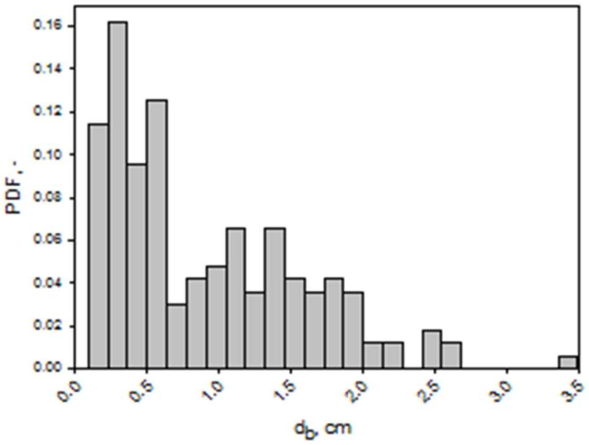

Figure 3-18- Average bubble size distribution inside the bubble column.

The bubbles exhibited different shapes, e.g. small spherical, ellipsoidal and irregular shaped bubbles, with a wide bubble size distribution, which is shown in Figure 3. According to the bubble size distribution, the mean bubble diameter was found as 0.9 cm. The bubble velocity was evaluated according the relation proposed by Pich and Schutz. [26]

Apart from the aforementioned experimental difficulties to correlate the efficiency towards the effective particles, several points limited the applicability of the Pich’s model. In particular, a strong bubble coalescence during the bubble rising and a high turbulence with an intense bubble deformation at the exit of the distributor was observed. These phenomena led to a bubble size distribution varying in the time and in the space and to internal motions that severely modified the conditions under which Pich’s model can be applied. Nevertheless, we tried applying Pich’s model to our data, following the approach of Charvet et al. [20] and Koch and Weber [66], but we calculated very low removal efficiency, in the range of 2-5% for all the particles.

So according to the Pich’s model, the removal efficiency of the bubble column adopted in this work would be really low in. This observation led to scrutinize the real contribution of the water of the bubble column keeping out that one of the porous distributor and to effectively ascribe to the condensational growth the improvement of the system in the GT-BC system. To this aim, two sets of tests were carried out: a first one operating the bubble column without water with and without the GT, a second one feeding the bubble column with a heated aerosol at the same temperature, T_G, at which it exits from the GT. To perform these experiments, we bypassed the saturator and the growth tube and flowed the gas through a 6 m metal tube immersed in the thermostatic bath. The experiments were carried out both with an empty and a HPLC water filled bubble column. Finally, we also performed tests with the GT unit and the empty bubble column to exploit the role of gas distributor and wall of the column on the particle capture. The polystyrene nanoparticles with mean diameter of 100 nm were used. Table 1 resumes the tests on particle capture. Each type of test was labelled to simplify the description of results.

Table 3.10 resumes the tests on particle capture. Each type of test was labelled to simplify the description of results.

Table 3-10--Experimental tests resume

T_W (K)	**GT**	**GT-BC**	**GT-BC_{empty}**
298	D1	E1	F1
303	D2	E2	F2
323	D3	E3	F3
343	D4	E4	F4
353	D5	E5	F5
T_G (K)	**BC**	**BC_{empty}**	
298	G1	H1	
298	G2	H2	
318	G3	H3	
338	G4	H4	
348	G5	H5	

Figure 3.19 shows a flowchart of the experimental tests carried out to study the particles abatement.

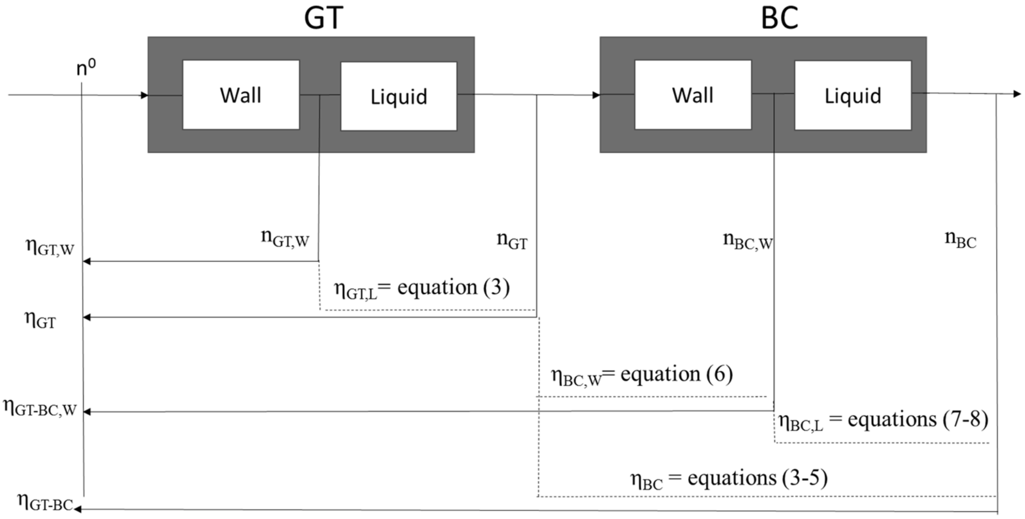

Figure 3-19- Flowchart of the experimental campaign for particle capture efficiency

The flowchart shows the contribution of the single unit on the total removal efficiency. For all the run tests, both the GT and the BC efficiencies were split in the contribution of the wall (denoted by subscript “W”) and the liquid (denoted by the subscript “L”).

Table 3.11 shows the removal efficiency of the total particle removal efficiencies of the GT, BC, BC_{empty}, GT-BC_{empty} and GT-BC system calculated from the experimental data of the tests D, E, F, and G, respectively. Table 4 reports the derived removal efficiency of the bubble column liquid, from the tests E and G, the removal efficiency of the distributor and wall of the bubble column from the tests F, and the removal efficiency of the bubble column from the tests E.

The numbering of tests from 1 to 5 in Table 3.11 and 3.12 stands for the operating temperature of water film T_w in GT for the tests D, E, F and the temperature T_G of gas entering the bubble column for the tests G, H. The numbering mirrors the increase of both temperatures.

Table 3-11-Summary of the experimental results on the total particle removal efficiency in the growth tube, η_{GT}^{D}, bubble column η_{BC}^{G}, growth tube with the bubble column distributor only $\eta_{GT\text{-}BC,W}^{F}$ and the GT-BC sequence $\eta_{GT\text{-}BC}^{E}$

N°	Total number removal efficiency %		
	$\eta_{GT\text{-}BC,W}^{F}$	η_{BC}^{G}	$\eta_{BC,W}^{H}$
1	45.4±3.2	37.8±8.5	21.6±5.3
2	45.4±3.2	37.8±8.5	21.6±5.3
3	51.0±3.5	40.1±9.1	26.5±4.2
4	78.2±2.2	35.7±5.0	24.1±6.4
5	88.0±4.1	62.2±9.0	48.9±7.5

Table 3-12- Summary of the experimental results on the evaluated removal efficiency of the bubble column from the tests E (η_{BC}^{E}), the wall and the distributor contribution from the tests F ($\eta_{BC,W}^{F}$), the contribution of the liquid from the tests E and G ($\eta_{BC,L}^{G}$, $\eta_{BC,L}^{E}$)

N°	Total number Efficiency %			
	$\eta_{BC,L}^{E}$	$\eta_{BC,L}^{G}$	$\eta_{BC,W}^{F}$	η_{BC}^{E}
1	23.6	20.6	21.6	37.8
2	39.11	20.6	17.9	50.1
3	77.9	18.5	34.4	85.5
4	85.4	15.3	39.5	91.2
5	87.5	31.2	49.3	93.6

Experiments revealed that the total efficiency increased with the temperature for all the investigated units, as reported in Table 3.12. The growth tube alone provided a particle capture of roughly 30% for the operative condition 1 and 2 and increased up to 76 % for water film temperature of 353 K (N° 5).

The removal efficiency of the distributor and wall of the bubble column, investigated in the test H and F was not negligible and significant changed was observed when the water temperature increased from 343 to 353 K. It was roughly 25% for the tests N°1-2-3-4 and increased up to 49% for the test N°5. The experimental results showed that the contribution of the distributor and wall for the test F was higher than that one of the tests H for the operative conditions N°3-4. This discrepancy was due to the heterogeneous condensation as it is deductible from the Figure 8. At the operative condition N°5, the contribution of this portion of the bubble column was similar when the growth tube was bypassed.

From the test G, the efficiency of the BC was quite constant at value of 34% with the gas temperature until 338 K and then increased up to 62% at 348 K. These results are consistent with the experimental findings of Koch and Weber. [66] The increment with the temperature can be explained by considering the occurrence of phoretic forces on the deposition of particles on the wall of the BC and the distributor. [121] The removal efficiency of the bubble column estimated from the test E had a significant increment with the temperature of the water film, indicating the positive effects of the heterogeneous condensation. Indeed, it passed from 38% to 94% for T_w of 303 and 353 K, respectively. Similar conclusions were deductible comparing the contribution of the liquid in the bubble column between the test E and G. The experimental results showed that the BC improved its performance when the heterogeneous condensation was active. In particular, when the condensational growth occurred, the removal efficiency of the BC doubled (Table 3.12)

From the CDF data in Figure 3.3 it appears that when the supersaturation increased and T_w is higher than 343 K, more than 60% of the particles were enlarged at a size larger than the original particle size. At 353 K this percentage increased to more than 80% and more than 85% of the particles were larger than 200 nm. However, it is worth remembering that the calibration of LAS 3340 underestimates the size of water-solid particles. At this size, Cadavid-Rodriguez et al·[67] reported that bubble column removal efficiency is higher than 25%. In our opinion, the removal efficiency also increased because of the presence of a liquid shell surrounding the particles, which allows improving the efficiency of the aerosol impacts with the water-gas interface. Indeed, we noticed that the water contribution rapidly increased between tests N°1 and N°2 although the condensational growth was apparently very limited. We think that this occurrence may depended on the presence of a small layer of water surrounding the particles leaving the GT, which resulted enough to improve the number of effective impacts with the gas-liquid interface of the bubbles. This, together with the parallel improvement of the growth tube, allowed achieving removal efficiency higher than 90% for all the particle size range.

Figure 3.20 shows the different contribution evaluated from the test E of the GT, of the distributor and wall of the bubble column and of the liquid of the bubble column on the total removal efficiency and on that one for each particle size range. The $-\log(1-\eta)$ was plotted for the different tests N°1-5. It is worth underline that the *-log(1-η)* is proportional to the efficiency: the bigger the stacked bar the higher the contribution on the removal efficiency.

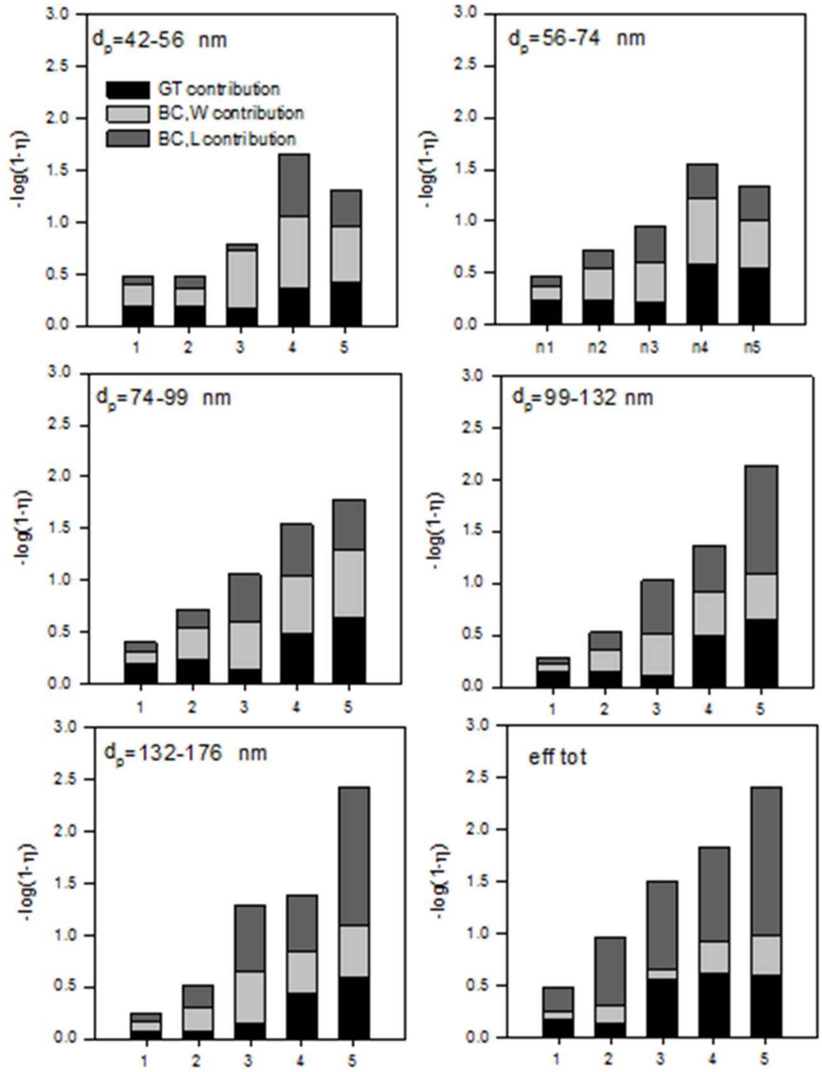

Figure 3-20- The GT (black), BC, W (light grey), BC,L (dark grey) contributions on the total removal efficiency and on the efficiency for each particle size.

From the Figure 3.20 it is possible to note that the removal efficiency had a non-monotonic trend with the particle size, as observed by Charvet et al.[20] and La Motta et al. [122], with a minimum in the range 99-132 nm for all the temperatures except for that at T_w=353 K. Indeed, the dark and light grey stacked bar in this particle range were lower than that one of the other particle ranges. For the diameters ranging from 42 to 74 nm the contribution of the GT increased from the test N°1 to the test N°4 and then unchanged. For the particle size ranging from 74 to 176 nm the particle abatement in the GT increased passing from the test N°1 to N°5. The contribution of the distributor and wall slightly increased with the temperature for all the particle size ranges, while the contribution of the liquid of the bubble column increased significantly for the particles ranged from 99 to 176 nm. The total removal efficiency for the particles ranged from 74 to 99 nm raised considerably while for the particles from 42 to 74 nm decreased when the temperature. Overall, the total removal efficiency increased with the temperature of the water film and the liquid of the bubble column had the major benefits when the heterogeneous condensation occurred.

<u>Condensational growth assisted wet electrostatic scrubber</u>

The experimental results of Wet Electrostatic Scrubber were described in light of scavenging model proposed by Di Natale et al. [18], [98]. The model was developed for an OPES configuration and estimated a theoretical collection efficiency as a function of inertial, Brownian, phoretic and electrostatic contributions on particles capture. Regarding the electrostatic effects, the authors regarded the attractive Coulomb force acting between droplets and particles, and the image forces induced from droplets (or particles) on uncharged particles (or droplets). For the CDES configuration that was performed in this study, the electrostatic effect on particle collection efficiency was studied limited to the image forces exerted from charged droplets towards the uncharged particles. This contribution was estimated according to the Equation (1.34):

$$E_{Im} = \left[\frac{15\cdot\pi}{8}\cdot\frac{\varepsilon_p-1}{\varepsilon_p+2}\cdot\frac{2C_c\left(q_D/\pi\cdot d_D^2\right)^2\cdot d_p^2}{3\cdot\pi\cdot\mu_g\cdot U\cdot\varepsilon_0 d_D}\right]^{0.4} \tag{1.34}$$

where ε_p is the particle relative dielectric permittivity, ε_0 is the vacuum dielectric permittivity, q_D is the droplet charge, U is the relative velocity liquid-gas that was set coincident with the droplets velocity considering the entering gas stream in WES much slower. C_C is the Cunningham factor evaluated as:

$$C_c = 1 + \frac{2\,\lambda_a}{d_p}\left(1.257 + 0.4exp\left(-\frac{1.1d_p}{2\lambda_a}\right)\right) \tag{3.6}$$

where λ_a is the air free mean path that is 68 nm.

The image force collisional efficiency was estimated both for particles enlarged by a water layer and for dry particles bypassing the growth unit. In the first case, the particles relative dielectric permittivity was set as that of water; in the second case, it was that of starting material. The total droplets charge was measured by means a Faraday Cage that collected them and at which an electrometer Keythley 6513 was connected to. The charge was measured as mean value of 2500 values countered by the instrument. The single droplet charge q_D was obtained by dividing the total droplets charge for the number of formed droplets N, which was given by the ratio of volumetric liquid flow rate and volume of a droplet with diameter d_D.

In Figure 3.21, the collisional efficiency E_{Im} for the tested materials is graphed as function of particle diameter.

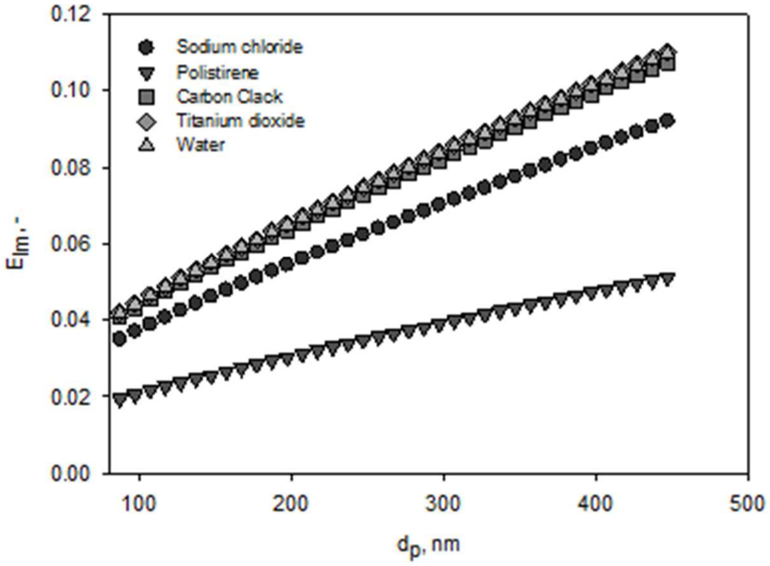

Figure 3-21- Electrostatic collisional efficiency for all materials

The image forces contribution is more consistent as the dielectric permittivity of particles is high. Indeed, from Figure 3.21, it can be noted that at fixed particle diameter, the polystyrene and the titanium dioxide showed the lowest and highest effect of electric field on collisional efficiency, respectively. Noticeably, a water droplet of the same size exploited an electrostatic efficiency close to that of titanium dioxide. Assuming that image charges on the liquid solid aerosol is equal to those occurring on a droplet of the same size, it appears that once the particles are enlarged by a water layer, the effect of image forces increased up to a factor 5. For example, if a 100 nm polystyrene particle passing in the growth tube becomes a liquid-solid aerosol of 400 nm, E_{Im} increased from 0.02 to 0.10. Similarly, apart Brownian's contribution, all the other components of the collisional efficiency increased with the size of the aerosols for d_p>200 nm, as shown in Figure 3.22 for all materials.

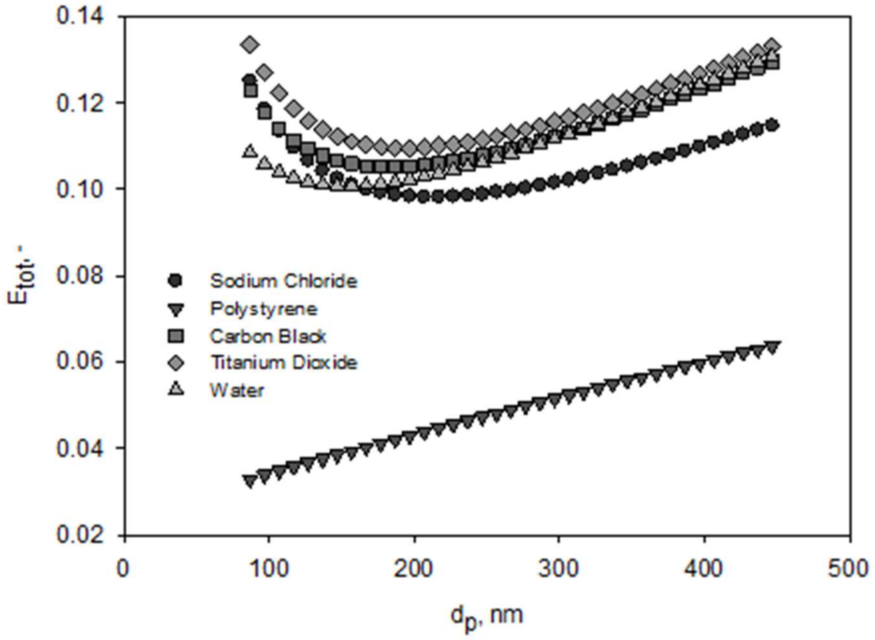

Figure 3-22- Total collisional efficiency for all materials

The collisional efficiency contributions were evaluated according the relations listed in Table 1.3. The polystyrene particles showed an increasing trend with particle size suggesting that the minimum of E_{tot} could be at particle diameters lower than investigated ones. Omitting the polystyrene, for particles smaller than 200 nm, the difference between sodium chloride, carbon black, titanium dioxide and water was due to the thermophoretic diffusion because of a lower thermal conductivity of water droplets, while at d_p>200 nm the sodium chloride differentiated from the four materials for the lower dielectric permittivity.

Once the particles were enlarged and covered by a water film, the total collisional efficiency increased considerably, as confirmed by WES experimental removal efficiencies reported in Chapter 3.

The total collisional efficiency for dry particles reflected the WES performances when the aerosols entered bypassing the growth tube. Indeed, the lowest values of E_{tot} estimated for polystyrene particles clarify the reason why the removal efficiency was 0.1 and 0.2 for OptiBind 0.1 and 0.2, respectively. It was due for the low dielectric permittivity and thermal conductivity. For the sodium chloride, carbon black and titanium dioxide the experimental removal efficiencies of WES were 0.2, 0.31 and 0.34, respectively. The higher values for carbon black and titanium dioxide for the opposite reasons of polystyrene and for a more consistent effect of Inertial Impaction collisional efficiency for the high densities of these materials. The sodium chloride has a halfway behaviour. Anyway, the lower removal efficiency compared with CB and titanium dioxide is due to the less influent electrostatic collisional efficiency.

In Table 3.13 are listed the parameters of collisional efficiencies constant for all materials. In Table 3.14 are reported the physical properties that depended on material nature.

Table 3-13- Parameters of collisional efficiency equations

Parameters	
ε_0, F/m	$8.82 \cdot 10^{-12}$
μ_w, Pa·s	$1 \cdot 10^{-3}$
μ_g, Pa·s	$1.81 \cdot 10^{-5}$
ρ_w, Kg/m^3	$1 \cdot 10^{+3}$
λa, m	$68 \cdot 10^{-9}$
Q_D, C	$2.75 \cdot 10^{-9}$
N, #	90.82
d_D, m	$1.12 \cdot 10^{-3}$
U, m/s	0.77
k_B, J/K	$1.38 \cdot 10^{-23}$
k_g, W/m·K	$2.50 \cdot 10^{-2}$
T_D, K	298
T_G, K	303
P, Pa	$1 \cdot 10^{+5}$
Re, -	$8.62 \cdot 10^{+2}$
Pr, -	$7.13 \cdot 10^{-1}$
D_w, m^2/s	$2.82 \cdot 10^{-5}$

Table 3-14- Physical properties of tested materials in collisional efficiency equations

Parameters/Material	**Sodium Chloride**	**Polystyrene**	**Carbon Black**	**Titanium Dioxide**	**Water**
ε_r, F/m	5.9	1.5	31.2	114	80.2
ρ_P, kg/m^3	2165	1040	2800	3800	1000
k_P, W/m·K	6.5	0.033	1.7	11.8	0.591

Beyond the increase of the collection efficiency, Di Natale et al. [113] indicated that, when a hot gas comes into contact with a cold electrified water in conditions favouring water condensation on the drops in an opposite polarity electrostatic scrubber operated in conditions similar to those investigated here, phoretic forces positively influences the capture of droplets larger than 300 nm. Therefore, the formation of aerosols with size larger than the parent particles lead to higher removal efficiencies. Besides, the efficiency improved even when low or even negligible particles enlargement was observed, as far as a liquid layer is present on them. We envisage that this experimental finding mirrored the effects of the increase in the thermal conductivity of water (affecting thermophoresis), the effects on polarization phenomena and a possible improvement on the interfacial interactions with the water droplets, as observed for the bubble column.

Conclusion

The present work faced the study of an innovative system to remove fine and ultrafine particles. The system was based on the concept to couple two treatment units, the bubble column and the wet electrostatic scrubber, with a preconditioning technique, as the heterogeneous condensation. Indeed, the condensational growth of particles that took place in a specific growth tube allowed to improve the performances of the clean technologies. Five different material were tested: the sodium chloride, the titanium dioxide, calibrated polystyrene nanoparticles (nominal diameter 100nm and 200nm) and carbon black nanoparticles. A first study was accomplished to monitor the enlargement of the aerosol size distribution at the exit of the growth tube by varying the water film temperature T_w from 30 to 70°C. A second study had the purpose of estimating the particle removal efficiency of the bubble column and the WES assisted by the heterogeneous condensation.

Preliminary tests on the abatement of the GT showed that the growth unit had a kind of “cut-off” for particles larger than 500 nm. Therefore, all the particles that enlarged above 500 nm were not detected and so the aerosol size distributions of tested particles at the GT exit spanned from 80 to 500 nm. Although this observation, a condensational growth of all the tested particles was observed for the different operating conditions.

The growth tube led to the formation of larger liquid-solid aerosols as far as the temperature of the liquid film T_w increased for the tested particles. The sodium chloride started to grow at 30°C and the count mean diameter of its aerosol size distribution passed from 135 to 315 nm. Both the OptiBind 0.1 and 0.2 articles enlarged as soon as the temperature was higher than 30 °C. The OptiBind 0.1 inlet aerosol size distribution ranged from 90 to 297 nm and shifted in size range spanning from 149 to 400 for the condensational growth. The OptiBind 0.2 showed a narrow distribution around 200 nm at the inlet and a particles distribution at GT exit ranging from 258 to 410 nm. The titanium dioxide started to growth at 30°C and passed from a wide distribution to a narrow one. The gradually temperature increase led to a gradually raising of a peak at 410 nm. The carbon black enlarged when the temperature reached already 30°C and all the particles enlarged towards particle size of roughly 350 nm. The experimental evidences showed that in the condensation growth, although the inescapable presence of a water layer that cover the particles, it must be taking into account even the contribution of the adsorption in the calculation of the minimum of the free energy of the system particle-embryo-vapor. Indeed, imposing that the embryo in order to exist has to be in equilibrium with its vapor phase, without considering the links due to the adsorption that make it linked to the surface, leads to an overestimation of the supersaturation levels.

The removal efficiency of the BC and the WES, indeed, benefited of the particles growth and their removal efficiency increased significantly when the heterogeneous condensation was active for all the tested particles. The experimental results showed that the removal efficiency of the bubble column increased as soon as the particles, whatever their nature was, reached a size larger than 300 nm, as showed by Cadavid-Rodrigues et al.[67]. The maximum benefit of the BC was observed at 70°C for all the materials and from 30°C to 70°C the efficiency increased about 100%, 148%, 100%, 100%, 350% for the sodium chloride, OptiBind 0.1, OptiBind0.2, titanium dioxide and carbon black, respectively.

The experimental results on the removal efficiency of the WES showed an optimum with the water temperature of 50°C for all materials. The maximum increment of the removal efficiency was 33%, 53%, 7%, 12% and 43% for the sodium chloride, OptiBind 0.1, OptiBind 0.2, titanium dioxide and carbon black particles, respectively.

Furthermore, the experimental results showed that for the OptiBind 0.2 polystyrene nanoparticles a removal efficiency higher than 90% was reached at already 30°C, when the particle enlargement generated by the condensational growth apparently was very limited. This experimental result suggests that the presence of a thin water liquid layer surrounding the particles, undetectable in size with the LAS 3340, minimized the rebounding phenomena that occurs between the particles and the water droplets generated by the electrospray.

The two units had an improvement in terms of removal efficiency even when a not appreciable enlargement was observed and so the increment was ascribable to the presence of a thin liquid layer surrounding the particles. Indeed, this conclusion was confirmed by the observed efficiencies of the two units operating without GT that were lower than that one coupled with the GT operating at 30°C.

Thanks to the promising results obtained in these experimental tests, the new system earns a chance to become a reliable alternative aerosol treatment for industrial application.

References

[1] W. Hinds, “Aerosol Technology,” *Methods Biochem. Anal.*, vol. 2, pp. 0–471, 2001.

[2] F. R. Rita Van Dingenena, J.-P. Putaud, U. Baltensperger, A. C. C, M.-C. Facchini, S. Decesari, S. Fuzzi, R. Gehrig, H.-C. Hansson, R. M. Harrison, C. H. . E, Alan, M. Jones, P. Lajg, G. Lorbeerh, W. Maenhauti, F. Palmgrenj, X. Querolk, S. Rodriguezk, J. S. . H, H. ten Brinkl, P. Tunvedf, B. W. , Kjetil T^rsethm, E. Weingartnerb, A. Wiedensohlern, and P. Wahlin, “A European aerosol phenomenology—1: physical characteristics of particulate matter at kerbside, urban, rural and background sites in Europe,” *Atmos. Environ.*, vol. 38, pp. 2561–2577, 2004.

[3] Amec, “European Commission Industrial emissions of nanomaterials and ultrafine particles,” no. October, 2011.

[4] D. V Spracklen and C. L. Heald, “The contribution of fungal spores and bacteria to regional and global aerosol number and ice nucleation immersion freezing rates,” *Atmos. Chem. Phys*, vol. 14, pp. 9051–9059, 2014.

[5] E. Levitater and G. O. Rubel, “Aerosol Chemical Processes in the Environment.” pp. 197–211, 2000.

[6] G. Oberdörster, Z. Sharp, V. Atudorei, A. Elder, R. Gelein, W. Kreyling, and C. Cox, “Translocation of Inhaled Ultrafine Particles to the Brain,” *Inhal. Toxicol.*, vol. 16, no. 6–7, pp. 437–445, 2004.

[7] G. Oberdorster, J. Ferin, R. Gelein, S. C. Soderholm, and J. Finkelstein, “Role of the alveolar macrophage in lung injury: Studies with ultrafine particles,” *Environ. Health Perspect.*, vol. 97, pp. 193–199, 1992.

[8] R. Beelen, G. Hoek, P. A. van den Brandt, R. A. Goldbohm, P. Fischer, L. J. Schouten, M. Jerrett, E. Hughes, B. Armstrong, and B. Brunekreef, “Long-term effects of traffic-related air pollution on mortality in a Dutch cohort (NLCS-AIR study),” *Environ. Health Perspect.*, vol. 116, no. 2, pp. 196–202, 2008.

[9] Achille MARCONI, “Materiale particellare aerodisperso: definizioni, effetti sanitari, misura e sintesi delle indagini ambientali effettuate a Roma,” *Ann Ist Super Sanità*, vol. 39, no. 3, pp. 329–342, 2003.

[10] World Health Organization, “WHO Air quality guidelines for particulate matter, ozone, nitrogen dioxide and sulfur dioxide: global update 2005: summary of risk assessment,” 2006.

[11] Eea, *Air quality in Europe — 2013 report*, no. 9. 2013.

[12] F. Di Natale and C. Carotenuto, “Particulate matter in marine diesel engines exhausts: Emissions and control strategies,” *Transp. Res. Part D Transp. Environ.*, vol. 40, pp. 166–191, 2015.

[13] C. Ridurre and L. O. Smog, “MAL ’ ARIA DI CITTÀ 2017,” 2017.

[14] M. Tammaro, “Heterogeneous condensation for submicronic particles abatement.”

[15] S. Bari, C. W. Yu, and T. H. Lim, “Filter clogging and power loss issues while running a diesel engine with waste cooking oil,” *Proc. Inst. Mech. Eng. Part D J. Automob. Eng.*, vol. 216, no. 12, pp. 993–1001, 2002.

[16] R. Sanchirico, P. Russo, V. Di Sarli, and A. Di Benedetto, “On the explosion and flammability behavior of mixtures of combustible dusts,” *Process Saf. Environ. Prot.*, vol. 94, pp. 410–419, 2015.

[17] A. Denkevits, “Explosibility of hydrogen–graphite dust hybrid mixtures,” *J. Loss Prev. Process Ind.*, vol. 20, no. 4, pp. 698–707, 2007.

[18] C. Carotenuto, F. Di Natale, and A. Lancia, “Wet electrostatic scrubbers for the abatement of submicronic particulate,” *Chem. Eng. J.*, vol. 165, no. 1, pp. 35–45, 2010.

[19] A. Jaworek, A. Krupa, and T. Czech, “Modern electrostatic devices and methods for exhaust gas cleaning: A brief review,” *J. Electrostat.*, vol. 65, no. 3, pp. 133–155, 2007.

[20] A. Charvet, N. Bardin-monnier, and D. Thomas, “Can bubble columns be an alternative to fibrous filters for nanoparticles collection?,” *J. Hazard. Mater.*, vol. 195, pp. 432–439, 2011.

[21] S. Heidenreich and F. Ebert, “Condensational droplet growth as a preconditioning technique for the separation of submicron particles from gases,” *Chem. Eng. Process.*, 1995.

[22] S. Heidenreich, “Condensational droplet growth in the continuum regime—a critical review for the system air-water,” *J. Aerosol Sci.*, vol. 25, no. 1, pp. 49–59, 1994.

[23] J. E. McDonald, “Homogeneous nucleation of vapour condensation.1.Thermodynamic aspects,” *Am. J. Phys.*, 1962.

[24] N. H. Fletcher, “Size Effect in Heterogeneous Nucleation,” *J Chem Phys*, vol. 29, no. 3, p. 572,

1958.

[25] V. Y. Smorodin and P. K. Hopke, “Condensation Activation and Nucleation on Heterogeneous Aerosol Nanoparticles,” *J Phys Chem*, 2004.

[26] L. Krastanov, “On the activity of semi-wettable substances as condensation,” 1957.

[27] X. Luo, Y. Fan, F. Qin, H. Gui, and J. Liu, “A kinetic model for heterogeneous condensation of vapor on an insoluble spherical particle,” *J. Chem. Phys.*, vol. 140, no. 2, 2014.

[28] E. Meszaros, “On the thermodynamics of the condensation on water soluble and mixed particles,” 1969.

[29] D. Kashchiev, “Analysis of experimental data for the nucleation rate of water droplets,” *J. Chem. Phys.*, vol. 125, no. 4, p. 44505, 2006.

[30] S. Heidenreich, U. Vogt, H. Büttner, F. Ebert, H. Bu, F. Ebert, H. Büttner, and F. Ebert, “A novel process to separate submicron particles from gases - a cascade of packed columns,” *Chem. Eng. Sci.*, vol. 55, no. 15, pp. 2895–2905, 2000.

[31] F. Fan, L. Yang, J. Yan, and Z. Yuan, “Numerical analysis of water vapor nucleation on PM2.5 from municipal solid waste incineration,” *Chem. Eng. J.*, vol. 146, no. 2, pp. 259–265, 2009.

[32] J. PODZIMEK and J. C. CARTENS, “The 100 year evolution of Aitken nuclei counters current and future problems,” *J. Rech. atmosphériques*, vol. 19, no. 2–3, pp. 257–274.

[33] H. Köhler, “The nucleus in and the growth of hygroscopic droplets,” *Trans. Faraday Soc.*, vol. 32, no. 0, pp. 1152–1161, 1936.

[34] G. MILOSHEV and L. KRASTANOV, “Influence of adsorption on the formation of embryo lunules,” *Tellus*, vol. 15, no. 3, pp. 297–302, Aug. 1963.

[35] A. W. ADAMSON and I. LING, “Contact Angle, Wettability, and Adhesion,” in *Contact Angle, Wettability, and Adhesion*, vol. 43, 1964, pp. 57–73.

[36] J. C. H. Van der Hage, “Condensation on Insoluble Particles,” *J. Colloid Interface Sci.*, vol. 91, no. 2, 1983.

[37] C.-C. Chen, L.-C. Hung, and H.-K. Hsu, “Heterogeneous Nucleation of Water Vapor on Particles of SiO2, Al2O3, TiO2, and Carbon Black,” *Journal of colloid and interface science*, vol. 157. pp. 465–477, 1993.

[38] D. Nordstrand, F. Wheeler, and B. G. Miller, “Post-Combustion Emissions Control.”

[39] J. Porstendörfer, H. G. Scheibel, F. G. Pohl, O. Preining, G. Reischl, and P. E. Wagner, "Heterogeneous Nucleation of Water Vapor on Monodispersed Ag and NaCl Particles with Diameters between 6 and 8 nm," *Aerosol Sci. Technol.*, vol. 4, no. November 2015, pp. 65–79, 1985.

[40] J. A. Koutsky, A. G. Walton, and E. Baer, "Heterogeneous nucleation of water vapor on high and low energy surfaces," *Surf. Sci.*, vol. 3, no. 2, pp. 165–174, Apr. 1965.

[41] E. Ruckenstein, G. O. Berim, and G. Narsimhan, "A novel approach to the theory of homogeneous and heterogeneous nucleation," *Adv. Colloid Interface Sci.*, vol. 215, pp. 13–27, 2015.

[42] A. Laaksonen, "A unifying model for adsorption and nucleation of vapors on solid surfaces," *J. Phys. Chem. A*, 2015.

[43] P. J. Pomonis and E. T. Tsaousi, "Frenkel-Halsey-Hill equation, dimensionality of adsorption, and pore anisotropy," *Langmuir*, vol. 25, no. 17, pp. 9986–9994, 2009.

[44] B. J. McCoy, "Vapor Nucleation and Droplet Growth: Cluster Distribution Kinetics for Open and Closed Systems," *J Colloid Interface Sci*, vol. 228, no. 1, pp. 64–72, 2000.

[45] J. Aitken, "On Improvements in the Apparatus for Counting the Dust Particles in the Atmosphere.," *Proc. R. Soc. Edinburgh*, vol. 16, pp. 135–172, Sep. 1890.

[46] P. H. Mcmurry, "The History of Condensation Nucleus Counters," vol. 322, pp. 297–322, 2000.

[47] J. C. Barrett and H. J. Fissan, "Aerosol growth by condensation chamber," vol. 20, no. 3, pp. 279–288, 1989.

[48] W. Li, N. Montassier, and P. K. Hopke, "A System to Measure the Hygroscopicity of Aerosol A System to Measure the Hygroscopicity of Aerosol Particles," *Aerosol Sci. Tech.*, no. November 2014, pp. 37–41.

[49] J. Bao, L. J. Yang, B. Lu, J. Geng, J. P. Yan, X. L. Shen, G. Besagni, F. Inzoli, G. De Guido, L. A. Pellegrini, A. Charvet, N. Bardin-Monnier, D. Thomas, E. Commission, Z. Dai, D. Fornasiero, J. Ralston, A. Dehbi, D. Suckow, S. Guentay, J. L. L. E. H. M. J. Escudero, M. M. E. V Peyrés, J. P. Ch, K. M. K. Koch, U. B. H. Unger, L. M. C. D. Ch, S. W. Trow, A. V. J. E. Bonanni, M. C. A. Alonso, S. A. Grinshpun, K. Willeke, V. Ulevicius, A. Juozaitis, S. Terzieva, J. Donnelly, G. N. Stelma, K. P. Brenner, S. Heidenreich, U. Vogt, H. Büttner, F.

Ebert, L. E. Herranz, M. J. Escudero, J. Polo, Y. Huang, M. Takaoka, N. Takeda, T. G. Kaldor, C. R. Phillips, H. J. H. G. Kim, H. J. H. G. Kim, M. H. Lee, J. H. Kim, D. Koch, A. P. Weber, H. Liu, G. Wei, R. Zhang, B. C. Meikap, M. N. Biswas, A. V. A. V. Nguyen, H. J. H. J. Schulze, J. Ralston, H. J. H. J. Schulze, S. H. Park, B. K. Lee, B. Raj Mohan, B. C. Meikap, D. Reay, G. A. Ratcliff, A. G. Szekely, J. P. Yan, L. J. Yang, X. Zhang, L. J. Sun, Y. Zhang, X. L. Shen, L. F. Zhang, and S. Taniguchi, "A novel process to separate submicron particles from gases - a cascade of packed columns," *J. Aerosol Sci.*, vol. 53, no. 2, pp. 59–82, 2000.

[50] J. Hienola, M. Kulmala, and A. Laaksonen, "Condensation and evaporation of water vapor in mixed aerosols of liquid droplets and ice:numerical comparison of growth rate expressions," *jounrmal aersol Sci.*, vol. 32, p. 24, 2001.

[51] S. P. Fisenko and A. A. Brin, "Heat and mass transfer and condensation interference in a laminar flow diffusion chamber," *Int. J. Heat Mass Transf.*, vol. 49, no. 5, pp. 1004–1014, 2006.

[52] S. P. Fisenko, W.-N. Wang, M. Shimada, and K. Okuyama, "Vapor condensation on nanoparticles in the mixer of a particle size magnifier," *Int. J. Heat Mass Transf.*, vol. 50, no. 11, pp. 2333–2338, 2007.

[53] G. Cozzolino, M. De Joannon, R. Ragucci, and A. Cavaliere, "Efficiency Evaluation of a Condensational Scrubber for Particulate Abatement : Preliminary Results," in *XXXIV Meeting of the Italian Section of the Combustion Institute*, 2011, pp. 1–6.

[54] J. Xu, Y. Yu, J. Zhang, Q. Meng, and H. Zhong, "Heterogeneous condensation of water vapor on particles at high concentration," *Powder Technol.*, vol. 305, pp. 71–77, 2017.

[55] M. Tammaro, F. Di Natale, A. Salluzzo, and A. Lancia, "Heterogeneous condensation of submicron particles in a growth tube," *Chem. Eng. Sci.*, vol. 74, pp. 124–134, 2012.

[56] C.-C. C. Chen, M.-S. S. Guo, Y.-J. J. Tsai, and C. C. Huang, "Heterogeneous nucleation of water vapor on submicrometer particles of SiC, SiO2, and naphthalene," *J. Colloid Interface Sci.*, vol. 198, no. 198, pp. 354–367, 1998.

[57] L. B. W. and W. Strauss, "A study of steam injection into wet scrubbers," *Ind. Eng. Chem. Fundam.*, pp. 362–369, 1971.

[58] Yoshida T., K. Y., and O. K., "Growth of aerosol particles by condensation," *Ind. Eng. Chem. Fundam.*, pp. 37–41, 1976.

[59] S. Calvert and H. M. Englund, *Handbook of Air Pollution Technology*. New York, 1984.

[60] T. Johannessen, J. A. Christensen, O. Simonsen, and H. Livbjerg, “The dynamics of aerosols in condensational scrubbers,” *Chem. Eng. Sci.*, vol. 52, no. 15, pp. 2541–2556, 1997.

[61] L. Yang, J. Bao, J. Yan, J. Liu, S. Song, and F. Fan, “Removal of fine particles in wet flue gas desulfurization system by heterogeneous condensation,” *Chem. Eng. J.*, vol. 156, no. 1, pp. 25–32, 2010.

[62] Y. Huang, M. Takaoka, and N. Takeda, “Removal of unburned carbon from municipal solid waste fly ash by column flotation,” vol. 23, pp. 307–313, 2003.

[63] J. Yan, L. Yang, X. Zhang, L. Sun, Y. Zhang, and X. Shen, “Separation of PM2.5 from combustion based on vapor condensation and scrubbing,” *J. Fuel Chem. Technol.*, vol. 36, no. 3, pp. 267–272, 2008.

[64] N. Kantarci, F. Borak, and K. O. Ulgen, “Bubble column reactors,” *Process Biochem.*, vol. 40, no. 7, pp. 2263–2283, 2005.

[65] F. Particles, D. Reay, and G. A. Ratcliff, “Removal of Fine Particles from Water by Dispersed Air Flotation : Effects of Bubble Size and Particle Size on Collection Efficiency,” *Can. J. Chem. Eng.*, vol. 5, no. 2, pp. 178–185, 1973.

[66] D. Koch and A. P. Weber, “Separation of gas-borne nanoparticles in bubble columns,” *J. Aerosol Sci.*, vol. 53, pp. 61–75, 2012.

[67] M. C. Cadavid-rodriguez, A. Charvet, D. Bemer, and D. Thomas, “Optimization of bubble column performance for nanoparticle collection,” *J. Hazard. Mater.*, vol. 271, pp. 24–32, 2014.

[68] A. Dehbi, D. Suckow, and S. Guentay, “THE EFFECT OF LIQUID TEMPERATURE ON POOL SCRUBBING OF AEROSOLS Figure 2 : DF vs pool temperature (PA24),” vol. 28, no. 97, pp. 707–708, 1997.

[69] I. Kaneko, M. Fukasawa, M. Naito, K. Miyata, and M. Matsumoto, “Experimental study on aerosol removal effect by pool scrubbing,” 1993.

[70] K. Akita and F. Yoshida, “Bubble Size, Interfacial Area, and Liquid-Phase Mass Transfer Coefficient in Bubble Columns,” *Ind. Eng. Chem., Process Des. Dev.*, vol. 13, pp. 84–90, 1974.

[71] M. Sato, N. Kudo, and M. Saito, “Surface Tension Reduction of Liquid By Applied Electric Field Using Vibrating Jet Method,” vol. 34, no. 2, pp. 294–300, 1998.

[72] G. Besagni, F. Inzoli, G. De Guido, L. A. Pellegrini, P. Milano, and V. Lambruschini, “The dual effect of viscosity on bubble column hydrodynamics,” *Chem. Eng. Sci.*, vol. 158, no. October 2016, pp. 509–538, 2017.

[73] C. England, J. R. Grace, and M. E. Weber, “Bubbles, Drops, and Particles DEPARTMEVT OF CHEMICAL E h G I h E E R I N G.”

[74] J. Pich and W. Schütz, “On the theory of particle deposition in rising gas bubbles: The absorption minimum,” *J. Aerosol Sci.*, vol. 22, no. 3, 1991.

[75] B. . Meikap and M. . Biswas, “Fly-ash removal efficiency in a modified multi-stage bubble column scrubber,” *Sep. Purif. Technol.*, vol. 36, no. 3, pp. 177–190, 2004.

[76] G. W. Penney, “Electrified Liquid Spray Dust-Precipitators,” 2357354, 1944.

[77] W. Balachandran, A. Krupa, W. Machowski, and A. Jaworek, “Smoke precipitation by charged water aerosol,” *J. Electrostat.*, vol. 51–52, no. 1–4, pp. 193–199, 2001.

[78] W. Balachandran, A. Jaworek, A. Krupa, J. Kulon, and M. Lackowski, “Efficiency of smoke removal by charged water droplets,” *J. Electrostat.*, vol. 58, no. 3–4, pp. 209–220, 2003.

[79] A. Jaworek, W. Balachandran, M. Lackowski, J. Kulon, and A. Krupa, “Multi-nozzle electrospray system for gas cleaning processes,” *J. Electrostat.*, vol. 64, no. 3–4, pp. 194–202, 2006.

[80] G. Biskos, K. Reavell, and N. Collings, “Electrostatic characterisation of corona-wire aerosol chargers,” *J. Electrostat.*, vol. 63, no. 1, pp. 69–82, 2005.

[81] T. Sato, “Charging process of fine particles in unipolar ion flow,” *Trans. I.E.E. Jpn*, vol. 107, pp. 155–161, 1987.

[82] S.-B. K. T. Seto, T. Orii, H. Sakurai, M. Hirasawa, “Ion beam charging of aerosol nanoparticles,” *Aerosol Sci. Technol*, vol. 39, pp. 750–759, 2005.

[83] S. Matsukada and H. Masuda, “Electrostatics of particles,” *Adv. Powder Technol.*, vol. 14, no. 2, pp. 143–166, 2003.

[84] S. Matsukada, H. Maruyama, T. Matsuyama, and M. Ghadiri, “Triboelectric charging of powders: a review,” *Chem. Eng. Sci.*, vol. 65, pp. 5781–5807, 2010.

[85] A. Maisels, F. Jordan, and H. Fissan, “On the effect of charge recombination on the aerosol charge distribution in photocharging systems,” *J.Aerosol Sci.*, vol. 34, pp. 117–132, 2003.

[86] C. G. Noll, W. Miller, and C. Bracikowski, “Charge-carrier extraction from air and nitrogen gas streams that entrain charge from a radioactive ionizer,” *J. Electrost.*, vol. 54, pp. 283–291, 2002.

[87] A. Schiel, A. P. Weber, G. Kasper, and H. J. Schmid, “In-Situ determination of the charging of nanometer and submicron particles at high temperatures,” *Part. Syst. Charact*, vol. 19, pp. 410–418, 2002.

[88] J. P. Borra, “Charging of aerosol and nucleation in atmospheric pressure electrical discharges,” *Plasma Phys. Control*, vol. 50, 2008.

[89] A. Mizuno, J. S. Clements, and R. H. Davis, “Use of an electron beam for particle charging,” *IEEE Trans. Ind. Appl*, vol. 26, no. 1, pp. 29–35, 1990.

[90] A. Jaworek and A. Krupa, *Charged Sprays Generation*, no. i. Nova Science Publishers, Inc., 2011, pp. 1–100.

[91] A. Jaworek, “Micro- and nanoparticle production by electrospraying,” vol. 176, pp. 18–35, 2007.

[92] N. Ashgriz, *Handbook of atomization and sprays: theory and applications*, vol. 1. 2011.

[93] A. Jaworek and A. Krupa, “Jet and drops formation in electrohydrodynamic spraying of liquids . A systematic approach,” vol. 27, no. November 1998, 1999.

[94] P. Miao, W. Balachandran, P. Xiao, O. Lastow, W. Balachandran, L. L. F. L. F. Agostinho, G. Tamminga, C. U. Yurteri, S. P. Brouwer, E. C. Fuchs, J. C. M. Marijnissen, B. Ambravaneswaran, S. D. Phillips, O. A. Basaran, H. J. Subramani, S. D. Phillips, O. A. Basaran, A. Borner, Z. Li, D. A. Levin, M. Cloupeau, A. Jahangiri, K. Adibkia, J. M. Grace, J. C. M. Marijnissen, R. P. A. Hartman, D. J. Brunner, D. M. A. Camelot, J. C. M. Marijnissen, B. Scarlett, M. K. I. Khan, A. Nazir, A. A. Maan, J. R. Melcher, G. I. Taylor, T. R. Melcher, G. I. Taylor, G. Riboux, Á. G. Marín, I. G. Loscertales, A. Barrero, A. V Subbotin, A. N. Semenov, L. L. F. L. F. Agostinho, L. Jolla, S. Verdoold, L. L. F. L. F. Agostinho, C. U. Yurteri, J. C. M. Marijnissen, H. Search, C. Journals, A. Contact, M. Iopscience, I. P. Address, A. I. Zhakin, P. A. Belov, H. Search, C. Journals, A. Contact, M. Iopscience, and I. P. Address, “Morphology of water electrosprays in the simple-jet mode,” *J. Aerosol Sci.*, vol. 25, no. 1, pp. 1–176, 2013.

[95] L. L. F. Agostinho, “Electrohydrodynamic Atomization in the Simple-Jet Mode: Out-scaling and Application,” 2013.

[96] C. CLANET and J. C. LASHERAS, “Transition from dripping to jetting,” *J. Fluid Mech.*, vol. 383, p. S0022112098004066, Mar. 1999.

[97] L. D’Addio, C. Carotenuto, W. Balachandran, A. Lancia, and F. Di Natale, “Experimental analysis on the capture of submicron particles (PM0.5) by wet electrostatic scrubbing,” *Chem. Eng. Sci.*, vol. 106, pp. 222–230, 2014.

[98] L. D’Addio, F. Di Natale, C. Carotenuto, W. Balachandran, A. Lancia, L. D’Addio, F. Di Natale, C. Carotenuto, W. Balachandran, and A. Lancia, “A lab-scale system to study submicron particles removal in wet electrostatic scrubbers,” *Chem. Eng. Sci.*, vol. 97, pp. 176–185, Jun. 2013.

[99] W. Licht, *Air pollution control engineering: basic calculations for particulate collection*. 1988.

[100] C. W. Lear, W. F. Krieve, and E. Cohen, “Charged Droplet Scrubbing for Fine Particle Control,” *J. Air Pollut. Control Assoc.*, vol. 25, no. 2, pp. 184–189, Feb. 1975.

[101] W. Slinn, “Precipitation scavenging in atmospheric sciences and power production,” 1983.

[102] H. T. Kim, C. H. Jung, S. N. Oh, and K. W. Lee, “Particle removal efficiency of gravitational scrubber considering diffusion, interception, and impaction,” *Enviromental Eng. Sci.*, vol. 18, no. 2, 2001.

[103] C. H. Jung and K. W. Lee, “Filtration of Fine Particles by Multiple Liquid Droplet and Gas Bubble Systems,” *Aerosol Sci. Technol.*, vol. 29, no. 5, pp. 389–401, 1998.

[104] H. M. Davenport and L. K. Peters, “Field studies of atmospheric particulate concentration changes during precipitation.,” *Atmos. Environ.*, no. 1963, 1977.

[105] K. A. Nielsen and J. C. Hill, “Capture of Particles on Spheres by Inertial and Electrical Forces,” *Ind. Eng. Chem., Fundam.*, 1976.

[106] A. Jaworek, A. Krupa, A. T. Sobczyk, A. Marchewicz, M. Szudyga, T. Antes, W. Balachandran, F. Di Natale, and C. Carotenuto, “Submicron particles removal by charged sprays. Fundamentals,” *J. Electrostat.*, vol. 71, no. 3, pp. 345–350, 2013.

[107] M. J. Pilat, S. A. Jaasund, and L. E. Sparks, “Collection of Aerosol Particles by Electrostatic Droplet Spray Scrubbers,” 1908.

[108] J. A. Cross, J. C. W. Fowler, and G. Fu, “Electrostatic Enhancement of water sprays for coal

dust suppression," Sydney, Australia, 2003.

[109] H. T. Yang, S. Viswanathan, W. Balachandran, and M. B. Ray, "Modeling and measurement of electrostatic spray behavior in a rectangular throat of pease-anthony venturi scrubber," *Environ. Sci. Technol.*, vol. 37, no. 11, pp. 2547–2555, 2003.

[110] a H. A. E. Almuhanna E A, "Optimization Of Dust Removal In Poultry Houses Using Electrostatic Wet Scrubber," *J. Appl. Sci. Res.*, vol. 8, no. 12, pp. 5651–5660, 2012.

[111] F. Di Natale, C. Carotenuto, L. D'Addio, A. Jaworek, A. Krupa, M. Szudyga, and A. Lancia, "Capture of fine and ultrafine particles in a wet electrostatic scrubber," *J. Environ. Chem. Eng.*, vol. 3, no. 1, pp. 349–356, 2015.

[112] H. G. Kim, H. J. Kim, M. H. Lee, and J. H. Kim, "Experimental study on the enhancement of particle removal efficiency in spray tower scrubber using electrospray," *Asian J. Atmos. Environ.*, vol. 8, no. 2, pp. 89–95, 2014.

[113] F. Di Natale, C. Carotenuto, L. D'Addio, and A. Lancia, "Effect of gas temperature on the capture of charged particles by oppositely charged water droplets," vol. 50, no. 2, pp. 110–117, Feb. 2016.

[114] U. Diebold, "The Surface Science of Titanium Dioxide," *Appl. Surf. Sci.*, vol. 48, no. x, pp. 53–229, 2003.

[115] S. A. Black, B. Pearls, and R. Spectra, "Carbon Black," *IARC monograph*, vol. 1995, no. April 1984. pp. 43–88, 1996.

[116] B. Weigand and D. Lauffer, "The extended Graetz problem with piecewise constant wall temperature for pipe and channel flows," *Int. J. Heat Mass Transf.*, vol. 47, no. 24, pp. 5303–5312, 2004.

[117] N. A. Fuchs, "Evaporation and droplet growth in gaseous media." London, 1959.

[118] O. B. Popovicheva, N. M. Persiantseva, V. Tishkova, N. K. Shonija, and N. A. Zubareva, "Quantification of water uptake by soot particles," *Environ. Res. Lett.*, vol. 3, no. 2, p. 25009, 2008.

[119] S. J. Gregg, S. Nashed, and M. T. Malik, "The adsorption of water vapour on a microporous carbon black," *Powder Technol.*, vol. 7, no. 1, pp. 15–19, 1973.

[120] G. H. Pollack, *The fourth phase of water : beyond solid, liquid, and vapor*. Ebner & Sons,

2013.

[121] F. Prodi, G. Santachiara, and C. Cornetti, “Measurements of diffusiophoretic velocities of aerosol particles in the transition region,” vol. 33, no. 1, pp. 181–188, 2002.

[122] F. La Motta, F. Di Natale, C. Carotenuto, and A. Lancia, “A heterogeneous condensation assisted three-phase bed column to remove submicronic particles,” *Chem. Eng. Trans.*, 2016.